GPU-Accelerated Optical Coherence Tomography Signal Processing and Visualization

Seyed Hamid Hosseiny Darbrazi
Department of Physics and Astronomy
University of Porto

This thesis is submitted for the degree of
Doctor of Philosophy

Porto 2016

Dedicated to my family

Preface

This thesis is the result of the work undertaken at the Center for Applied Photonics (CAP) Group of INESC TEC, situated at the Department of Physics and Astronomy of the Faculty of Science of the University of Porto, Porto, Portugal, and the Research Laboratory of Electronics (RLE) Laser Medicine and Medical Imaging Group, located at the Department of Electrical Engineering and Computer Science of the Massachusetts Institute of Technology (MIT), Cambridge, USA.

Except where specific reference is made to the work of others, the contents of this thesis are original and have not been submitted in whole or in part for consideration for any other degree or qualification in this, or any other University.

Hamid Hosseiny

Advisors:

Dr. Carla Carmelo Rosa, Assistant Professor, advisor at the University of Porto and the thesis advisor

Prof. James G. Fujimoto, Professor of Electrical Engineering and Computer Science, advisor at the Massachusetts Institute of Technology

Dr. Zhao Wang, Postdoctoral Associate, co-advisor at the Massachusetts Institute of Technology

Acknowledgements

This thesis would have not been possible without the support, time and dedication of many people with whom I had the pleasure of working throughout my PhD journey. Therefore, I would hereby like to express my sincere gratitude to all of them.

Foremost, I would like to thank my advisors Dr. Carla Carmelo Rosa, Prof. James Fujimoto, and Dr. Zhao Wang for sharing their knowledge, and for their guidance and support during my PhD study at their sites. It has been a true privilege to conduct my research at two international institutes of Portugal and USA, where I had access to outstanding resources and the opportunity to work in the world-class laboratories.

I am deeply grateful to all my caring colleagues and friends at the Center for Applied Photonics (CAP) Group and the Research Laboratory of Electronics (RLE) Laser Medicine and Medical Imaging Group. All scientific discussions during the weekly meetings, journal clubs and lab work are greatly appreciated. Not only did these scientific gatherings play an important role for the success of my work, but also the occasional social group gathering in Porto, Portugal and the seasonal social group meetings in Cambridge, USA.

I would like to acknowledge the financial support of the national Portuguese funding agency, Foundation for Science and Technology (FCT), through the grant SFRH/BD/72801/2010 for the entire PhD study. I would also acknowledge the external supplement support of the National Institute of Health and Air Force Office of Scientific Research during my study at the RLE Laser Medicine and Medical Imaging Group of the Massachusetts Institute of Technology (MIT).

Last, but not least, I am deeply thankful to my family to whom I dedicate this thesis. My most heartfelt thanks to my wife Parisa for her understanding, unending support, and unwavering love. Words cannot express how thankful I am to my father and mother for their all sacrifices, endless affection and unconditional love.

Abstract

Optical coherence tomography (OCT) has been continuously evolving over the past 25 years since its advent in early 1990's. Despite the advances in the development of ultrahigh-resolution and -speed OCT imaging systems, real-time processing and 2D/3D/4D visualization of acquired OCT volumes are required. The emergence of graphics processing unit (GPU) and its highly optimization advantage for massive parallel processing have tremendously assisted OCT technology to meet the aforementioned need. This thesis presents highly optimized GPU-based signal processing algorithms to significantly shorten processing time of spectral domain (SD) and swept source (SS) optical coherence tomography imaging systems. The optimization techniques for efficient OCT data processing and 2D/3D visualization are explained in detail. A real-time video rate volumetric 4D SS-OCT imaging system is developed. The potential applications of such a powerful optical imaging tool are introduced.

Thus far, high speed GPU-based OCT data processing approaches have been shown for processing and display of small OCT volumes because of GPU memory latency and some other hardware limitations. Conversely, this thesis demonstrates the feasibility of real-time processing and visualization of large OCT volumes (1024 A-scans$\times$1024 B-scans) with high efficiency (81%) by using only a single commercial-grade GPU.

The spectrometer design and optimization steps for SD-OCT imaging systems are described. Some important considerations to choose appropriate spectrometer components to improve the overall performance are explained. A spectral calibration method that can be used for calibration of SD-OCT and SS-OCT imaging systems is proposed, and it is numerically implemented. A real-time video rate SD-OCT imaging system is developed for sensing and imaging applications. Such a developed system is employed for quantitative evaluation of polyethylene terephthalate (PET) bottle preforms in realtime.

Keywords: Optical Coherence Tomography, OCT Signal Processing, Spectrometer Design and Optimization, Spectral Calibration, Optical Thickness Measurement, Intraoperative Optical Coherence Tomography, Graphics Processing Unit

Contents

List of Figures

List of Tables

Abbreviations

4D OCT	Four-Dimensional Optical Coherence Tomography
AWG	Arrayed Waveguide Grating
BOS	Broadband Optical Source
CAP	Center for Applied Photonics
CCD	Charged Coupled Device
CMOS	Complementary Metal Oxide Semiconductor
CP-SD-OCT	Common Path Spectral Domain Optical Coherence Tomography
CPU	Central Processing Unit
CUDA	Compute Unified Device Architecture
D2H	Device to Host
DC	Directional Coupler
DCPP	Dispersion-Compensating Prism Pair
DFT	Discrete Fourier Transform
DG	Diffraction Grating
DLL	Dynamic Link Library
DOCT	Doppler Optical Coherence Tomography
DSP	Digital Signal Processor

EVOH	Ethylene Vinyl Alcohol
FBG	Fiber Bragg Grating
FC/APC	Ferrule Connector/Angled Physical Contact
FC/PC	Ferrule Connector/Physical Contact
FD-OCT	Fourier Domain Optical Coherence Tomography
FFT	Fast Fourier Transform
FM	Fiber Mirror
FPGA	Field-Programmable Gate Array
FWHM	Full Width at Half Maximum
GLUT	OpenGL Utility Toolkit
GPU	Graphics Processing Unit
H2D	Host to Device
HBM	High Bandwidth Memory
LCCD	Line-Scan Charge Coupled Device Camera
MEMS	Micro-Electromechanical System
MIT	Massachusetts Institute of Technology
MTS	Motorized Translation Stage
NA	Numerical Aperture
NDF	Neutral Density Filter
NDFFT	Non-Uniform Discrete Fast Fourier Transform
NUFFT	Non-Uniform Fast Fourier Transform
OC	Optical Circulator
OCE	Optical Coherence Elastography
OCT	Optical Coherence Tomography

OPD	Optical Path Difference
PC	Polarization Controller
PET	Polyethylene Terephthalate
PS-OCT	Polarization Sensitive Optical Coherence Tomography
RC	Reflective Collimator
RLE	Research Laboratory of Electronics
RM	Reference Mirror
SD-OCT	Spectral Domain Optical Coherence Tomography
SH	Sensing Head
SM	Scanning Mirror
SMF	Single Mode Fiber
SNR	Signal to Noise Ratio
SOCT	Spectroscopic Optical Coherence Tomography
SS-OCT	Swept Source Optical Coherence Tomography
TD-OCT	Time Domain Optical Coherence Tomography
UP	University of Porto
VCSEL	Vertical-Cavity Surface Emitting Laser

Chapter 1

Introduction

Several biomedical imaging modalities have been introduced to improve the quality of medical care and treatment procedure [1–3]. Each imaging modality offers specific resolution and penetration depth that makes them a suitable choice for imaging of certain human organs, providing accurate and in some cases early diagnosis. Optical coherence tomography (OCT) emerged among these advanced imaging techniques in early 1990s [4]. The technique is analogous to ultrasound imaging in terms of scanning regimes with the difference that OCT employs light instead of sound waves to visualize the testing sample. It has higher resolution than ultrasound, and on the other hand greater penetration depth than confocal microscopy. OCT therefore fills an important niche between ultrasound and confocal microscopy imaging methods [5].

OCT is based on white light (or low coherence) interferometry, where an optical source with a short coherence length, or, in other words, a broad spectral bandwidth, is employed. White light interferometry technique typically generates one-dimensional (1D) interference signal at the output of the interferometer. OCT is a two-dimensional (2D) or three-dimensional (3D) version of white light interferometry. It was created by adding a transversal scanner at the sample arm of the interferometer to create 2D cross-sectional images [4].

As a white light interferometry technique, the interference OCT signal is detectable only if the optical path difference (OPD) between sample and reference optical paths is less than the coherence length of the broadband optical source. The axial resolution of such an interferometric technique is determined by the spectral properties of the light source. The resolution is inversely proportional to the optical bandwidth of the light source: the broader the optical bandwidth, the finer the resolution becomes. Nowadays OCT is capable of delivering ultrahigh-resolution cross-sectional images due to progressive advances in the development of optical sources [6]. The penetration depth of this imaging technique is dependent on the scattering and absorption properties of the sample under test. In most

biological tissues, the penetration depth is typically between 2-3 mm at 1300 nm wavelength region [7].

1.1 Significance and Applications

OCT embraces distinguished advantages and capabilities, making it a suitable imaging modality for a wide range of biomedical and industrial imaging applications:

1. It offers a high axial resolution in the range of 1-15 μm, enabling precise measurement and imaging of the interrogated samples [8, 9].

2. In contrast to confocal microscopy, OCT's axial resolution is decoupled from its lateral resolution. The axial resolution is determined by the coherence length of the light source, whereas transverse resolution is determined by the focusing optics properties. This important advantage contributed to the development of ultra-high resolution OCT systems [10–12].

3. In comparison with microscopy imaging, OCT permits the sample to be placed in longer working distances from the objective lens while maintaining an excellent axial resolution.

4. OCT is a non-invasive and contact-free imaging modality.

   Features (3) and (4) empower OCT to perform bioimaging in situ, eliminating the need for excisional biopsy.

5. This imaging technique provides high dynamic range and sensitivity, allowing in vivo imaging of highly scattering samples such as biological tissues [13].

6. OCT is categorized as a safe imaging technique as it employs light within visual and near infrared spectral regions.

7. OCT is considered as a cost-effective imaging method compared to other equivalent imaging modalities, such as fluorescein angiography, to screen and diagnose various retinal diseases [14].

8. Multi-megahertz scanning speed is another distinct advantage of some extensions of OCT imaging technique [15]. Nowadays, multi-megahertz OCT systems are capable of delivering OCT volumes with axial scan rate of 40 MHz [16]. This high speed advantage eliminates motion artifacts in the resultant images and also enables 3D visualization of the captured OCT volume data in real time [17, 18].

9. Apart from structural imaging, OCT can also be utilized for functional imaging. Different extensions of OCT such as spectroscopic OCT (SOCT), polarization sensitive OCT (PS-OCT), Doppler OCT (DOCT), optical coherence elastography (OCE), and molecular imaging OCT have demonstrated the power of this technique to extract functional information from biological tissues [19].

10. The miniaturization of some components of OCT system and the small diameter of single mode optical fibers (~125 μm) enable the use of OCT in catheters and endoscopes [20, 21]. Today OCT is able to interrogate internal human organs with much higher resolution than other imaging modalities such as ultrasound [22, 23].

Above advantages have distinguished OCT as an extremely powerful imaging modality for medical and non-medical imaging applications. The large volume of OCT journal publications in the fields of ophthalmology and optometry indicates the importance and indispensable role of OCT in these areas, where OCT is now a clinical standard. The quantitative information that OCT collects from the eye cannot be obtained by using other high resolution imaging modalities. These days OCT is widely used in imaging of retina and anterior segment, diagnosis of variety of retinal diseases, and monitoring disease progression [24–27]. After ophthalmology field, another major area that OCT has been successfully deployed is in cardiology, where OCT has contributed to the understanding of variety of cardiovascular diseases [7, 28].

OCT has been interfaced with catheters and endoscopes, allowing internal imaging of gastrointestinal, pulmonary, and urinary tracts with the high resolution of more than 12 times better than ultrasound [29–31]. OCT has also shown a great potential in monitoring cancer treatment [32, 33]. Dentistry is another field that OCT was effectively employed in assessing the extent of dental caries on smooth enamel surfaces of human teeth [34]. Non-invasive, high resolution and high speed features of OCT have enabled the use of this technology in the field of dermatology, where OCT has been utilized for morphological evaluation of skin, and investigation of skin tumors and inflammatory skin diseases [35, 36]. Functional extensions of OCT can reveal structural and functional information of the investigated tissue in a single measurement. This aspect of OCT has been used in multiple functional imaging applications such as identification of vasculature, blood flow, and architectural and cellular organization of retinal nerve fibers [19, 37, 38].

OCT technology has also been successful outside the medical field. Dimension metrology, non-destructive evaluation and material characterization, data storage and security, botany and microfluidics are some non-medical applications of OCT, reviewed in Ref. [39]. In art conservation, OCT outperforms other imaging techniques and obtained subsurface

information for thickness assessment of the varnish and paint layers of old master painting [40]. In pharmaceutical industry, OCT was exploited as an in-line quality control tool to monitor and measure the coating thickness of various tablets [41].

1.2 Thesis Objectives

All studies are conducted based on two OCT imaging methods, spectral domain OCT (SD-OCT) and swept source OCT (SS-OCT), to fulfill the proposed initial objectives. The primary objectives of this thesis are as follows:

- To conduct comprehensive study on different factors affecting the performance and image quality of SD-OCT imaging system.
- To improve the overall performance of the existing SD-OCT imaging system that is based for all future experiments for sensing and industrial imaging applications.
- To design and implement a spectrometer for the existing SD-OCT imaging system.
- To implement hardware interfaces to accomplish ultrahigh-speed OCT data acquisition, processing and visualization schemes.
- To study on optimization of volumetric OCT data processing and visualization techniques in order to achieve real-time video rate SD- and SS-OCT imaging systems.
- To develop optimized graphics processing unit (GPU)-based signal processing algorithms to significantly improve signal processing speed of SD- and SS-OCT imaging systems.
- To construct a highly parallelized and optimized two- and three-dimensional visualization methods for real-time structural and functional imaging.
- To develop a live video rate volumetric four-dimensional (4D) OCT (3D+time) system that is used as an optical guidance tool to provide intraoperative feedback for microsurgical applications.

The presented work was developed at the University of Porto (UP) and Massachusetts Institute of Technology (MIT). All experiments and studies based on SD-OCT were performed at the Center for Applied Photonics (CAP) Group of INESC TEC situated at the Department of Physics and Astronomy of the Faculty of Science of the University of Porto, Porto, Portugal [42]. The main focus of the CAP Group is on white light interferometry techniques and

development of optical fiber sources, fiber communications, fiber sensors and fiber microfabrication. At CAP, OCT is mainly used for sensing, optical measurement and real-time monitoring applications in industry because of the good relation of INESC TEC with its industrial collaborators.

All studies based on SS-OCT were conducted at RLE Laser Medicine and Medical Imaging Group located at the Department of Electrical Engineering and Computer Science of the Massachusetts Institute of Technology, Cambridge, USA [43]. RLE Laser Medicine and Medical Imaging Group is the inventor and world leader of many inventions in the field of OCT. Their active research areas include high-speed and high-resolution imaging, functional Doppler flow and angiography, and polarization sensitive methods. The group employs OCT in several biomedical imaging applications such as multiphoton microscopy imaging, ophthalmic imaging, endoscopic imaging, and small animal imaging.

1.3 Thesis Organization

The thesis is divided into the following chapters to meet the proposed objectives of the PhD study:

Chapter 2 details theoretical basis of OCT. Each OCT imaging method and their principles of operation are explained. The advantages and disadvantages of each imaging technique are discussed. Different scanning regimes of OCT are next presented. System resolution and the factors affecting axial and transverse resolutions of OCT systems are introduced. The concept of system sensitivity is described. Sensitivity fall-off and the parameters causing the sensitivity decay with respect to the depth are discussed. Dispersion theory is ultimately elucidated.

Chapter 3 specifies the design steps and some considerations that should be taken into account for a spectrometer design of a SD-OCT system. The implementation steps are given. Two spectrometer configurations are designed and explained in detail.

Chapter 4 introduces a numerical study on a calibration method performed by phase calibration. It highlights the importance of calibration and re-sampling methods. The signal to noise ratio is assessed based on two approaches. The pros and cons of each approach are discussed.

Chapter 5 presents the performance characterization of the developed common path SD-OCT system. The performance of the system is expressed based on typical characterization parameters such as fringe visibility, sensitivity, sensitivity fall-off, system resolution, maximum imaging depth and processing speed. Three different non-biological samples are examined and the results are demonstrated.

Chapter 6 describes the optimization techniques to significantly shorten signal processing and visualization time. All technological challenges to achieve a real-time video rate volumetric 4D SS-OCT system are detailed. Real-time processing and visualization of large OCT volumes with high efficiency and axial scan rate is demonstrated. The future applications of such developed 4D OCT system are given.

Chapter 7 offers an approach based on spectrally resolved white light interferometry technique for quantitative assessment of polyethylene terephthalate (PET) bottle preforms. The development of a real-time video rate SD-OCT imaging system is described. An optimized GPU-based signal processing algorithm to develop a real-time inline optical inspection tool for monitoring and quality control of the produced PET preforms at industrial production lines is explained. The temporal performance of such a highly optimized algorithm is detailed. A post-processing approach is proposed to automate computation of optical thickness measurement of PET preform layers.

Chapter 8 concludes the thesis and provides a perspective for future studies.

1.4 Thesis Contributions

Data processing and visualization of captured OCT data volumes in realtime are compute-intensive. It requires a high performance imaging system and fast data processing and visualization algorithms. This thesis has contributed to the development of realtime video rate volumetric 4D OCT imaging systems. The thesis has provided highly optimized GPU-based OCT signal processing and visualization algorithms to significantly shorten the processing and visualization time of SD- and SS-OCT imaging systems, eliminating one of main bottlenecks of OCT imaging systems.

A spectral calibration method was implemented to calibrate and re-sample the captured spectral data in evenly spaced in $k-space$. Such a spectral method works on SD- and SS-OCT imaging systems, playing an important role in achieving high signal resolution. The $k-space$ linearization and re-sampling methods were further developed under GPU architecture.

A spectrometer with two configurations was implemented aiming to increase the overall performance of the existing SD-OCT imaging system at CAP's lab of INESC TEC. The performance parameters of the imaging system were significantly improved, making the system ready to perform imaging in realtime. The system sensitivity was increased to $\sim$ 98 dB, the maximum imaging range was improved by more than threefold, and the axial resolution was enhanced by almost twofold.

A live video rate volumetric intraoperative 4D SS-OCT application was developed to be

deployed to a microsurgery system at New England Eye Center. The developed processing and visualization algorithms only employ a low-cost consumer grade GPU to process and display large OCT volumes in realtime. The reliance on a single GPU also eases the adaptation of the 4D OCT application with each microsurgery system in the clinic. The proposed approach in this thesis for the acquisition and real-time processing of large OCT volumes empowers physicians to scan a large area resulting in better understanding of anatomy and consequently enhancing surgical decision-making during surgeries.

A realtime video rate SD-OCT imaging system was developed at CAP's lab for sensing and imaging applications. Such a highly optimized fast imaging system was proposed as an inline inspection tool to quantitatively assess polyethylene terephthalate (PET) bottle preforms in realtime at industrial production lines. The thesis has offered a post-processing procedure to automate the thickness measurement of laminated PET bottle preforms and better visualize the thickness of layers for operators working at production lines.

Chapter 2

Principles of Optical Coherence Tomography

The main focus of this chapter is to give a solid background on the theory and physics behind OCT. Operation principles of OCT imaging methods, together with the pros and cons of each method, are reviewed. The concept of some system specifications, such as system resolution, imaging depth, sensitivity fall-off affecting the overall system performance, is described. The dispersion theory is explained in detail.

2.1 Principles of Operation

OCT imaging techniques are divided into two variant methods: time domain OCT (TD-OCT) and Fourier domain OCT (FD-OCT) [44]. A typical OCT imaging system consists of an optical source, an interferometer, a scanning unit and a processing unit. As shown in Fig.2.1 the interferometer is fed by an optical source. Different interferometer configurations can be employed to implement an OCT imaging system. A Michelson interferometer set-up, as illustrated in Fig.2.1, is commonly used. First, the light from the optical source is divided by a beam splitter or a directional coupler into two arms known as the reference and the sample arms. The beam travels a round trip in both arms. In the sample arm there is a scanning unit, transversally scanning the testing sample by using a Galvo scanning mirror or a micro-electromechanical system (MEMS) scanning mirror. The back scattered and the back reflected lights interfere with one another at the beam splitter or the directional coupler, creating fringes corresponding to the optical path length mismatch between the sample and the reference arm beams. Ultimately the interference signal is detected and processed by the processing unit, as indicated in Fig.2.1.

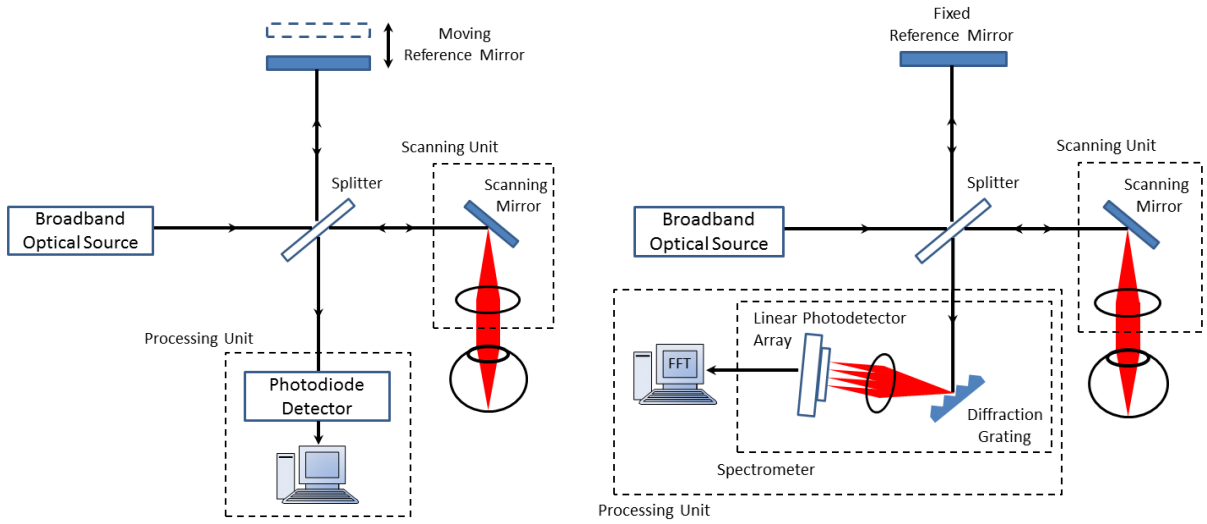

(a) TD-OCT (b) SD-OCT

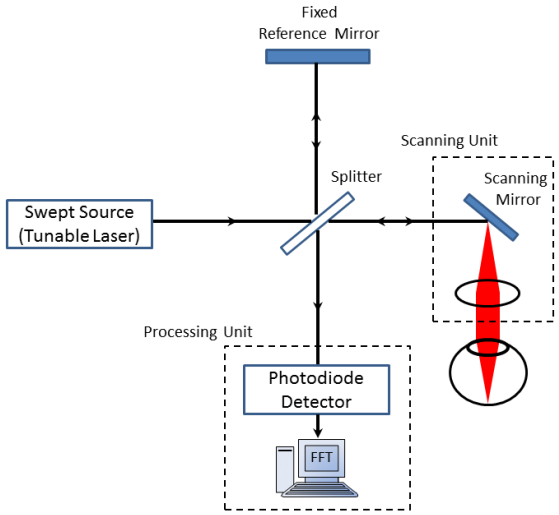

(c) SS-OCT

Figure 2.1: Schematic diagram of various OCT imaging systems.

2.1.1 Time Domain Optical Coherence Tomography

The first generation of OCT system was TD-OCT. In this approach, a broadband optical source with an extremely short coherence time is used. The reference mirror is translated longitudinally, as shown in Fig.2.1.a, to axially scan the testing object. In this imaging method, the processing unit comprises of a photodiode detector registering the time-varying interference signal. After detection and acquisition of the interference signal, the photo-detected signal is amplified, filtered by a low pass filter and then rectified, in order to keep

only the envelope of the resulting signal [45, 46]. This method is called TD-OCT as the structural information of the object is obtained by translating the reference mirror with a time-varying location.

Like other imaging methods, TD-OCT has some advantages and disadvantages. The primary advantage of such imaging method is that it allows adjusting the focal spot point by point, in depth, as the reference mirror is translated [11]. This dynamic focus feature is unique to TD-OCT since other OCT imaging techniques cannot provide such a capability. In addition, this feature enables a selective and large depth of focus in a complete range of an axial scan, hence making optical sectioning of the sample possible. Another additional advantage of this method is its lower overall cost compared to other OCT techniques, because of its hardware simplicity.

TD-OCT has also some constraints. As the A-scans are obtained by moving the reference mirror, this results in slow acquisition rate (in the order of kHz) [47, 48]. Such a slow acquisition speed yields imaging at a few frames per second, thus making it suitable for small axial field of view imaging [49]. In addition, it is hardly feasible to perform in vivo 3D imaging in real-time because of the aforementioned acquisition speed limitation [49].

2.1.2 Fourier Domain Optical Coherence Tomography

FD-OCT is the next generation after the advent of TD-OCT [50]. In this approach, the structural information is encoded in the frequency of the detected oscillatory interference signal. FD-OCT embraces two configurations to detect such a signal: spectral domain OCT (SD-OCT) and swept source OCT (SS-OCT).

In SD-OCT, a broadband light source is employed as an optical source. The processing unit has a spectrometer consisting of a prism or a diffraction grating and a linear photodetector array at the output of the interferometer. At the detection arm the interference signal is first dispersed in wavelength by using a dispersive optical element, e.g. either the diffraction grating or the prism. The dispersed light is then detected by a linear photodetector array which is usually either a charged coupled device (CCD) or a complementary metal oxide semiconductor (CMOS) linear camera. A schematic diagram of a typical SD-OCT system configuration is presented in Fig.2.1.b.

In SS-OCT, a swept source tunable laser is used as an optical source. The processing unit employs a photodiode detector. In this approach the axial scanning is performed by sweeping the individual wavelengths of the optical source. Each sweep of wavelengths generates an interference signal by the reflections at different depths. A schematic diagram of a typical SS-OCT imaging system configuration is presented in Fig.2.1.c.

In FD-OCT imaging methods, there is no need to translate the reference mirror to obtain

the depth information of the testing sample. The depth information is attained by performing an inverse Fourier transform. In this imaging approach, the detected spectral fringes must be evenly sampled in wavenumber space (*k-space*) before applying the inverse Fourier transform. However, as the detected signal is more often measured as a function of wavelength (λ) instead of wavenumber (k), and there is a non-linear relation between λ and k ($k = 2\pi/\lambda$), the spectral fringes normally are not evenly sampled in *k-space*. Therefore, in this imaging method calibration and resampling methods are often used to place the sampled data equally spaced in k-space prior to the inverse Fourier transform stage. The calibration and resampling methods are explained in detail in Chapter 4 of this thesis.

In SD-OCT, the captured spectral fringes at the detector are expressed as a function of wavenumber as [51, 52]:

$$I(k) = s(k)\{a_r + \sum_{s_i} a_{s_i} + 2\sum_{s_i}\sum_{s_i \neq s_j} \sqrt{a_{s_i} a_{s_j}} \cos(2k(z_{s_i} - z_{s_j})) + 2\sum_{s_i} \sqrt{a_r a_{s_i}} \cos(2k(z_r - z_{s_i}))\} \quad (2.1)$$

where *s(k)* is the spectral intensity distribution of the light source as a function of wavenumber, a_r is the reflectivity of light in the reference arm, $a_{s_i}$and $a_{s_j}$are the reflectivity of light at the $i^{th}$and j^{th}layer of the sample, and z_r, $z_{s_i}$and $z_{s_j}$are the optical path length of the reference arm, $i^{th}$and j^{th}layers of the sample, respectively. Now by applying an inverse Fourier transform to Eq.2.1, the depth information, $i(z)$, is retrieved as [51, 52]:

$$i(z) = \left|FFT^{-1}_{k\to z} < I(k) >\right| = \Gamma(z) * \{a_r \delta(z) + \sum_{s_i} a_{s_i} \delta(z) + 2\sum_{s_i}\sum_{s_i \neq s_j} \sqrt{a_{s_i} a_{s_j}} \delta(z \pm z_{s_i s_j}) + 2\sum_{s_i} \sqrt{a_r a_{s_i}} \delta(z \pm z_{r s_i})\} \quad (2.2)$$

where $\Gamma(z)$ is the coherence function (the Fourier transform of the source spectrum), z is the optical path difference between sample and reference arms, $z_{s_i s_j} = z_{s_i} - z_{s_j}$ and $z_{r s_i} = z_r - z_{s_i}$. The total signal consists of DC, auto-correlation and cross-correlation terms. The first two terms of Eq.2.1 and 2.2 are known as DC terms and they appear close to OPD zero in the reflectivity profile. The DC terms are undesired, and these non-interferometric terms are eliminated by background subtraction methods at the processing stage. The third term is known as auto-correlation term describing the mutual interference between the layers within the testing sample. This term has a very small contribution to the total signal and can be

neglected. The last term is known as cross-correlation term containing depth information of the examined sample.

In SS-OCT, the detected spectral interferogram as a function of wavenumber, $I_D(k(t))$, is expressed as [53]:

$$I_D(k(t)) = \frac{\eta q}{h\nu}\left\{P_r + P_s\int a^2(z)dz + 2\sqrt{P_r P_s}\int a(z)\Gamma(z)\cos(2k(t)z+\phi(z))dz\right\} \tag{2.3}$$

where η is the detector sensitivity, q is the quantum of electric charge (1.6×10^{-19} coulomb), $h\nu$ is the single photon energy, P_r is the optical power coming from reference arm, P_s is the optical power at the sample arm, z is the OPD, and $\Gamma(z)$ is the coherence function of the laser source. Here, $a(z)$ and $\phi(z)$ are respectively the amplitude and phase of the backscattered profile of the sample expressed as a function of OPD. $k(t)$ is the wave number, changing over the time by tuning the laser. In Eq.2.3, the first and the second terms are non-interferometric terms and are known as DC and autocorrelation terms, respectively. The interferometric signal containing the structural information of the sample is the third term known as cross-correlation term.

In FD-OCT imaging method, in contrast to TD-OCT, the reference mirror is kept fixed, and the depth information is retrieved by performing an inverse Fourier transform. The Elimination of the mechanical scanning of the reference mirror enables a dramatic increase in imaging speed and sensitivity [13, 47, 54, 55]. Such increase allows imaging of a large field of view with less motion artifacts compared to TD-OCT images. Nowadays, the FD-OCT imaging systems are favorable for versatile applications because of its distinguished imaging speed and sensitivity advantages over conventional TD-OCT systems.

Although FD-OCT emerged as the best promising low-coherence imaging technique, it presents some disadvantages and limitations that need to be addressed:

1. Unlike TD-OCT, dynamic focusing is not possible [11]. One solution to equip FD-OCT systems with such capability is to design the interface optics to have a large depth of focus. However, this method does not allow using a high numerical aperture objective, which consequently degrades the transverse resolution [46].

2. As the detected spectrum is a real function, the Fourier transformation of the channeled spectrum has symmetric spectral terms [11, 56]. If no additional processing is performed, the reflectivity profile resulting from the Fourier transformation has mirrored images around OPD zero, meaning a repetition of the information in both positive and negative optical path difference. This is even more severe if OPD zero is placed

in the middle depth of the region of interest as the information of both positive and negative OPDs would be overlapped, preventing a reliable analysis of the observed structure. In order to avoid such overlap, the OPD zero is placed at the outer layer of the testing sample. As a solution, some methods such as phase-shifting and Talbot bands based methods have been devised to double the scan range and reduce the effect of the mirror terms [57, 58].

3. In FD-OCT the sensitivity is not the same for any OPD values. The system sensitivity is the highest around the OPD zero, and it gradually decays by the increase of OPD. This is one of the main disadvantages of FD-OCT and is known as sensitivity fall-off along the depth [59]. Such an effect is caused by the finite resolution of FD-OCT systems in separating peaks and troughs of the detected spectral fringes. A high number of grating lines and pixel cameras in the case of SD-OCT, and a very narrow line width in the case of SS-OCT are desirable to lessen this effect [11]. The sensitivity fall-off phenomenon and its effect are explained in more detail in Section 2.4 of this chapter.

4. FD-OCT data processing methods require intense computations and large memory spaces, since huge volume of numerical interpolation and FFT are involved. Real time volumetric OCT imaging in vivo is therefore hardly possible to be handled by central processing units (CPUs). Hence the acquired data is processed in post-processing mode, incurring a significant time overhead. As some remedies for this issue, Field-Programmable Gate Array (FPGA) [60], multi-core CPU parallel processing [61], digital signal processor (DSP) [62] and graphics processing units (GPU) [63, 64] have been proposed to significantly reduce FD-OCT data processing and visualization time.

2.2 OCT Scanning Procedures

In general there are two types of possible scanning procedures: depth and lateral scanning [65]. In TD-OCT the depth scan performs by translating the reference mirror to change the delay of the reference beam. In FD-OCT there is no need for depth scanning as the depth information is encoded in the sinusoidal modulation of the acquired spectral fringes. Lateral scanning is obtained either by moving the sample or translating the beam across the sample using scanning mirror(s). Usually OCT lateral scanning is carried out by one or two orthogonal scanners placed at the sample arm to transversally scan the examined sample in x and y directions.

The extraction of depth information at a single transverse location of the examined

sample is known as axial scan, or A-scan. In TD-OCT, the depth scanning is first performed by the reference mirror and then, the depth dependant captured interference signal is amplified, filtered and rectified to form an A-scan. In SD-OCT, the spectral fringes are read and inverse Fourier transformed to form an A-scan. In SS-OCT, the depth scan is performed by sweeping the individual wavelengths of the laser source and then the 1-sweep information is inverse Fourier transformed to form an A-scan.

By lateral scanning the probed beam across the sample, a cross-sectional image, known as B-scan, is built. In other words, a B-scan image consists of adjacent successive A-scans. The combination of consecutive B-scans forms a volume, or 3D OCT dataset.

2.3 System Resolution

The resolution of OCT systems is expressed in terms of axial (depth) resolution and lateral (transverse) resolution. In contrast to conventional microscopy, the axial resolution of an OCT system is independent of its lateral resolution.

2.3.1 Axial Resolution

The axial or depth resolution is specified by the coherence length of the used optical source. For a Gaussian spectrum the coherence length (l_c) is defined as follows [59]:

$$l_c = \frac{4\ln(2)}{\pi}\frac{\lambda_0^2}{\Delta\lambda} \tag{2.4}$$

where λ_0 is the central wavelength and $\Delta\lambda$ is the full width at half maximum of the light source spectrum. As the light travels twice the distance in an OCT system, the minimum resolvable distance, or in other words, the axial resolution (Δz), corresponds to half the coherence length, and is given by [59]:

$$\Delta z = \frac{l_c}{2n} = \frac{2\ln(2)}{n\pi}\frac{\lambda_0^2}{\Delta\lambda} \tag{2.5}$$

where n is the refractive index of the interrogated sample. Eq.2.5 demonstrates that the axial resolution is inversely proportional to the spectral bandwidth of the optical source and also directly depends on the square of the central wavelength. The broader the bandwidth of the source, the shorter the coherence length and consequently the better the axial resolution is.

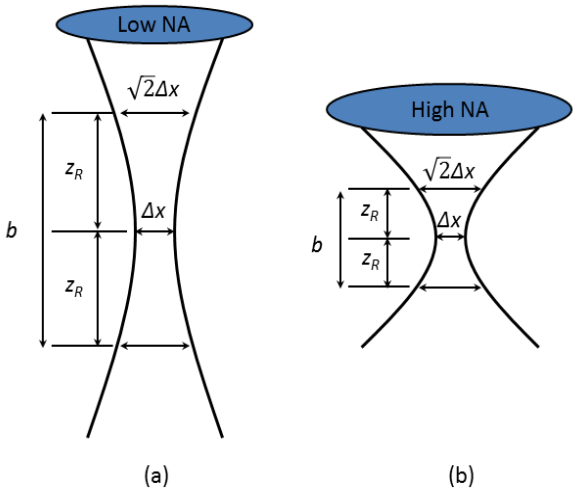

Figure 2.2: A comparison of depth of focus and lateral resolution between low and high numerical aperture (NA) objective lenses: (a) a low NA objective lens has high depth of focus and lower lateral resolution, whereas (b) a high NA objective lens has higher lateral resolution and lower depth of focus.

In overall, an optical source with a wide spectral width and perfect Gaussian spectral shape is highly desirable. The non-Gaussian spectral shape of the optical source introduces side-lobes, lowering the axial resolution. Apart from the source spectral shape, some other effects such as uncompensated dispersion and unmatched polarization between sample and reference arms also degrade the axial resolution of OCT systems [66].

2.3.2 Lateral Resolution

Similar to conventional microscopy, the lateral or transverse resolution of both TD- and FD-OCT systems is determined by focusing optics design of sample arm. The lateral resolution is the diffraction limited spot size on the sample and is defined as [67, 68]:

$$\Delta x = \frac{4\lambda_0}{\pi}\frac{f_{obj}}{d} \tag{2.6}$$

where Δx is the lateral resolution, λ_0 is the central wavelength of the optical source, f_{obj} is the focal length of the objective lens, and d is the size of the beam waist at the objective lens. Eq.2.6 clearly demonstrates that a larger numerical aperture focusing the beam to a smaller spot size increases the lateral resolution. As shown in Fig.2.2, the use of high numerical aperture would decrease the depth of focus or the confocal parameter known as b which is

twice the Raleigh range, z_R [67, 68]:

$$b = 2z_R = \frac{\pi \Delta x^2}{2\lambda_0} \tag{2.7}$$

On the other hand, lower numerical aperture increases depth of focus at the cost of losing the lateral resolution. Therefore, in an OCT system there is always a trade-off between lateral resolution and depth of focus between which a compromise has to be found.

2.4 Sensitivity Fall-off

If the sensitivity is defined as the signal to noise ratio for a perfect sample reflector, in the case of TD-OCT, the sensitivity is the same for any axial position along an A-scan [11]. This is due to the fact that as the reference mirror scans, two signals coming from reference and sample arms are completely overlapped at each position of the coherence gate. Therefore, while the reference mirror is translating, the maximum sensitivity is moved from one layer of the sample to another, resulting in constant sensitivity with increasing OPD. However, this depth independent sensitivity does not hold true for FD-OCT systems.

By assuming a single reflector as a sample, and excluding the DC terms from Eq.2.1, the detected interference signal can be shortly expressed as a function of wavenumber (k) as:

$$I(k) = s(k)\cos(k\Delta z) \tag{2.8}$$

where $s(k)$ is the spectral intensity distribution of the optical source and Δz is the optical path difference between reference mirror and the single reflector. From theory perspective, the amplitude of the oscillatory cosine in Eq.2.8 after performing an inverse Fourier transform should be independent of the cosine frequencies and should remain the same for all frequencies, or, in other words, for all OPDs. However, experimental results have demonstrated that the amplitude of the cosine or the fringe visibility decays as OPD increases. This phenomenon is known as sensitivity fall-off, limiting useful imaging range of FD-OCT imaging systems.

This depth dependent sensitivity fall-off effect is depicted in Fig.2.3. A reflecting mirror is placed as a sample at different depths as shown in Fig.2.3. The reflecting mirror returns equal optical power at different depths; hence, the same fringe visibility should be obtained for all positions of the mirror. Conversely, as illustrated in Fig.2.3, the reflectivity profile exhibits less sensitivity for the reflecting mirror positioned at deeper depths.

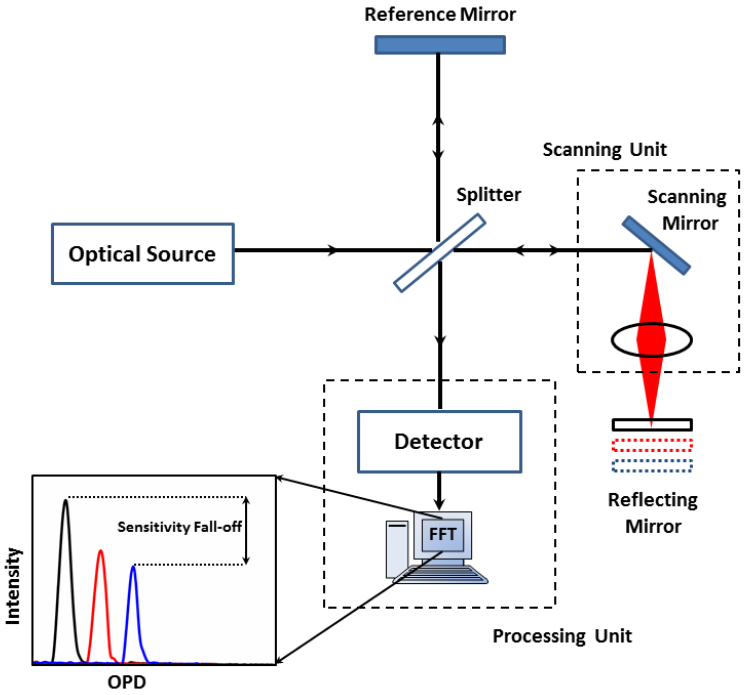

Figure 2.3: An illustration of depth dependent sensitivity fall-off effect.

In both FD-OCT imaging methods, the reference and sample signals are entirely overlapped only near OPD zero, and the amount of overlap for other axial positions gradually diminishes with increasing OPD [11]. This explains why the sensitivity drops at longer depths.

In SD-OCT, the design and implementation of the spectrometer is of paramount importance to minimize the sensitivity fall-off effect. An optimized design uses a diffraction grating with a large number of closely spaced grooves, providing sufficient resolution in separating peaks and troughs of the captured spectral fringes. In SS-OCT, a swept laser source with a line width as narrow as possible is highly desirable to increase the resolution and therefore mitigate such an effect.

In a spectrometer, the collimated beam first hits a diffraction grating. It is therefore essential to design a spectrometer in which the collimated beam size matches the aperture window of the diffraction grating. Otherwise, such unmatched beam diameter degrades spectrometer efficiency and sensitivity.

The pixels of the line-scan camera have a rectangular shape resulting in a *rect* function as impulse response. The sensitivity fall-off effect in SD-OCT can therefore be described as a convolution of the detected spectral fringes with the *rect* function in the frequency domain [47]. According to the convolution theorem, the resulting signal is the multiplication of a

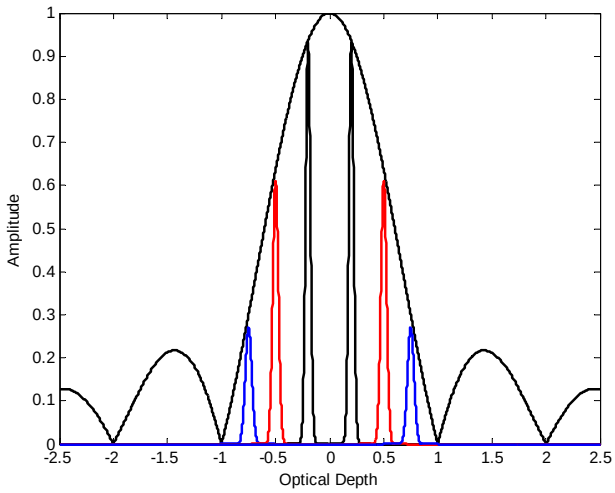

Figure 2.4: Simulation of the fall-off in the amplitude of the resulting signal for various optical depths.

sinc function by the Fourier transformed of the collected spectral fringes. Fig.2.4 simulates the amplitude fall-off of the signal (the black envelope), and the signal corresponding to a mirror reflection at three optical depths, after applying the Fourier transform. The MATLAB code for such a simulation of sensitivity fall-off effect can be found in Appendix D.1.

The frequency of the spectral fringes increases at longer depths. In the case of SD-OCT, the spectrometer detects the full spectral bandwidth of the optical source by using a finite number of camera pixels, limiting the spectral sampling of the detected spectral fringes. When the sampling frequency of the spectrometer is far less than at least twice the frequency of the spectral fringes, the fringes are washed out and the detector is not able to detect high frequencies originating from deep depths. Therefore, using a line scanned camera with a large number of pixels (greater than 2048 pixels) increases the sampling points, thus reducing sensitivity fall-off and increasing imaging range.

The other factors affecting the sensitivity fall-off are the focusing spot size of the beam on the camera and the pixel size. The size of the focused Gaussian beam width should be smaller than the pixel size [69]. Otherwise, some intensity smear into the neighboring pixels and some are lost in vertical direction, hence increasing the sensitivity fall-off. In addition, aberration in the focusing optics introduces distortion and increased spot size [59]. Therefore, a good design for spectrometer optics is vital to minimize the sensitivity fall-off effect. The design steps and some important considerations for an optimized spectrometer are detailed in Chapter 3 of this thesis.

2.5 Dispersion

The dispersion is defined as the wavelength dependency of the propagation velocity of light through a physical medium. The refractive indices of shorter wavelengths of light are higher in the dispersive medium; hence, these wavelength components of light propagate through the medium at lower speeds than higher wavelengths. Therefore, their travelling time or path length must be compensated; otherwise, such a phenomenon broadens the interferogram, degrading the axial resolution [70].

In addition to degradation of resolution, this phenomenon decreases signal to noise ratio and system sensitivity [59]. The dispersion imbalance between two arms also introduces image artifacts, corrupting the resultant images [71, 72]. As different wavelengths of light have various speeds in the dispersive medium, their path lengths are matched at different reference mirror positions. This makes the oscillation period of the interference fringes non-periodic, creating a beat effect and a multiple signal peak splitting within the coherence envelope [72]. Such consequences yield in presence of artificial layers in the obtained images when several closely spaced layers such as retina layers are imaged.

The dispersion phenomenon is caused by various factors in an OCT imaging system. Employing non-identical optical components and materials such as different fibers and lenses at sample and reference arms of the interferometer creates dispersion imbalance between two arms. Furthermore, imaging a dispersive material would also bring about dispersion, even if identical optical components are used in an interferometer.

2.5.1 Dispersion Theory

This section is a review on dispersion theory written in Ref.[71]. According to the Wiener–Khintchine theorem, the autocorrelation (coherence) function, $\Gamma(\tau)$, and the spectral density, $G(\omega)$, of the optical source are related by a Fourier frequency transform [73]:

$$\Gamma(\tau) = FFT\{G(\omega)\} = \int_{-\infty}^{+\infty} G(\omega)\, e^{-i\omega\tau} d\omega \tag{2.9}$$

A time delay τ_0 introduces a phase, $\phi_0 = \omega\tau_0$, in the coherence function that can be expressed as:

$$\Gamma(\tau+\tau_0) = \int_{-\infty}^{+\infty} G(\omega)\, e^{-i\phi_0} e^{-i\omega\tau} d\omega \tag{2.10}$$

The travel of light through the dispersive medium aggregates a dispersive phase, ϕ_{Disp}:

$$\Gamma_{Disp}(\tau+\tau_0) = \int_{-\infty}^{+\infty} G(\omega)\, e^{-i(\phi_0+\phi_{Disp})} e^{-i\omega\tau} d\omega \tag{2.11}$$

Such dispersive phase can be expanded by a Taylor series near the central frequency of the source ω_0 as:

$$\begin{aligned} \phi_{Disp}(\omega-\omega_0) &= k(\omega-\omega_0)z \\ &= k(\omega_0)z + k^{(1)}(\omega_0)(\omega-\omega_0)z + \frac{1}{2}k^{(2)}(\omega_0)(\omega-\omega_0)^2 z + \\ &\quad \frac{1}{6}k^{(3)}(\omega_0)(\omega-\omega_0)^3 z + ... \end{aligned} \tag{2.12}$$

where $k^{(j)}(\omega_0) = \left(\frac{d^j k}{d\omega^j}\right)_{\omega=\omega_0}$ is the j^{th} order dispersion and z is the path length in the dispersive medium. The zero order dispersion $k(\omega_0)$ adds a constant phase. The first order dispersion $k^{(1)}(\omega_0)$ describes the inverse group velocity and adds a phase term linear in ω to the spectrum. The first order changes the coherence length to:

$$l_{c,Disp} = \frac{l_c}{n_g} \tag{2.13}$$

where n_g is the group refractive index which is described by the first order dispersion as:

$$n_g = c\frac{dk}{d\omega} = n - \lambda\frac{dn}{d\lambda} \tag{2.14}$$

where n is the phase index and $\frac{dn}{d\lambda}$ is the phase index dispersion. As the group refractive index in Eq.2.13 is always larger than unity, the first order dispersion improves the axial resolution.

The second order dispersion $k^{(2)}(\omega_0)$ determines the group velocity dispersion, GVD, which is defined as:

$$\begin{aligned} GVD &= \frac{dn_g}{d\lambda} \\ &= \frac{d}{d\lambda}\left(n - \lambda\frac{dn}{d\lambda}\right) = -\lambda\frac{d^2 n}{d\lambda^2} = -\lambda\frac{2\pi\nu^3}{c}\frac{d^2 k}{d\omega^2} \end{aligned} \tag{2.15}$$

where c is the speed of light, and ν is the light frequency. The second and higher orders add a non-linear wavelength dependent phase, broadening the axial resolution. The third order dispersion $k^{(3)}(\omega_0)$ and higher orders contribute to the shape distortion of the coherence function. The orders higher than the third order dispersion are significant in achieving ultrahigh resolution OCT in tissue and water at wavelengths above 1 μm [74].

2.5.2 Dispersion Compensation

The dispersion imbalance between two interferometer arms has to be compensated to preserve axial resolution and avert reduced sensitivity. The proposed approaches for dispersion compensation are divided into two categories: hardware and software approaches.

Hardware approaches are widely used in balancing the dispersion between two interferometer arms. In this approach, a dispersive optical element equivalent to the dispersion properties of the testing sample is introduced in the reference arm to compensate the dispersion. The often used dispersion compensators are fused-silica or BK7 prisms. One standard technique is to deploy shifting prism pairs at the reference interferometer arm to compensate group velocity dispersion. A variable-thickness fused-silica prism pair compensates for the fiber length differences, and similarly a variable-thickness BK7 prism pair compensates for optical material mismatches between the interferometer arms [66]. Another approach is to use a fast optical delay line [75]. In other studies, a Fourier domain optical delay line was implemented to compensate for the second order dispersion [76, 77].

The main advantage of such hardware approaches is that no additional post-processing is required. Even if additional software dispersion compensation was required at post-processing stage, this hardware-based approach would be very helpful to reduce the amount of dispersion compensation performed by software. Despite these advantages, hardware techniques impose some challenges. First, the exact same dispersive material is required for compensation of dispersion orders higher than second order. This is sometimes hard to implement. Secondly, the sample dispersion is depth dependent; therefore, a dynamic dispersion compensation is required.

Apart from the aforementioned hardware techniques, several numerical algorithms have been proposed for dispersion compensation. Such numerical methods can be performed in direct space [78, 79] or in Fourier space [80, 81]. These numerical techniques can be used a posteriori and the dispersion compensation is performed dynamically. In this thesis, the automatic numerical dispersion compensation approach proposed by Wojtkowski et al. was employed [78]. The dispersion is first compensated by arranging a pair of dispersion-compensating prisms at the reference arm. The remaining dispersion was compensated by software through an iterative procedure, optimizing the sharpness of the images.

2.6 Summary

Three main OCT imaging methods, TD-, SD- and SS-OCT, together with their principles of operation were explained. The pros and cons of each imaging approach were discussed. In this chapter, the main attention was paid to FD-OCT imaging methods as all studies and experiments of the PhD thesis are based on these imaging approaches. The OCT scanning procedure to generate a 3D OCT volume was explained. The common OCT scanning terminology was described. The system resolution was presented in terms of axial and transverse resolution. The factors influencing the overall system resolution were explained in detail. The depth dependent sensitivity fall-off effect in OCT imaging systems was presented and illustrated. The parameters affecting the sensitivity fall-off were introduced, and improvement solutions were given. Finally, the dispersion concept was explained and the proposed dispersion compensation methods were reviewed.

Chapter 3

Spectrometer Design and Optimization

The overall performance of a typical spectral domain optical coherence tomography (SD-OCT) imaging system is dependent on several factors such as the chosen optical source, central wavelength, spectral bandwidth, spectrometer optical components and detector specifications. Among these factors, a good design and implementation of the spectrometer is of paramount importance, as it directly affects the system resolution, sensitivity fall-off, maximum imaging depth, SNR, and in general the system performance. This chapter describes the design steps of an OCT system's spectrometer to be used at CAP's lab of INESC TEC, and highlights some general considerations that should be taken into account during the design stage.

3.1 Introduction

As explained in section 2.1.2, the interference signal in SD-OCT imaging method is captured by a spectrometer at the detection arm of the interferometer, and reflectivity depth profiles are obtained by taking inverse Fourier transform from the acquired spectra [82]. So far, various spectrometer designs and configurations have been proposed for SD-OCT imaging systems. One common and conventional design is the deployment of refractive optical components in a spectrometer [83–85]. Such a widely used approach is bulky as the spectrometer's optical components are installed in free-space.

In another proposed design, the spectrometer's optical components were integrated on a single silicon chip to miniaturize spectrometer [86]. This approach has shown a good performance while reducing the size and cost [87–90]. Akca et al. demonstrated a silicon-oxynitride based arrayed waveguide grating (AWG) spectrometer to reduce the size and cost of the bulky free-space spectrometer [89]. Later, Akca et al. integrated the beam splitter and spectrometer into a silicon chip to miniaturize SD-OCT imaging system [86]. Apart

from reduced size and cost advantages, such an approach eliminates the need for accurate alignment of spectrometer's component.

Another reported configuration is the linear-in-wavenumber spectrometer, employing a prism after the diffraction grating to linearize the spectrum data in wavenumber [91]. This approach eliminates the numerical interpolation, decreases computational processing time and improves the depth dependent sensitivity fall-off. Apart from this deployment of prism, a spectrometer can be implemented by reflective optics, eliminating the chromatic aberration imposed by spectrometer's optical lenses. Kamal et al. proposed an all-reflective optics spectrometer consisting of a fold mirror, a grating, a cylindrical mirror and a line-scan detector in order to remove the chromatic aberration and increase the image quality [52, 92].

The following sections present optical design steps for a refractive optics-based spectrometer, covering a wavelength range of 1000-1100 nm, centered at $\sim$1050 nm. The designed spectrometer was implemented for a common path spectral domain optical coherence tomography (CP-SD-OCT) and a SD-OCT imaging system. For such a spectrometer, two different focusing optics configurations were designed and implemented.

3.2 Spectrometer Design

A typical SD-OCT spectrometer consists of four principal components: beam lead (a collimator), dispersive element (a diffraction grating), collection optics (a focusing lens) and detection (a line-scan camera). The detector specification is considered at the early stage of a spectrometer design since the constraints at this stage would affect other spectrometer components.

3.2.1 Detector

The spectrometer detector records a limited spectral bandwidth $\Delta\Lambda$ at a sampling density $\Delta\Lambda/N$, where N is the number of pixels of the used line-scan camera. In an optimized spectrometer design, the whole spectral bandwidth of the optical source is fully detected by the detector array with the highest pixel resolution possible to achieve a source limited axial resolution and maximum imaging range.

If the spectral bandwidth observed by the detector is too small, the entire spectral bandwidth of the optical source cannot be detected. This happening yields in degradation of the axial resolution and increase of imaging range. In this case, the actual axial resolution of the imaging system is less that its theoretical limit defined by Eq.2.5. On the other hand, if the detector's spectral bandwidth is too large, the sampling density will be reduced, resulting

in decreased imaging range. In this case, the axial resolution would remain unchanged and would be limited by the specification of the optical source.

Therefore, there is always a trade off between the axial resolution and the imaging range. An optimized approach is to choose $\Delta\Lambda$ such that optical source limited axial resolution can be obtained without compromising the imaging range. Thus, the axial resolution and the maximum imaging depth are determined at the initial stage of the design.

The employed light source has a central wavelength at approximately 1050 nm, a FWHM of 50 nm, and a 10 dB bandwidth of 70 nm. In the context of this chapter, a range between $\lambda_{min} = 1000$ nm and $\lambda_{max} = 1100$ nm was considered. As discussed in section 2.3.1, the axial resolution is specified by the coherence length of the light source and is calculated by Eq.2.5. Considering the given light source, the computed theoretical axial resolution in air is $\sim 9.73\ \mu m$.

The maximum imaging depth is determined by the optical source parameters and the total number of pixels of the detector. It is also limited by the scattering and absorption properties of the interrogated sample as such phenomena degrade light propagation along the sample.

Considering the axial pixel spacing as half of the theoretical axial resolution ($\Delta z/2$) allows the two closely spaced peaks can be resolvable by Δz. Otherwise, such peaks cannot be distinguished if the axial pixel spacing is less than $\Delta z/2$. Therefore, by choosing the pixel spacing as half of the theoretical axial resolution, the imaging depth is maximized while the axial resolution is maintained. If the absorption and scattering properties of the testing sample are excluded, the maximum imaging depth can be expressed as [78]:

$$\begin{aligned} z_{max} &= \frac{\Delta z}{2}\frac{N}{2} \\ &= \frac{ln2}{2\pi}\frac{\lambda_0^2}{\Delta\lambda}N \end{aligned} \tag{3.1}$$

where N is the number of pixels of the line-scan camera. N is divided by 2 as only half of the pixels contain unique information after taking the inverse Fourier transform. Eq.3.1 demonstrates that a wise balance between the axial resolution and the maximum imaging depth should be taken into account during the design of a spectrometer. Using the employed optical source parameters and assuming $N = 2048$ pixels in Eq.3.1, the theoretical maximum imaging depth is calculated as $\sim 5\ mm$.

Another important issue taken into account during selection of the line-scan camera is the spectral responsivity of the chosen detector. The spectral responsivity curves express the quantum efficiency of the detector as a function of wavelength. The detector requires

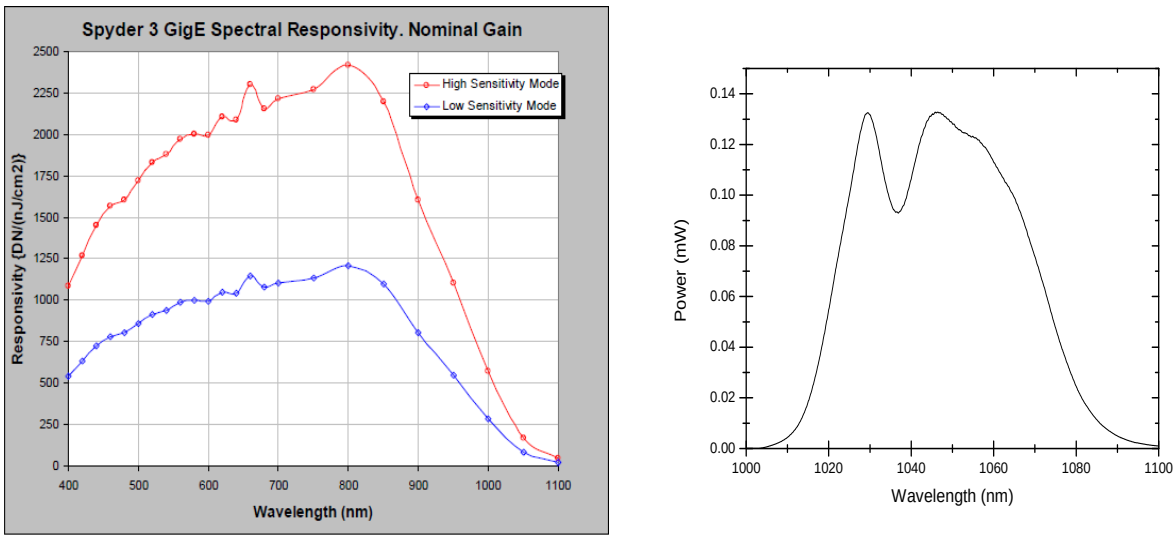

(a) (b)

Figure 3.1: (a) The spectral responsivity of the Dalsa SG-10-02K80-00-R Spyder3 GigE line-scan camera within the wavelength region of 400-1100 nm in two operating modes: low and high sensitivity modes. (b) Optical source spectrum within the wavelength region of 1000-1100 nm.

good spectral responsivity within the spectral bandwidth of the employed optical source. A commercial DALSA SG-10-02K80-00-R Spyder3 GigE line-scan camera was considered. It is a 12-bit camera with 36 kHz line rate and the total number of 2048 pixels, each pixel size is 14 $\mu m \times 14\ \mu m$. Fig.3.1 illustrates (a) the spectral response of the camera within the wavelength region of 400-1100 nm in two operating modes of low and high sensitivity [93], and (b) the optical spectrum of the used source within the wavelength region of 1000-1100 nm. The camera has the highest responsivity in the region of 800 nm, and the spectral responsivity decays dramatically within the wavelength region of 1000 – 1100 nm. Considering the availability of limited optical components in CAP's lab during the design and implementation of the spectrometer and high cost of InGaAs line-scan cameras, this camera was employed.

3.2.2 Diffraction Grating

A prism or a grating can be employed to spectrally disperse the light over the detector. A grating is normally used as it has two distinct advantages. First, it provides higher spectral resolution than prism. Secondly, it is less bulky. The properties of the grating strongly influence the spectrometer resolution. Gratings are defined by their resolving power (R) which is a dimensionless number and is given by [94, 95]:

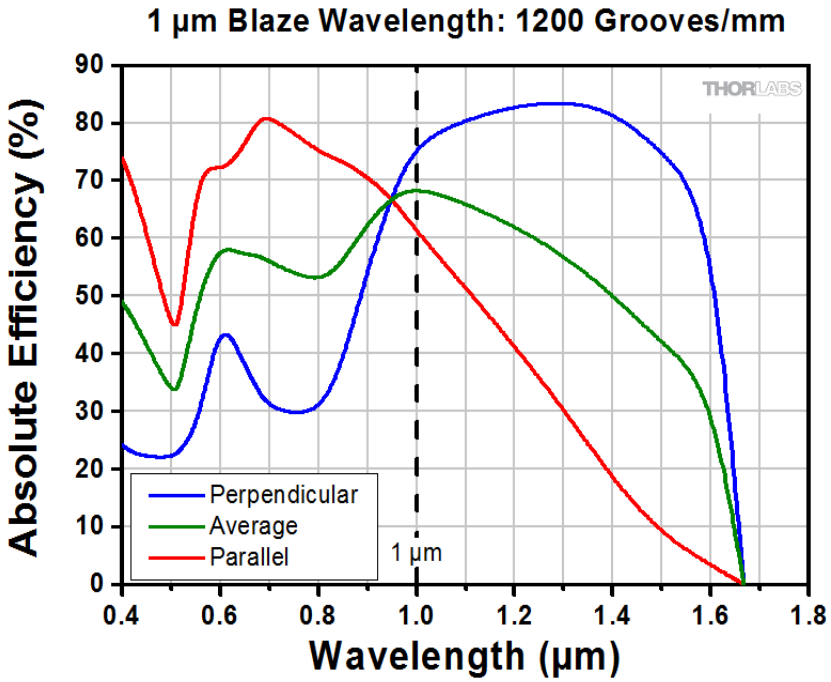

Figure 3.2: The efficiency curves of the identified ruled reflective diffraction grating, $1200\,grooves/mm$, $1\,\mu m$ blaze, and size of $25\,mm \times 25\,mm$.

$$R = \frac{\lambda}{\delta\lambda} = mM \tag{3.2}$$

where λ is the maximum wavelength, $\delta\lambda$ is the maximum achievable spectral resolution of the grating, m is the diffraction order, and M is the total number of grooves illuminated on the grating surface. Most gratings are first orders, meaning they are highly efficient at first diffraction order. Assuming $m = 1$ and $\lambda = \lambda_{max} = 1100\,nm$, to realize a spectral resolution of $\delta\lambda = (\lambda_{max} - \lambda_{min})/N = 0.048\,nm$, the total number of illuminated grooves is obtained as $22,916$. Therefore, if a groove density of $1200\,mm^{-1}$ is chosen, the beam diameter or in other words the minimum aperture size for the collimating lens must be at least $22,916/1200 = 19.09\,mm$.

The next issue to be taken into account is the grating efficiency. Fig.3.2 demonstrates the efficiency curves of the selected diffraction grating [96]. As shown in Fig.3.2, grating efficiency is a function of wavelength and polarization of the incident light. Considering the calculated beam diameter and the efficiency plot of various gratings, a ruled reflective diffraction grating of 1200 grooves/mm with the size of 25 mm $\times$ 25 mm was chosen.

Before determining the collimating and focusing optics, the angular dispersion of the

grating is computed. This angular dispersion is obtained by the grating equation defined as [94, 95]:

$$\sin(\theta_i) + \sin(\theta_d) = mG\lambda \tag{3.3}$$

where θ_i is the incident angle of the light, θ_d is the dispersion angle, m is the diffraction order and G is the groove density. The optimal efficiency is achieved for a specific geometry of the grating in which the dispersed light travels back along the direction of the incident light ($\theta_i = \theta_d$). This condition is known as Littrow condition. Hence, the grating equation simplifies for Littrow configuration as [94, 95]:

$$\sin(\theta_i) = \sin(\theta_d) = \frac{mG\lambda}{2} \tag{3.4}$$

Considering such a condition, and assuming $m = 1$ and $G = 1200\,mm^{-1}$, the dispersion angle for minimum ($\lambda_{min} = 1000$ nm), central ($\lambda_0 = 1050$ nm), and maximum ($\lambda_{max} = 1100$ nm) wavelength was obtained as 36.86°, 39.05° and 41.29°, respectively. Therefore, for Littrow configuration, the spectrum from 1000 nm – 1100 nm is dispersed at $\theta_d = 39.05^\circ \pm 2.2^\circ$.

The grating was placed as close as possible to Littrow angle for the sake of efficiency. The measured incident angle of the light was approximately $49^\circ \pm 2$. Using Eq.3.3, the dispersion angle for minimum, central, and maximum wavelength was calculated as 26.44°, 30.35° and 34.42°, respectively; thus, the spectrum from 1000 nm – 1100 nm is dispersed at $\theta_d = 30.35^\circ \pm \sim 4^\circ$.

3.2.3 Collimating Optics

To determine the collimating lens, the angular aperture (θ) of the beam exiting the fiber was first calculated. The angle depends on the numerical aperture (NA) of the fiber and refractive index of the medium through which the light travels [94].

$$NA = n\sin(\theta) \tag{3.5}$$

The numerical aperture of the used single mode fiber is 0.13. The light exits the fiber into the air ($n = 1$); hence, θ is obtained as 7.5 degrees. Using a simple geometry formula, the focal length for the collimating lens f_c is:

$$\tan(7.5) = \frac{19.09/2}{f_c}$$
$$f_c = 72.5\ mm$$

Therefore, a 1-inch achromatic doublet lens with the focal length of 75 mm was selected to collimate the beam and also to accommodate the calculated beam diameter, averting the degradation of the spectrometer resolution.

3.2.4 Focusing Optics

Two configurations were considered to implement the focusing optics: (A) single lens, (B) double lens for compact assembly.

- Configuration A consists of a single 2-inch achromatic doublet lens, with focal length of 80 mm.
- Configuration B is a combination of a converging and a diverging lens. In this design, the focusing optics comprises of a 2-inch achromatic doublet lens with the focal distance of 80 mm (the same lens as configuration A) and a 1-inch achromatic doublet lens with the focal distance of -50 mm.

Both designed configurations were simulated by using WinLens optical design software [97]. The simulations are illustrated in Fig.3.3. As it is shown in Fig.3.3, configuration B covers 26.22 mm out of the total length of 28.67 mm of the line-scan camera while the image height of configuration A is only 11.26 mm. The negative lens in configuration B was deployed to further expand the beam so that larger area of the line-scan camera can be covered.

In the next step, the image plane shown in Fig.3.3 was defocused at several positions to achieve an optimized position for the objective lens and the detector while minimizing the spot size of the beam on the detector. The defocus positions of -0.33 mm and -1.85 mm were considered for configuration A and B, respectively. The corresponding spot diagrams for both configurations demonstrating the spot patterns at different angles and defocus positions are shown in Fig.3.4. A numerical summary of the RMS spot size at various ray angles assists to better optimize the position of the objective lens relative to the line-scan camera while altering the defocus position. The numerical summary is given in Table 3.1.

In configuration A, the obtained results revealed that the spot size is less than the pixel size of the line-scan camera for on axis beams, and the size increases with the increase of

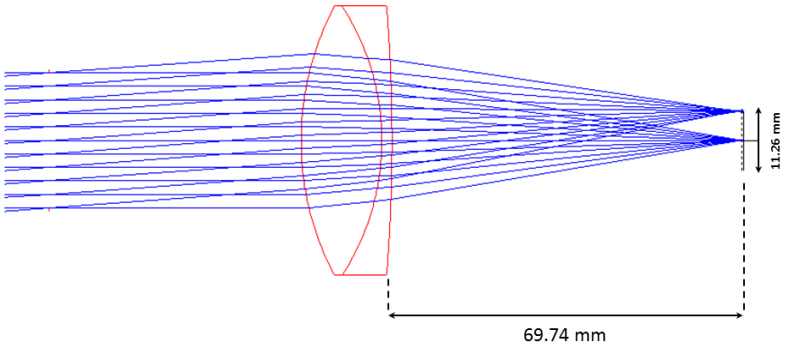

A

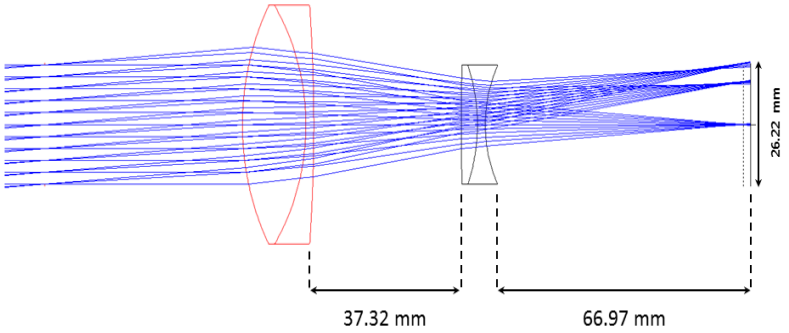

B

Figure 3.3: WinLens simulation of two configurations for focusing optics: (A) a single converging lens, (B) a combination of a converging and a diverging lens.

Ray Angle [Transverse Position]	0.0 deg [0.0]	0.7 deg [-0.18]	1.4 deg [-0.35]	2.1 deg [-0.53]
Configuration A (defocus position at -0.33 mm)				
$\sqrt{dx^2+dy^2}$	0.0125	0.0141	0.0197	0.0301
dy	0.0088	0.0092	0.0105	0.0136
Configuration B (defocus position at -1.85 mm)				
$\sqrt{dx^2+dy^2}$	0.0280	0.0399	0.0664	0.1024
dy	0.0198	0.0216	0.0266	0.0347

Table 3.1: Numerical summary of the RMS spot size at various ray angles. All values are expressed in mm unit.

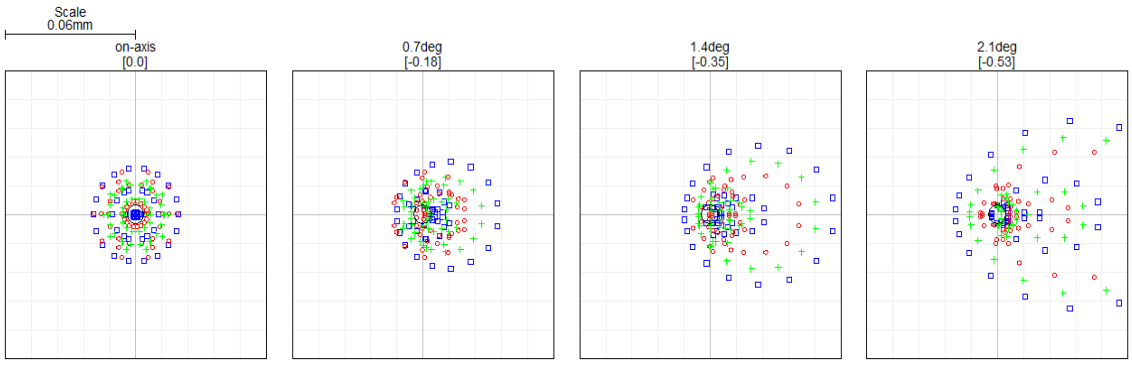

(a) Configuration A

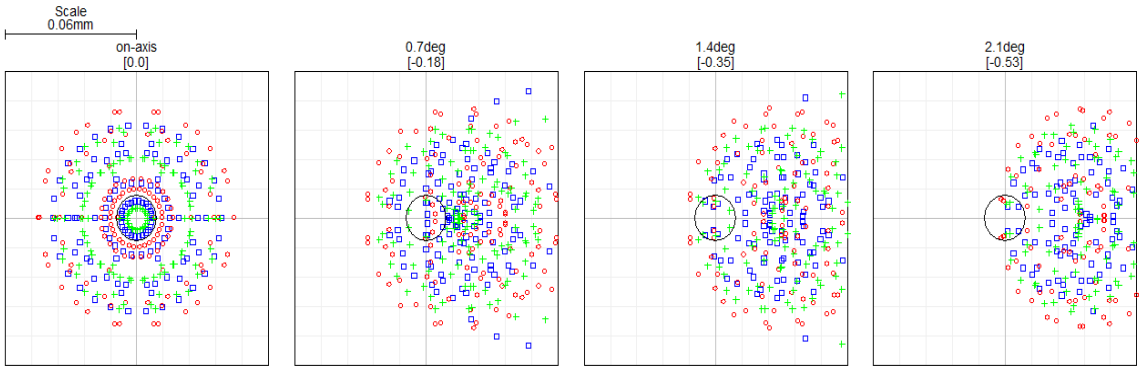

(b) Configuration B

Figure 3.4: Spot diagrams of the simulated focusing optics at various angular positions in image plane for two configurations: (a) the single objective lens and (b) the converging and the diverging objective lenses. The values inside the square brackets indicate transverse positions, expressed in mm unit. The black circle, the blue square, the green cross, and the red circle symbols denote the airy disc, short, mid and long wavelengths of the employed optical source, respectively.

the ray angle. In addition, the dy values of configuration A proved that the vertical pixel size of the camera is good enough to cover the spot size in vertical direction at all ray angles. In configuration B, the RMS spot size is twice of the pixel size of the camera for on axis beams, and by the increase of ray angles, the spot size increases. The dy values also exceeded the pixel height of the camera. The camera has an operating mode known as tall pixel mode in which the camera uses two line scan sensors to detect the beam. In this mode, each pixel is taller, covering a size of 14 $\mu m \times 28$ μm (width$\times$height). Therefore, two adjacent pixels in tall pixel mode would cover the spot size in vertical direction but with leaning to the horizontal.

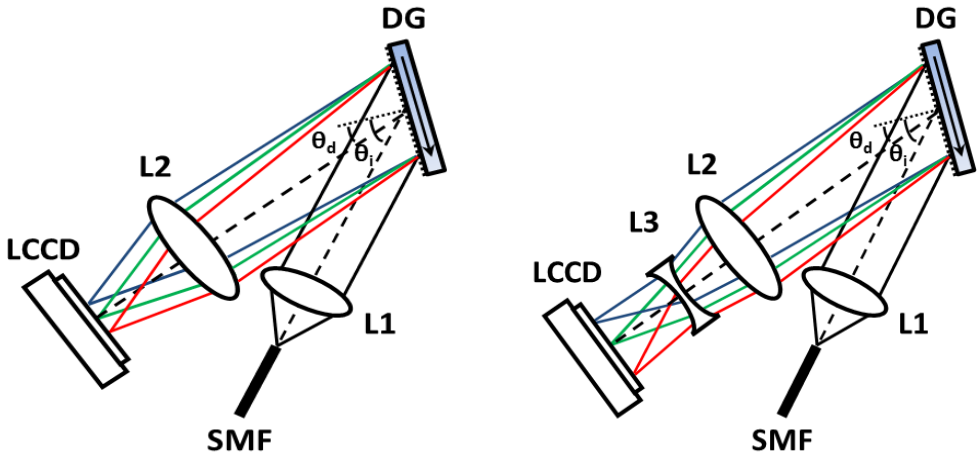

(a) (b)

Figure 3.5: Diagrams of two different spectrometer configurations: (a) Spectrometer of the CP-SD-OCT system, (b) Spectrometer of the SD-OCT system. SMF: single mode fiber, L1-3: achromatic doublet lenses, DG: ruled reflective diffraction grating (the arrow shows the direction of the blaze arrow), θ_i: incident angle ($\sim 49^\circ$), θ_d: dispersion angle ($\sim 30^\circ$), LCCD: line-scan charge coupled device camera.

3.3 Spectrometer Configuration

A schematic diagram of both spectrometer configurations are shown in Fig.3.5 and the optical components employed to implement these two configurations are summarized in Table 3.2 with their acronyms used throughout this section.

The single mode fiber (SMF) depicted in Fig.3.5 is connected to the spectrometer. The emerged light from the SMF is first collimated by the achromatic doublet lens with the focal length of 75 mm (L1). The collimated light is next dispersed by the ruled reflective diffraction grating of 1200 grooves/mm with the size of 25 mm × 25mm (DG). In configuration A, the dispersed light is focused on the line-scan charge coupled device camera (LCCD) with 2048 pixels, 12-bit resolution, and 36 kHz line rate by the achromatic doublet lens with the focal length of 80 mm (L2). In configuration B, two achromatic doublet lenses were considered. The first lens is a converging lens with the same specification as the objective lens used in configuration A. The second lens is a diverging achromatic doublet lens with the focal length of -50 mm (L3), further expanding the beam to cover the line length of the camera.

Table 3.2: The optical components employed for the implementation of the CP-SD-OCT and SD-OCT imaging systems.

Acronym	Description	Part number	Manufacturer
L1	Achromatic doublet lens, f = 75 mm	AC254-075-B	Thorlabs
L2	Achromatic doublet lens, f = 80 mm	AC508-080-B	Thorlabs
L3	Achromatic doublet lens, f = -50 mm	ACN254-050B	Thorlabs
L4	FC/APC fiber collimator, f = 15.43 mm	F260APC-1064	Thorlabs
L5	Achromatic doublet lens, f = 30 mm	AC254-030-B-ML	Thorlabs
L6	Achromatic doublet lens, f = 75 mm	AC254-075-B-ML	Thorlabs
SH	Sensing head, FC/PC collimation package, f = 36.6 mm	F810FC-1064	Thorlabs
RC	Reflective collimator	RC08APC-P01	Thorlabs
SM	Galvanometric scanning mirror	6220H -Au	Cambridge
DG	Ruled reflective diffraction grating, 1200 grooves/mm	GR25-1210	Thorlabs
LCCD	Line-scan charge coupled device camera, 2048 pixels, 12-bit, line rate 36 kHz	SG-14-02K80	Teledyne DALSA
BOS	Broadband optical source, $\lambda_0 = 1050\ nm$, $\Delta\lambda = 50\ nm$	BBS-1um-22-L	Multiwave Photonics
PC	Polarization controller	PLC-003-S-25	General Photonics
DC1	Directional coupler, splitting ratio 50:50	WP10500202B2111-UP1	AC Photonics
DC2	Directional coupler, splitting ratio 67:33	WP10500202B2111-UP1	AC Photonics
MTS	Motorized translation stage, 20 mm travel range, $0.1\,\mu m$ resolution	M-663.465	Physik Instrumente
OC	Optical circulator	PIOC31060P2431	AC Photonics

Table 3.2: The optical components employed for the implementation of the CP-SD-OCT and SD-OCT imaging systems.

Acronym	Description	Part number	Manufacturer
NDF	Mounted continuously variable neutral density filter, 25 mm, optical density range: 0.0 - 4.0	NDC-25C-4M	Thorlabs
DCPP	Dispersion-compensating prism pair, equilateral dispersing prisms, angles 60°, material BK7	01PES001	Melles Griot
FM	Fiber mirror reflector	FMR10982SC1	Thorlabs

3.4 Summary

This chapter highlighted the importance role of spectrometer design for SD-OCT imaging system in obtaining high quality OCT images. The necessary design steps together with some general considerations to design a spectrometer were explained. The direct effect of some optical components of an OCT imaging system affecting the specification of a spectrometer was described. Some of these discussed critical components include the chosen optical source, central wavelength and wavelength bandwidths, the diffraction grating, and the line-scan camera, influencing the spectrometer's performance.

An approach to properly select a collimating optics was introduced in this chapter. Two different configurations were proposed for the focusing optics of the spectrometer. Both focusing optics designs were simulated by employing WinLens optical design software. The position of the objective lens and the camera were optimized by using such simulations. The spot size was minimized by altering the distance between the objective lens and the line-scan camera, and defocusing the image plane to lessen the sensitivity fall-off effect.

The implemented spectrometer configuration A and B were integrated into a CP-SD-OCT and a SD-OCT imaging system, respectively. It was essential to design and implement such spectrometers in order to improve the performance parameters of the existing spectrometer in CAP's lab. Such an optimization increased the resolution and imaging range of the imaging systems, enabling imaging of micro multilayered structures with micron scale resolution. The CP-SD-OCT system is later employed to perform 1D imaging of various samples. These 1D imaging conducted to measure the thickness of laminated samples. The spectrometer's improvement also ameliorated the performance of the SD-OCT imaging sys-

tem, allowing the generation of higher quality cross-sectional images of examined samples. The enhanced imaging systems are demonstrated in Chapters 5 and 7, and the performance characterization results of such improved imaging systems are shown in sections 5.2 and 7.3 of this thesis.

Chapter 4

Numerical Study on Calibration and Re-Sampling Methods

In this chapter, a spectral calibration technique, a data processing method and the importance of calibration and re-sampling methods for the spectral domain optical coherence tomography system are numerically studied. Accurately assigning the wavelength to each pixel of the detector is of paramount importance to enhance the quality of resulting images and increase SNR. The calibration method is performed by phase calibration and interpolation. In addition, SNR is assessed by employing two approaches, single spectrum moving window averaging and consecutive spectra data averaging, to investigate an optimized method and factor for background noise reduction. The content of this chapter is published in Photonic Sensors, a peer-reviewed open access journal.

4.1 Introduction

In SD-OCT, the detected light intensity back reflected from sample is a function of wavelength, $I(\lambda)$. As discussed in section 2.1.2, the sample's reflectivity depth profile, or A-scan, is obtained by applying an inverse Fourier transform over the detected spectral fringes modeled by Eq.2.1. Since there is a nonlinear relationship between wavelength (λ) and wevenumber (k), and the sampled data is often almost evenly spaced in $\lambda - space$ (spectrometer detection), it will be then not evenly spaced in $k - space$. Therefore, in order to achieve the highest image quality, the data has to be re-sampled in an equally spaced $k - space$ prior to applying the inverse Fourier Transform. Otherwise, applying the inverse FFT to the unevenly spaced data would result in the broadening of the Fourier transformed signal, and consequently blurred images. Numerous approaches have been proposed for re-sampling of

the spectral data. These approaches fall into two categories: hardware and software solutions.

As an optics hardware solution, SD-OCT linear-in-wavenumber spectrometers were developed to obtain real time imaging and avert time-consuming re-sampling calculations [91, 98]. The detection arm is modified by using a customized prism placed directly after the diffraction grating to evenly disperse the spectrum in wavenumber. In SS-OCT, an external k-trigger electronic board allows the acquisition of uniformly sampled data in $k-space$ [99]. The proposed hardware approaches eliminate the need for numerical re-sampling, thus reducing computing time. However, these methods impose additional cost.

Software solutions are widely used for calibration and re-sampling of the acquired spectral fringes. Numerous approaches have been proposed in order to achieve the best performance, for both OCT signal quality, as well as computational efficiency. One suggested approach for spectral calibration is to use spectral calibration information extracted from the interference spectra at two different known positions [100, 101]. This eliminates the impact of dispersion mismatch between two interferometer arms and thus accurately assigns the wavelength to each pixel in the detector. After performing the calibration, a basic linear interpolation method is applied to make data uniform in $k-space$ [102, 103]. However, this method usually causes errors at greater depth [104]. In another approach, to correct such an error, the data processing method is carried out by applying a Discrete Fourier Transform (DFT), zero padding to increase the resolution by increasing the data array length, inverse DFT and then re-sampling of the resultant data at regular intervals in $k-space$ [105, 106].

The most popular re-sampling method offering the best cost-performance among the available interpolation methods is the cubic B-spline interpolation [13, 78, 107]. This method is more accurate; however, it is computationally expensive. The graphics processing unit (GPU)-based data processing algorithms have been proposed to resolve the computation time problem of such re-sampling methods and achieve a real-time data processing [108, 109]. Such GPU-based processing techniques are described in more detail in Chapters 6 and 7.

The following sections detail the numerical study of spectral calibration and data processing techniques to be employed in SD- and SS-OCT imaging systems, and for future implementation in GPU architecture, as discussed in Chapter 7. In this analysis, white noise was added to the signal, and SNR was assessed from two numerical background noise minimization approaches: moving window over spectrum averaging, and consecutive spectra data averaging.

4.2 Calibration Theory

In SD-OCT, the total signal detected at pixel n of a line-scan charge coupled device camera detector (LCCD) includes the incoherent superposition of reference and sample electromagnetic fields, and the coherent superposition of reference and sample fields encoding the reflectivity information along depth of the object. From Eq.2.1, the resulting signal $I(\lambda_n)$ can be expressed as [100]:

$$I(\lambda_n) = s(\lambda_n)\left(a_r^2 + a_s^2\right) + 2\,a_r\,a_s\,s(\lambda_n)\cos\left(\frac{2\pi}{\lambda_n}z + g(\lambda_n)\right) \tag{4.1}$$

where λ_n is the wavelength assigned to pixel n, a_r and a_s are the reflection coefficients of the reference mirror and sample (at z OPD) respectively, $s(\lambda_n)$ is the spectral shape of the light source, and $g(\lambda_n)$ is the dispersion mismatch between the two optical paths. The first two terms can be removed by proper subtraction of the background intensities. The desired information is thus encoded in the last interference term that includes the existence of the dispersion mismatch term:

$$\begin{aligned} I_{interf.}(\lambda_n) &= 2\,a_r\,a_s\,s(\lambda_n)\cos\left(\frac{2\pi}{\lambda_n}z + g(\lambda_n)\right) \\ &= 2\,a_r\,a_s\,s(\lambda_n)\cos\left(\phi(k_n)\right) \end{aligned} \tag{4.2}$$

The spectral calibration in this study is performed by a phase fitting method. First, the phase of Eq.4.2 at optical path difference (OPD) z_1 is extracted using the Hilbert transform [110]. The same procedure is repeated for optical path difference z_2. The difference between two phases ($\Delta\phi_n$) is calculated. Wavenumber (k_n) is obtained by:

$$k_n = \frac{\Delta\phi_n}{\Delta z} \tag{4.3}$$

where $\Delta z = z_2 - z_1$. The subtraction of two phases taken from the signal acquired at two different optical path lengths eliminates the impact of the dispersion mismatch, since $g(\lambda_n)$ function is the same as the optical path length changes. The resulting phase vector, size N, is fitted by a polynomial as a function of k. The attained polynomial coefficients are known as the calibration coefficients, and the corresponding curve may then be used to determine the interpolation points prior to inverse Fourier transform. The following section presents the numerical simulations for these procedures for a typical SD-OCT system.

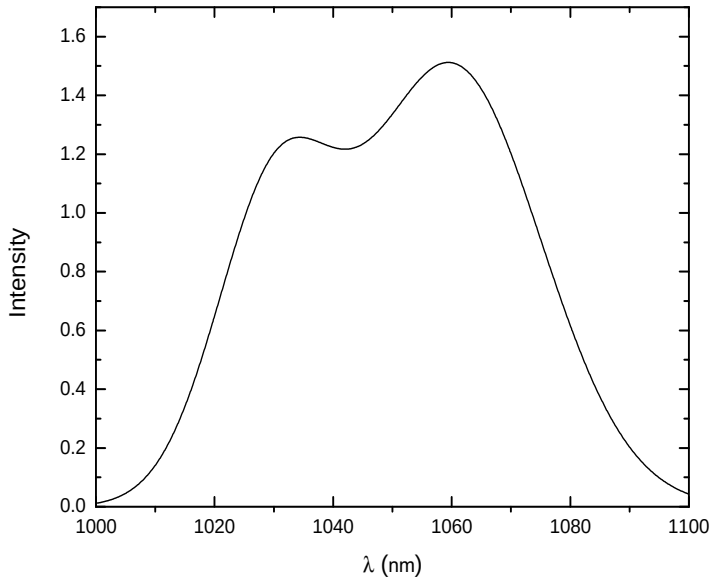

Figure 4.1: Simulated source spectrum $s(\lambda_n)$ using the parameters shown in Table 4.1.

4.3 Simulations

All signal processing procedures were implemented under LabVIEW^{TM} 2011 software as it has a flexible graphical programming environment, easing the implementation, monitoring, and debugging each signal processing step.

4.3.1 Calibration

The source spectrum, $s(\lambda_n)$, was simulated based on the optical source used at CAP's laboratory of INESC TEC. Such a simulation was performed by adding two Gaussian functions using the parameters shown in Table 4.1.

$$s(\lambda_n) = A_1 \exp\left(\frac{-\left(\lambda_n - \bar{\lambda}_1\right)^2}{2b_1^2}\right) + A_2 \exp\left(\frac{-\left(\lambda_n - \bar{\lambda}_2\right)^2}{2b_2^2}\right) \tag{4.4}$$

where A_1 and A_2 indicate the amplitude, $\bar{\lambda}_1$ and $\bar{\lambda}_2$ are the central wavelengths, and b_1 and b_2 are the standard deviations of the Gaussian functions; λ_n is changing from λ_{min} to λ_{max} in steps of $(\lambda_{min} + \lambda_{max})/N$ where N is the number of pixels at the LCCD. The simulated source spectrum is demonstrated in Fig.4.1, emulating the optical source spectrum shown

in Fig3.1.b.

Following Eq.4.2, the photo-detected signal corresponding to an optical path difference z is simulated by modulation of $s(\lambda_n)$ by a cosine function as:

$$I(\lambda_n) = s(\lambda_n)\left(\cos\left(\frac{2\pi z}{\lambda_n}\right) + DC\right) \tag{4.5}$$

The simulation of the corresponding detected signal using the parameters in Table 4.1 is shown in Fig.4.2. The *DC* constant was set to 0, emulating the signal after background removal. The vector k_n is obtained by Eq.4.3, with $\Delta z = 400\ \mu m$. The unwrapped phase obtained from the Hilbert transform with a reflecting surface at $z = 900\ \mu m$ is shown in Fig.4.3. The difference of two phase signals acquired for optical path length differences $z_1 = 500\ \mu m$ and $z_2 = 900\ \mu m$ is computed.

The vector of N containing the interpolation data points as a function of k, $N(k)$, was fitted by a polynomial order of 3. As shown in Fig.4.4, there is a non-linear relation between wavenumber and pixel number, confirming the need for data interpolation prior to FFT. In the simulated case, the obtained calibration curve and coefficients are as:

$$N(k) = 0.927442 + 1.63133 \times 10^6 k + 2.50773 \times 10^8 k^2 + 5.66137 \times 10^{10} k^3$$

After this polynomial fitting step, the attained calibration coefficients can be used to perform the evenly k-spaced interpolation. These points versus wavenumber k are demonstrated in Fig.4.4.

Parameter	Value	Parameter	Value
A_1	1	A_2	1.5
b_1	10	b_2	15
λ_{min}	1000 nm	λ_{max}	1100 nm
λ_1	1030 nm	λ_2	1060 nm
N	1024	DC	0
z	300 μm		

Table 4.1: The parameters and values, similar to those parameters of the employed source at CAP's lab, for simulation of the detected interference signal.

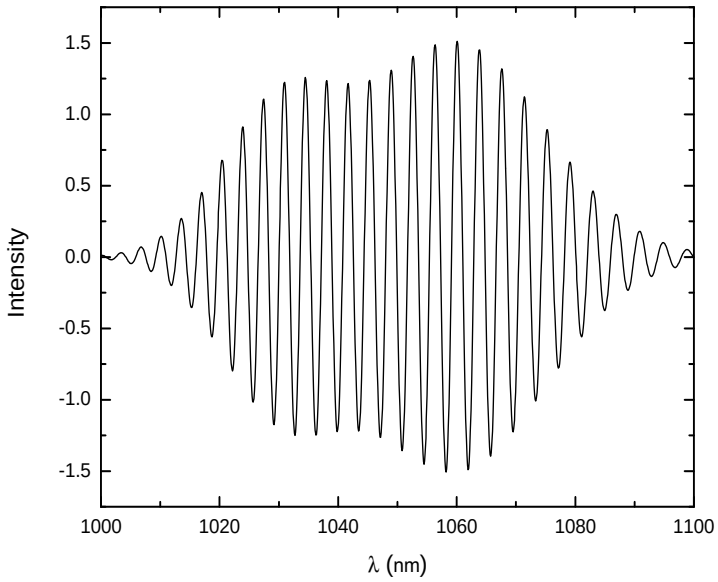

Figure 4.2: Simulated detected signal using values in Table 4.1.

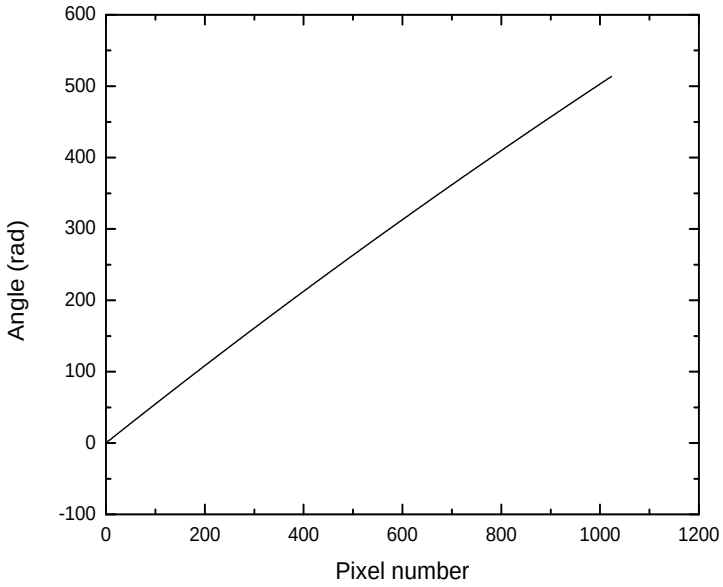

Figure 4.3: The unwrapped phase at $z = 900\,\mu m$.

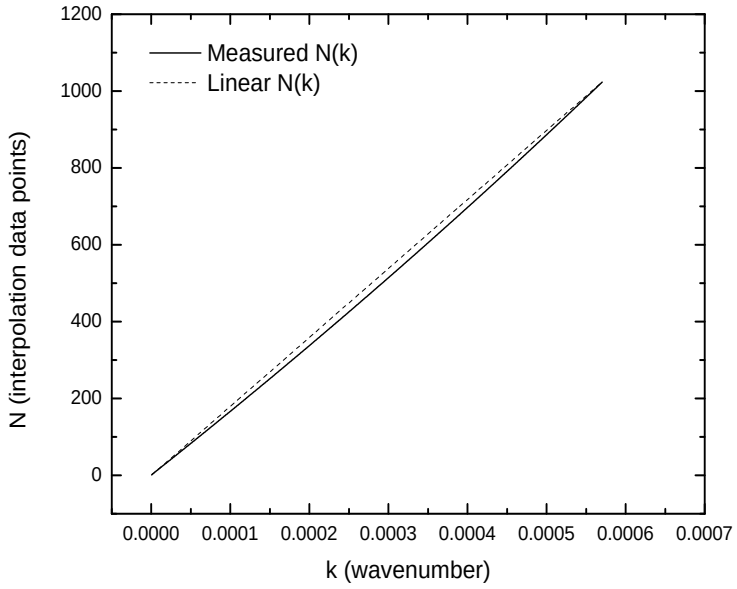

Figure 4.4: The interpolation data points versus k. The solid and dashed line demonstrate the measured wavenumber and the linear wavenumber versus the interpolation data points, respectively.

4.3.2 Multiple Reflections

Three reflecting surfaces along the sample arm were considered with total optical path difference z_1, z_2 and z_3. These reflecting surfaces emulate multilayerd structures of a testing sample. The resulting signal was implemented from Eq.4.4 as:

$$I(\lambda_n) = \sum_{i=1,2,3} s(\lambda_n) \times \left\{ R_i \cos\left(\frac{2\pi z_i}{\lambda_n}\right) + DC \right\} \tag{4.6}$$

where z_i is the optical path length difference associated to the light reflected at layer i contributing to the signal, and R_i is an array of three elements corresponding to the reflectivity of each layer. In this simulation, the background term was considered as a constant number, the DC term. Using Eq.4.6 and values mentioned in Tables 4.1 and 4.2, the photo-detected signal was simulated and demonstrated in Fig.4.5. The DC term was set to 1 to add a DC signal to the simulated signal.

The calibration coefficients obtained in section 4.3.1 were used to determine the interpolation points of the raw data to a regularly $k-spaced$ corrected signal. The data was inter-

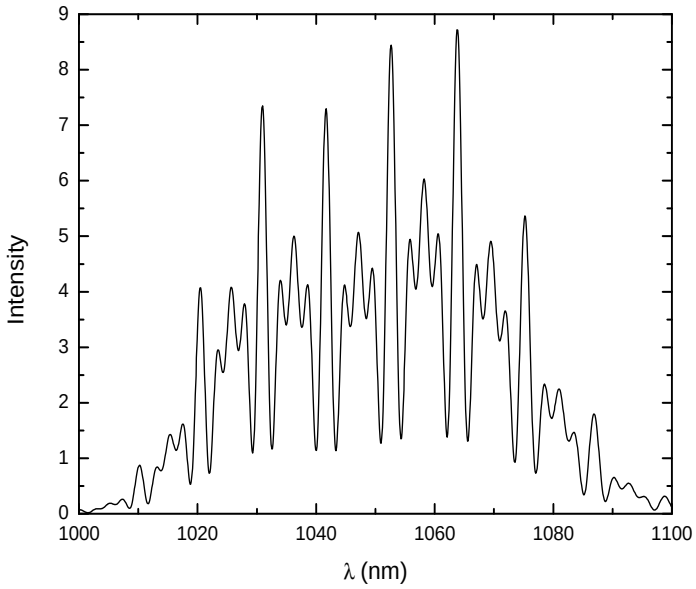

Figure 4.5: Simulated photo-detected signal of three reflecting surfaces using values in Tables 4.1 and 4.2.

polated with cubic B-spline for 1024 evenly spaced k points. Fig.4.6 shows non-interpolated and resulting interpolated data spectra.

The interpolated data was zero padded to increase the resolution of the inverse Fourier transformed signal. The number of zero points was chosen as a power of two, since the FFT algorithm requires an input that has a power of two length for optimized Fourier transform calculations. The depth profile was finally achieved by applying inverse FFT to the zero-padded data. The rescaling factor of $2\pi/\Delta k$ (where Δk is the difference between k_{min} and k_{max} obtained from calibration stage) was required to coordinate the peaks representing each

Parameter	Value
z_1	200 μm
z_2	300 μm
z_3	400 μm
DC	1
$R_{1,2,3}$	1, 1, 1

Table 4.2: The parameters and values for simulation of detected interference signal consisting of three reflecting surfaces.

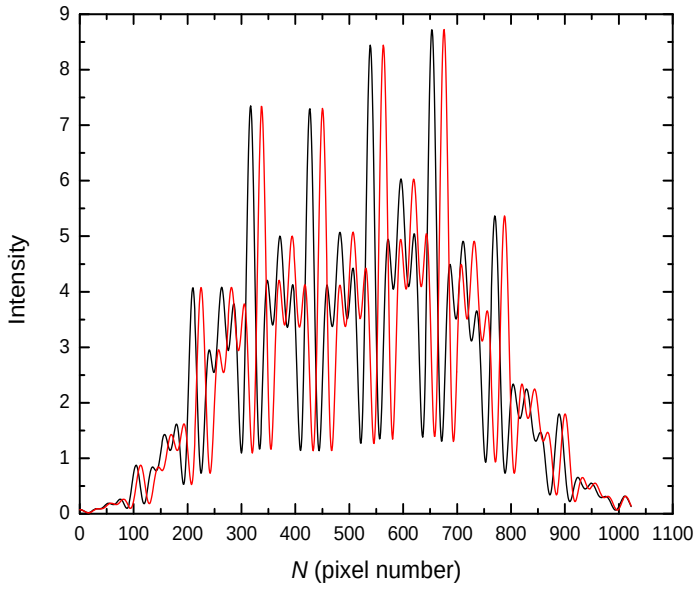

Figure 4.6: Non-interpolated (black line) and interpolated (red line) data spectrum, as a function of pixel number in wavenumber space, and k-space, respectively.

reflecting surface at the right position along the $x-axis$ in the reflectivity depth profile. Fig.4.7 demonstrates the reflectivity depth profile obtained for three reflecting surfaces at OPDs $z = 200$, 300 and 400 μm.

Considering different reflectivity factors for each layer, the reflection coefficient of the three surfaces was set as 0.9, 0.75 and 0.6 respectively. The resultant reflectivity depth profile is demonstrated in Fig.4.8. All simulations do not take into account the fringe wash-out with depth caused by the finite spectrometer resolution. Fig.4.8 illustrates that the peak amplitudes corresponding to each reflecting surface of the testing sample are proportional to their reflection coefficients.

4.3.3 Additive Noise

The photo-detected signal of three reflecting surfaces contaminated by uniform white noise of unity amplitude was simulated and shown in Fig.4.9. Parameter values mentioned in Tables 4.1 and 4.2 were used in this simulation.

Using the same calibration coefficients obtained from calibration section 4.3.1, 1024 interpolation points were computed. The simulated interference data was then interpolated employing these new points. Fig.4.10 demonstrates a non-interpolated and an interpolated

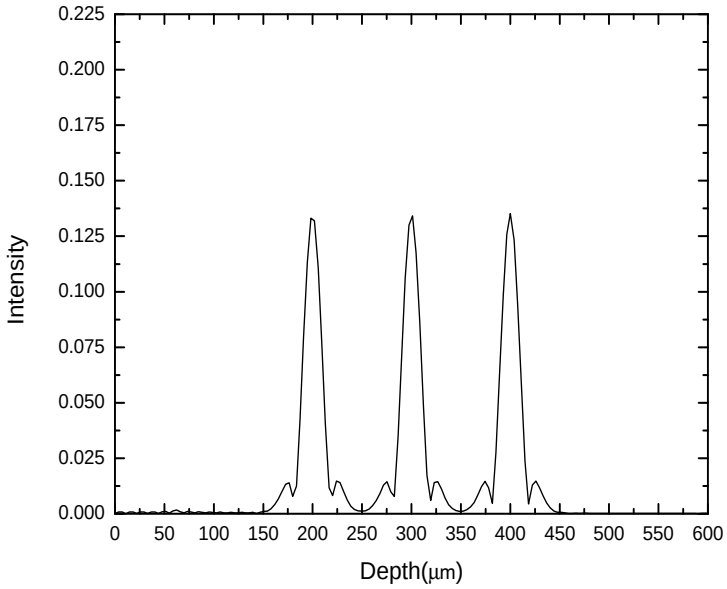

Figure 4.7: The reflectivity depth profile demonstrating three reflecting surfaces at $z = 200$, 300 and 400 μm.

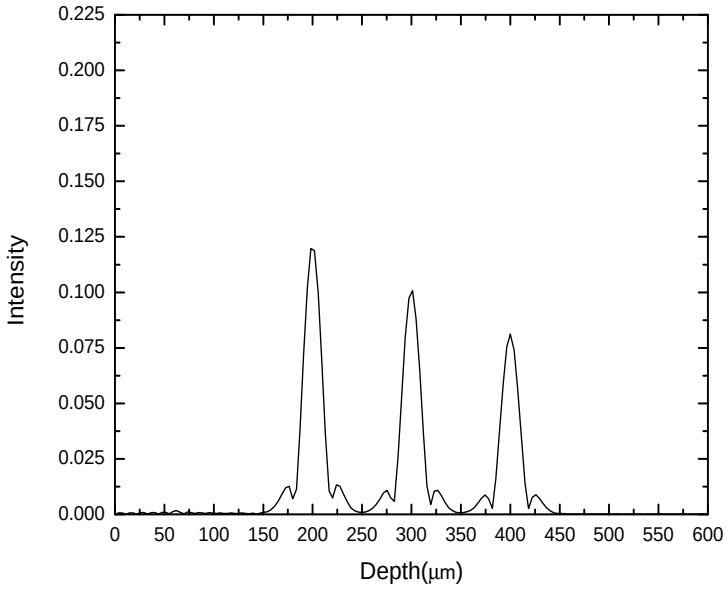

Figure 4.8: The reflectivity depth profile of three reflecting surfaces with reflectivity factor of 0.9, 0.75 and 0.6.

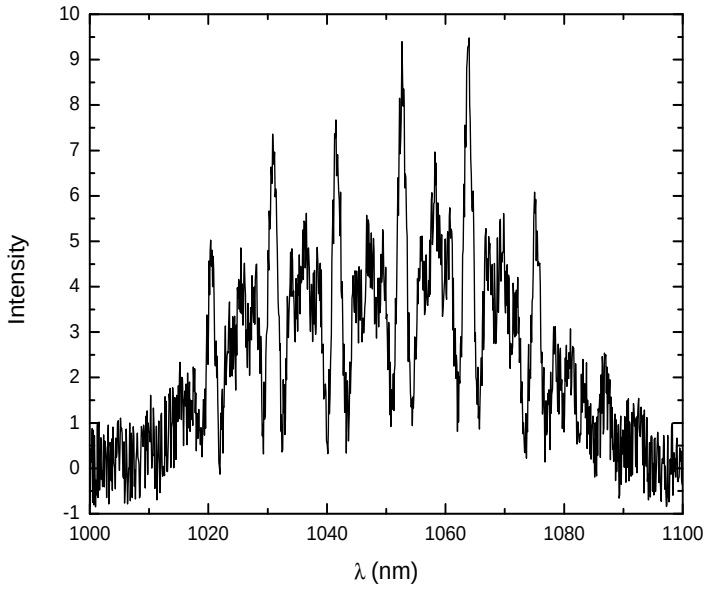

Figure 4.9: Simulated photo-detected signal of three reflecting surfaces contaminated by uniform white noise using values in Tables 4.1 and 4.2.

data spectrum where uniform white noise was added. After interpolation, the inverse FFT was applied to obtain the reflectivity depth profile. Fig.4.11 shows the reflectivity depth profile attained for three reflecting surfaces at OPDs: $z = 200$, 300 and 400 μm, in the presence of uniform white noise. The noise level in Fig.4.11 is clearly higher compared to the reflectivity depth profile result shown in Fig.4.7, but the added noise cannot prevent reconstruction of the depth profile and recognition of three reflecting surfaces from the contaminated white noise signal.

4.3.4 The Importance of Calibration and Re-sampling Methods

The impact of direct inverse Fourier transform of the spectral interference signal versus the effect of spectral calibration and re-sampling methods at a reflecting surface of 900 μm is shown in Fig.4.12. The black solid line is the result of the direct inverse Fourier transform of the spectral interference signal and the red solid line is the output of the Fourier transform after spectral calibration and interpolation are applied. The FWHM of the red peak, equivalent to the system axial resolution at OPD 900 μm, in Fig.4.12 is $\sim$ 16.54 μm while the FWHM of the black line is $\sim$ 79.42 μm. The red peak is approximately 4.8 times narrower, proving the fact that performing the Fourier transform of the collected interference signal

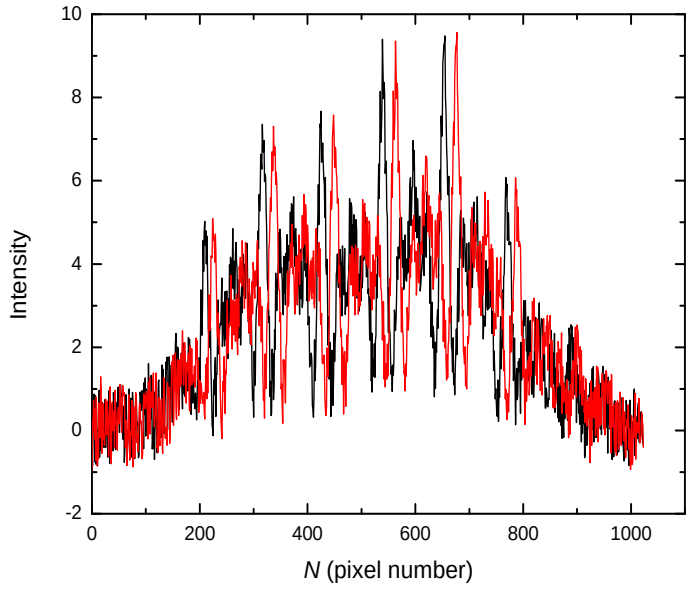

Figure 4.10: Non-interpolated (black line) and interpolated (red line) data spectrum as a function of pixel number in wavenumber space, and k-space, respectively (with presence of the uniform white noise).

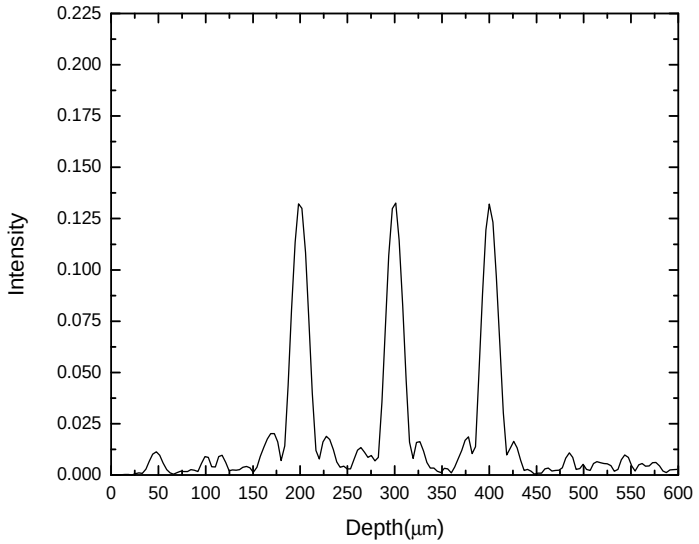

Figure 4.11: The reflectivity depth profile demonstrating three reflecting surfaces at $z = 200$, 300 and 400 μm with presence of the uniform white noise.

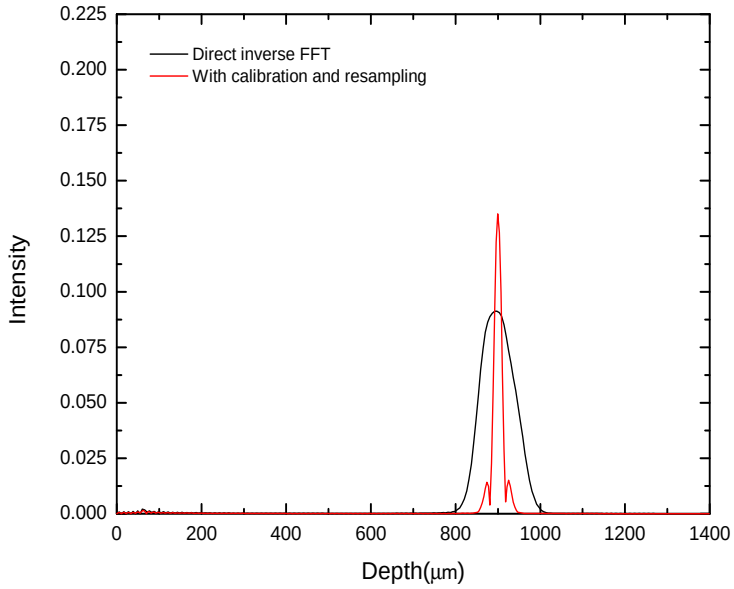

Figure 4.12: Reflectivity depth profile obtained from: inverse Fourier transformation of the spectral interference signal after spectral calibration and interpolation (red line), a direct inverse Fourier transform to the spectral interference signal without spectral calibration (black line). The parameter values mentioned in Table 4.1 were used, and the reflecting surface considered at 900 μm.

requires uniform spacing in wavenumber to avoid the deterioration of the SNR and also to prevent any degradation in the quality of the images.

4.3.5 SNR Assessment

Some numerical measurements were performed on the simulation results for simulated SD-OCT system SNR assessment. Uniform white noise with amplitude of 1 was generated and added to the simulated spectrometer data (Fig.4.9). Two approaches were studied to reduce the effect of the background noise and gain better SNR. One approach was to record several consecutive spectra and compute the average. The SNR was measured by $20\log(R_s/R_n)$, where R_s is the highest amplitude of the signal and R_n is the root mean square of the noise. The result up to 20 consecutive spectra record is shown in Fig.4.13.

An ideal number of sets should be considered, where the number of sets is big enough to remove noise and is small enough not to compromise the acquisition and the processing speed. A big collection of spectra would enhance the SNR, but the speed of SD-OCT would be potentially lost, since averaging over many signals will reduce the temporal response

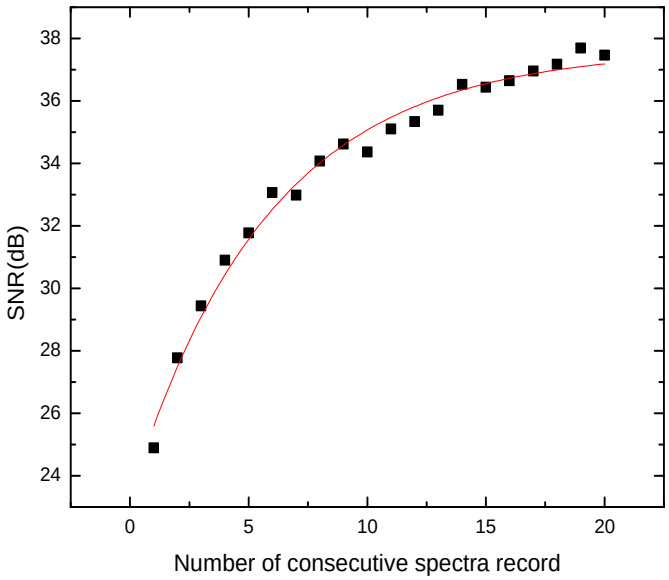

Figure 4.13: The SNR measurement result up to 20 consecutive spectra record.

of the system. Fig.4.13 shows that 15 recordings can be set as an optimized value for this method as the SNR improvement rate after this number is not significant.

To overcome the potential temporal limitation of spectra averaging another possible approach was to consider a moving window with a specific size and calculate the mean as the window is moved over the whole spectrum. Windows of different sizes, up to 20, were considered. The resulting SNR is shown in Fig.4.14 for the same amount of noise. The moving window averaging can be applied to single spectrum, but might compromise the resolution associated to the point spread function of the SD-OCT system, since the averaging will smooth out sharp signal variations.

The two techniques were compared. The results showed that the consecutive spectra averaging method provides a higher SNR than the moving window one. But the difference is not that relevant, so both methods can be potentially applied, favoring spectra averaging if good axial resolution is necessary, and possibly using moving window averaging if acquisition speed is paramount.

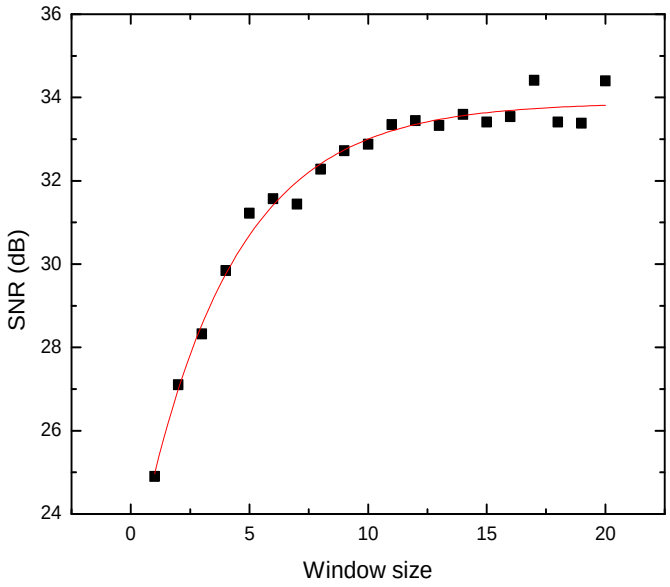

Figure 4.14: The SNR measurement result by considering different window size up to 20.

4.4 Summary

Methods for spectral calibration and data re-sampling of the SD-OCT signals were implemented numerically, paving the way for future SD-OCT signal processing under GPU architecture. It was shown that, as expected, $k-space$ linearization and spectral calibration procedure play a crucial role in achieving the highest signal resolution. Two different methods for SNR assessment were explored in order to find out optimized factors for reduction of background noise. It was demonstrated that consecutive spectra averaging yields higher SNR compared to moving window averaging, although the latter can be an option when temporal resolution is important. The developed spectral calibration and re-sampling methods yield promising signal quality. The presented algorithms are further developed under GPU architecture. The GPU-based data processing algorithms are described in more detail in Chapters 6 and 7 of this thesis.

Chapter 5

Common Path SD-OCT System

The developed spectrometer with configuration A discussed in Chapter 3 was integrated to a common path SD-OCT (CP-SD-OCT) system. The system was next calibrated by using the method proposed in Chapter 4. In this chapter, the CP-SD-OCT system is characterized based on some principal performance parameters such as maximum imaging depth, fringe visibility, sensitivity, sensitivity fall-off, axial resolution, and processing speed. The system characterization provides a good knowledge on system's performance and limitations. Such knowledge is crucial to achieve high quality images and to establish best performance operating parameters for imaging. Some optical measurements are conducted by employing the characterized system. The obtained results are presented and discussed.

5.1 Experimental Setup

A schematic diagram of the CP-SD-OCT system is shown in Fig.5.1. The optical components employed to implement this system is described in Table 3.2 with their acronyms used throughout this section. The system comprises of the broadband light source BOS, a common path interferometer, and the developed spectrometer with configuration A discussed in sections 3.2.4 and 3.3. The light source is a Multiwave Photonics' Broadband ASE source with a full width at half maximum (FWHM) of 50 nm, central wavelength at $\sim$1050 nm, and polarized light output power of 20 mW. The employed interferometer is a common path interferometer as the same physical path is shared between the reference and the sample arm. The deployment of such a shared optical path reduces group velocity dispersion and polarization mismatch between both arms of the interferometer and increases immunity to external interferences [111, 112].

The sensing head SH, installed on the motorized translation stage controller MTS, terminates the interferometer sample arm. The sensing head SH is interfaced through the

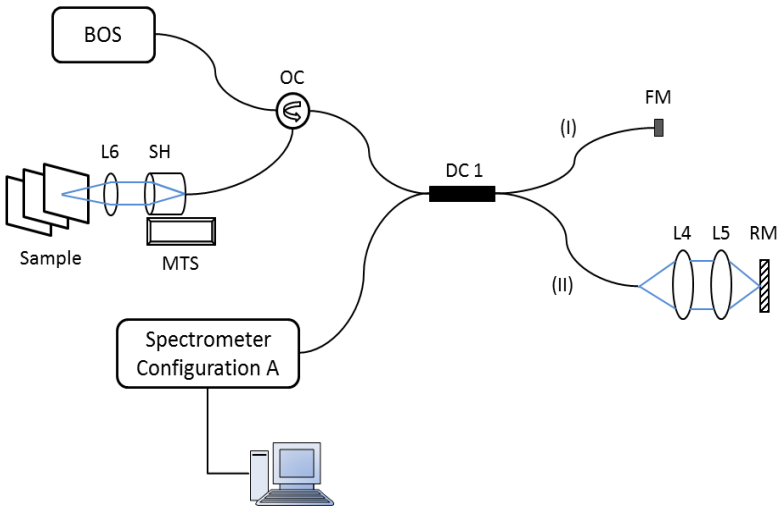

Figure 5.1: The schematic diagram of the CP-SD-OCT system. BOS: Broadband Optical Source, OC: Optical Circulator, SH: Sensing Head, MTS: Motorized Translation Stage, DC1: 50/50 Directional Coupler, FM: Fiber Mirror, RM: Reference Mirror, and L4-6: Achromatic Lenses.

highly specialized C-866 motion controller and the integrated drive electronics, controlled by a workstation computer through USB communication. A FC/PC fiber connector is utilized to connect the single mode fiber to the sensing head. The reference signal is obtained from the reflection at the distal end of the fiber, such that a fraction of light reflects back to the interferometer and the rest is transmitted and directed to the sample (sample signal) [111, 112]. The light reflected and scattered by the sample volume is collected back to the interferometer by the same sensing head. Back scattered and back reflected light pass through the 50/50 directional coupler DC1 and undertake interference after back reflecting from the interferometer arms indicated by (I) and (II) in Fig.5.1.

The interference signal is detected by the spectrometer configuration A explained in Chapter 3. The spectrum data collected by the line-scan camera LCCD is ultimately transferred to the workstation computer via an Ethernet card using the GigE Vision communication interface protocol.

5.2 System Performance Characterization

This section aims to provide the system characterization information, expressing the strengths and limits of the OCT imaging system. The following subsections summarize the characterization results of the implemented CP-SD-OCT system based on some major performance

parameters including: maximum imaging depth, fringe visibility, sensitivity, sensitivity fall-off, axial resolution, and processing speed.

5.2.1 Maximum Imaging Depth

The maximum imaging depth is normally measured by mounting a flat mirror in the sample arm of the interferometer. The mirror is placed on a single-axis translation stage with micrometer precision. The mirror is then translated by micrometer steps. The maximum imaging depth is found where the signal peak disappears, either by predominance of noise over spectral fringes, or by fringes being washed out by the aliasing problem discussed in section 2.4. The maximum imaging depth was measured by translating the sensing head until the spectral fringes vanished, while the mirror used as a sample was stationary. The maximum imaging depth was measured as ~ 3.06 mm.

The maximum imaging depth can be further improved by using a line-scan camera with higher number of pixels (greater than 2048 pixels). However, the typical imaging range of an OCT imaging system is normally limited to few millimeters (2-3 mm) in biological tissue because of the scattering and absorption properties of the testing sample, attenuating light propagation along the sample.

5.2.2 Fringe Visibility

The fringe visibility, or interferometric visibility, expresses the achieved fringe contrast of interference signal. The visibility is maximized when the intensity of the signals returned from sample and reference arms are alike. The fringe visibility function (V) is defined in terms of the maximum and the minimum intensity of the spectral fringes as follows, comparing the coherence (interference) signal amplitude with the incoherent signal superposition. It is expressed as [113]:

$$V = \frac{I_{max} - I_{min}}{I_{max} + I_{min}} \tag{5.1}$$

where I_{max} and I_{min} denote the maximum and the minimum intensity of the fringes, respectively. The fringe visibility varies between 0 and 1. The fringe visibility was measured by placing the flat mirror as a sample. The incident power on the sample was ~ 1.4 mW. A fringe visibility of 0.93 was obtained at the optical path difference close to zero (OPD = $\sim 100\ \mu m$). The visibility decays with increased depth, and it drops to approximately 0.39 at the maximum imaging depth. The reported OPD was measured by constructing the

reflectivity depth profile using the calibration method discussed in Chapter 4.

5.2.3 Sensitivity

The system sensitivity is the ability of an imaging system to detect smallest amount of back reflected light from the testing sample. In OCT context, sensitivity and signal to noise ratio (SNR) are often used interchangeably. The system sensitivity is defined as the ratio of maximum signal over noise floor, and it is expressed in decibel unit. The maximum signal is measured by placing a perfect reflector in the sample arm of the interferometer without saturating the detector or exceeding the digitization range. The sensitivity or SNR is given by [40]:

$$SNR = 20log\left(\frac{FFT^{-1}\left\{I_{peak}(z)\right\}}{\sigma\left(FFT^{-1}\left\{I_{noise}(z)\right\}\right)}\right) \tag{5.2}$$

where the numerator, $FFT^{-1}\left\{I_{peak}(z)\right\}$, is the highest value of the signal after taking the inverse Fourier transform, and the denominator, $\sigma\left(FFT^{-1}\left\{I_{noise}(z)\right\}\right)$, is the standard deviation of the noise floor, away from the peak position, and after taking the inverse Fourier transform.

The same flat mirror was placed as a sample at depth 0.1 mm. The incident power on the sample was measured as $\sim$1.4 mW. The averaged standard deviation of 512 measurements (A-scans) of noise with the sample removed was computed. Employing Eq.5.2, the system sensitivity was measured as $\sim$ 98.21 dB. Higher sensitivity can be even achieved by reducing fiber coupling loss. There is a power loss when the light is launched back into the fiber. There is also some other power losses in FC/APC fiber mating sleeves. Decrease of such losses would result in the increase of the overall sensitivity of the CP-SD-OCT system. In addition, as the electronic noise in the CP-SD-OCT system is dominant, reduction of such noise would significantly increase the overall sensitivity.

5.2.4 Sensitivity Fall-off

The sensitivity fall-off was measured by using the flat mirror as a sample and computing the SNR expressed by Eq.5.2 at 15 positions along the imaging range. The exposure time of the line-scan camera was 27.8 μs during the acquisition of A-scans. The A-scans were processed by employing the spectral calibration and the 1D linear interpolation methods discussed in Chapter 4. Fig.5.2 demonstrates the measured SNR in dB scale as a function of

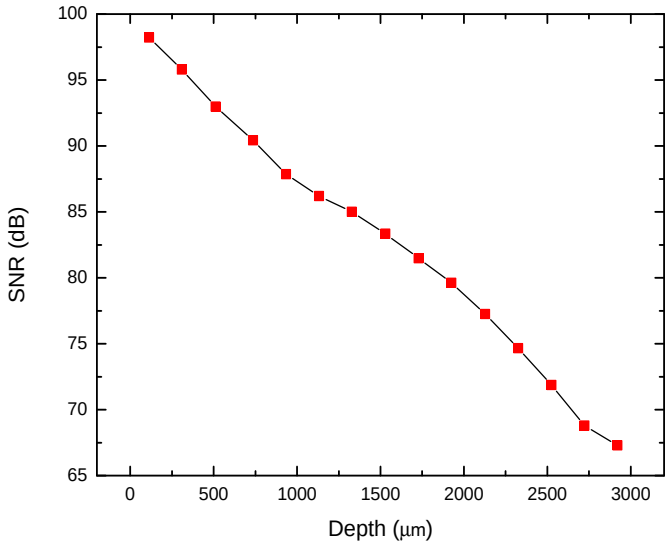

Figure 5.2: Sensitivity fall-off measurement of the CP-SD-OCT system as a function of depth.

depth. The system sensitivity fall-off, at maximum depth, was measured as 30.93 dB. Such high sensitivity fall-off is attributed to the spot size of the focused beam on the detector. The spot size of on axis beams is less than the pixel size; however, by the increase of beam angle, the spot size increases to the size of approximately more than one and half pixel size at the extreme ends of the pixel array. Reducing the spot size to less than the pixel size would significantly decrease the sensitivity drop over the imaging range.

5.2.5 Axial Resolution

The system axial resolution over a depth range of 3 mm is demonstrated in Fig.5.3. The same flat mirror was deployed as a sample. The axial resolution was obtained by measuring the FWHM of the axial reflectivity profile of the air/mirror interface, as a function of depth, at 15 positions along the imaging range. The averaged axial resolution was measured as $\sim 20\ \mu$m over the depth range of 3 mm, using the developed wavelength calibration method discussed in Chapter 4. As it is shown in Fig.5.3, there is a slight decrease (less than 1 μm) in axial resolution as the imaging depth increases. Aliasing started to affect the spectral fringes after an imaging depth of ~ 3.1 mm.

There is $\sim 10\ \mu$m difference between the theoretical and the experimental axial resolution. This can be attributed to the spot size of the focused beam on the camera and the

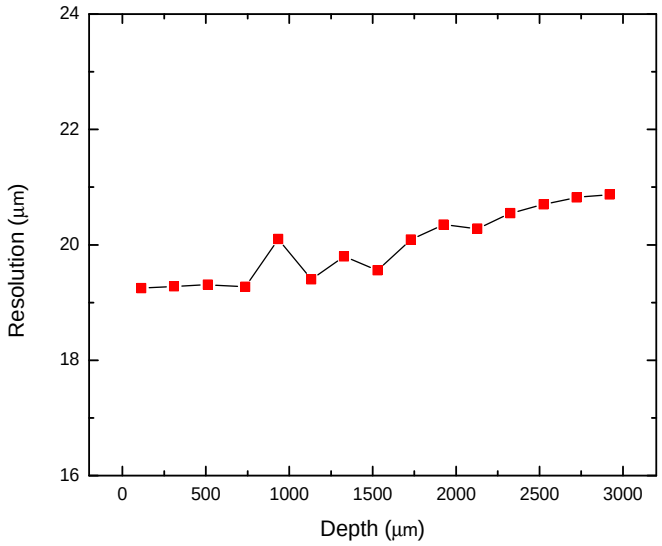

Figure 5.3: System axial resolution as a function of depth, demonstrated over a depth range of $\sim$ 3 mm.

responsivity of the Dalsa camera within the wavelength region of 1000-1100 nm. The spot size of the beam in Configuration A covers approximately one and half pixels, resulting in reduction of the axial resolution. A comparison between the optical source spectrum and the dramatic decay of the camera's responsivity within the same region of 1000-1100 nm, as demonstrated in Fig.3.1, indicates the reshaping of the detected spectra by the camera sensitivity, resulting in further degradation of the measured axial resolution.

5.2.6 Processing Speed

The imaging system has an A-scan processing speed of $\sim$ 21 kHz while the line-scan camera is operating in high sensitivity mode with the maximum line rate of 36 kHz and the exposure time of 27.8 μs. Each A-scan consists of 2048 samples. The obtained processing speed includes all processing time of the implemented OCT processing steps as well as the display time. The processing steps to construct the axial reflectivity profile of the testing sample consist of linear interpolation, background subtraction, spectral shaping (Hamming window), dispersion compensation, zero-padding, inverse Fourier transform, and modulus. These steps were implemented under the graphics processing unit (GPU) architecture to achieve a camera limited readout speed rate. These processing steps are explained in detail in Chapter 7.

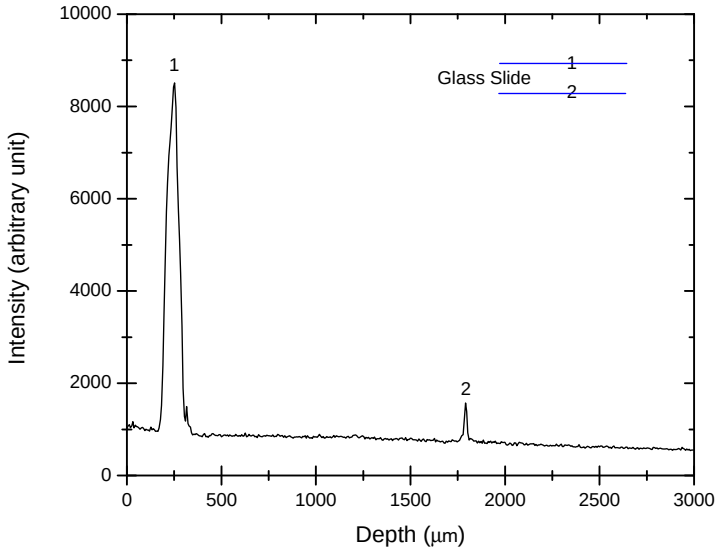

Figure 5.4: The reflectivity depth profile measured from the glass slide sample. The optical length between the two surfaces (peaks) was measured as $\sim$ 1537 μm, corresponding to a physical thickness of $\sim$1 mm (considering the refractive index of the glass microscope slide as 1.5251).

The given processing speed is now limited to the maximum readout speed of the used line-scan camera. The processing speed can be increased by replacing the existing line-scan camera with a higher line rate camera. The developed processing and visualization algorithms allow the reconstruction of A-scans at the maximum readout speed rate of the line-scan camera. Currently, the DALSA camera provides $\sim$ 21 k lines/sec (each line consists of 2048 pixels) while working at the maximum line rate of 36 kHz with the exposure time of 27.8 μs.

5.3 Measurements

After acquiring the knowledge on system's performance and limitations, three different samples were imaged to validate the imaging system. The presented results are all 1D measurements, enabling optical thickness measurements of multilayered micrometric structures with micron scale accuracy.

A plain glass microscope slide with the thickness of approximately 1 mm was first imaged. The resulting depth profile is shown in Fig.5.4. The peaks labeled as 1 and 2 correspond to the front and the back surface of the glass slide, respectively, and the optical

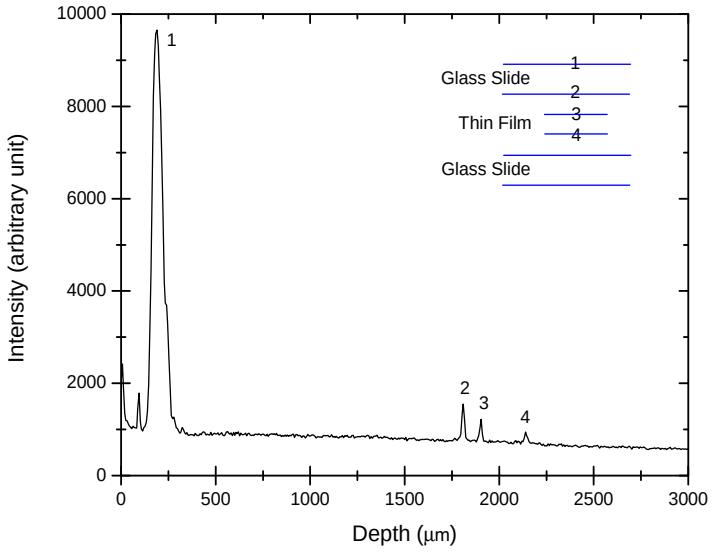

Figure 5.5: The reflectivity depth profile measured from a very thin film sandwiched between two plain glass microscope slides. The optical length between peak 1 and 2 is $\sim 1620\ \mu m$, and the optical length between peak 3 and 4 is $\sim 234\ \mu m$. There is an air gap between the first glass slide and the thin film, measured as $\sim 95\ \mu m$ (the optical length between peak 2 and 3).

length between them is $\sim 1537\ \mu m$. Considering the refractive index of the glass microscope slide as ~ 1.5251, the obtained optical thickness is equivalent to a physical thickness of $\sim 1.00\ mm$. This is in good agreement with the actual physical thickness of the imaged glass slide measured by a digital caliper with 1 μm precision.

Fig.5.4 demonstrates a drop-off in the peak amplitudes of the depth profile obtained from the interrogated glass slide. This is attributed to the depth dependent fall-off in the sensitivity of the imaging system, limiting the imaging range of the CP-SD-OCT system. The peak amplitudes are also proportional to the reflection coefficients of the front and back surface of the testing glass slide.

The next sample was a fabricated object, simulating a multilayer structure. The fabricated sample consists of a very thin film sandwiched between two glass microscope slides. Each glass slide has the physical thickness of 1 mm, and the physical thickness of the thin film is within the range of $100\ \mu m - 300\ \mu m$.

Fig.5.5 illustrates the resulting reflectivity depth profile, indicating four reflections obtained from the front and the back surface of the first glass slide (the peaks labeled as 1 and 2), and the front and the back surface of the thin interior film (the peaks labeled as 3 and

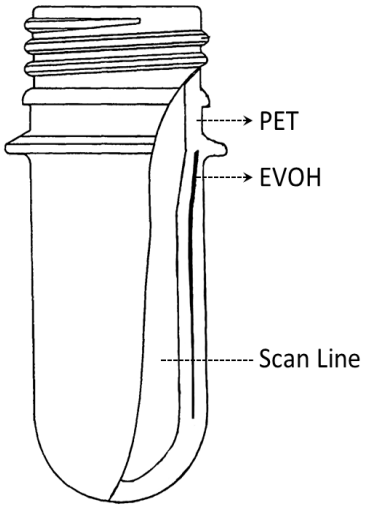

Figure 5.6: A schematic of the bottle preform.

4). The distance between peak 1 and 2 is $\sim 1620\ \mu m$, demonstrating the optical length of the first glass slide. This optical length corresponds to $\sim 1.06\ mm$ physical thickness of the glass slide. The distance between peak 3 and 4 is $\sim 234\ \mu m$, showing the optical length of the thin film; thus, the physical thickness is evaluated as $\sim 154\ \mu m$, considering the refractive index of the thin film as 1.52. There is an air gap between the first glass microscope slide and the inner thin film. This air gap is determined by measuring the optical distance between peaks labeled as 2 and 3 in Fig.5.5. Such an air gap is measured as $95\ \mu m$.

The first peak with no label in the beginning of the depth profile is the coherence noise and is caused by the low frequency modulation of the light source. Apart from the cross-correlation term discussed in section 2.1.2, containing the depth information, there also exist many reflections within the imaging system components that contribute to the total signal. These low frequency signals are referred to as coherence noise.

The next imaged sample was a bottle preform used for beverage packaging. The bottle preform is made of polyethylene terephthalate (PET) material with a very thin film of ethylene vinyl alcohol (EVOH) or nylon embedded in the middle. A schematic of the bottle preform is demonstrated in Fig.5.6. The knowledge of the intermediate film thickness is paramount to determine the quality of produced preforms at the production line before blow molding process begins. As depicted in Fig.5.6, the film thickness is thicker near the bottle neck, and it decreases as the height increases. The typical film thickness is normally between $10 - 250\ \mu m$.

The bottle preform was imaged, and an A-scan was acquired from the scanning area

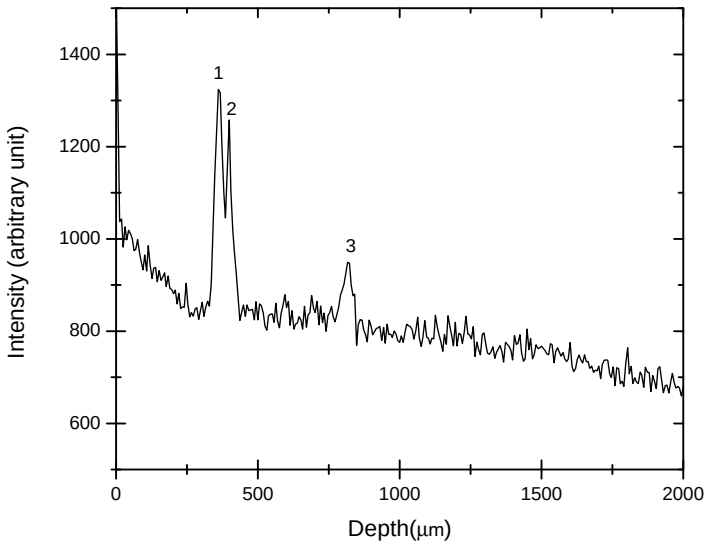

Figure 5.7: The reflectivity depth profile of the imaged bottle preform obtained from three reflecting surfaces. These reflecting surfaces correspond to PET/EVOH, EVOH/PET and PET/air interfaces, labeled as peak 1, 2 and 3, respectively. The distance between peaks labeled as 1 and 2 determines the optical thickness of the EVOH laminate film ($\sim 38\ \mu m$). The peaks labeled as 2 and 3 determine the optical distance between EVOH/PET and PET/air interfaces ($\sim 417.64\ \mu m$).

shown in Fig.5.6. The depth profile of three reflecting surfaces of the imaged bottle preform is demonstrated in Fig.5.7. These surfaces correspond to EVOH laminate film, the peaks labeled as 1 and 2, and the PET/air interface, the peak labeled as 3. The optical distance between peak 1 and 2 was measured as $\sim 38\ \mu m$. Such a measurement determined the physical thickness of the EVOH laminate film in close proximity to the head position of the preform as $\sim 25\ \mu m$, considering the refractive index of EVOH as 1.525 [114]. The optical distance between EVOH/PET and PET/air interfaces were measured as $\sim 417.64\ \mu m$, corresponding to physical thickness of $\sim 265\ \mu m$, considering the refractive index of PET as 1.575 [114].

5.4 Summary

The designed and implemented spectrometer with configuration A presented in Chapter 3 was integrated to the CP-SD-OCT system. After performing the calibration method developed in Chapter 4, the CP-SD-OCT system was characterized based on some principal

performance characterization parameters. This chapter presented the results of the imaging system assessment based on fringe visibility, sensitivity, sensitivity fall-off, axial resolution, imaging range, and processing speed. Such a characterization assessment is also summarized in Appendix A for future reference.

The awareness of the strength and limitation of the imaging system is of paramount importance. Such gained knowledge of various system performance parameters enabled to better perform the imaging of samples. The obtained system information also eases the comparison of various OCT imaging systems. Three different samples were imaged to measure the optical and physical thickness of multilayer structures. The imaged samples included a plain glass microscope slide, a fabricated multilayer structure, and a bottle preform. All performed measurements were 1D, aiming to reveal the thickness of micro multilayer structures with micron scale accuracy. The obtained imaging results proved a significant improvement in overall performance of the existing CP-SD-OCT system, thus enabling to conduct 1D OCT imaging in order to measure the thickness of micro multilayer structures.

Chapter 6

GPU-Accelerated SS-OCT Data Processing and Visualization for Micro-surgeries

In this chapter, the optimization techniques to achieve a real-time video rate swept source optical coherence tomography (SS-OCT) system are presented. All technological challenges are discussed in detail, and the solutions for an efficient processing and visualization are given. Live video rate volumetric 4D OCT signal processing and visualization is realized. So far, high speed GPU-based OCT data processing approaches have been proposed for processing and display of small OCT volumes because of GPU memory and resource limitations. Conversely, this chapter demonstrates the feasibility of real-time processing and visualization of large OCT volumes with high efficiency (81%) by using only a single commercial-grade GPU. The developed algorithm not only has high efficiency but also has speed advantages over conventional CPU-based OCT data processing approaches. This study is a very important step toward the development of an intraoperative surgical OCT system to be deployed at New England Eye Center. Such a developed system is employed as a surgical guidance tool to provide intraoperative feedbacks to surgeons, assisting them to better perform micro-surgeries.

6.1 Introduction

OCT is a continuously evolving optical imaging modality which provides cross-sectional and 3D information of the examined samples at micrometer-scale resolution, noninvasively. As discussed in section 1.1, contact free, non-destructive, non-invasive and cost-effective

features of OCT, compared to other imaging modalities, made it suitable for biomedical imaging and industrial applications [115–120]. Such medical and industrial applications are comprehensively reviewed in section 1.1.

OCT has dramatically improved in terms of resolution, sensitivity and speed since its emergence in early 1990s [6, 121–123]. Early implementation of OCT systems, known as TD-OCT system, acquired and processed B-scan images in less than 3 s for in vivo retinal imaging [124]. Although the speed of TD-OCT has increased to couple of B-scans per second over the last two decades [125], the mechanical movement of the scanning mirrors is a barrier to achieve higher frame rates. Later by the advent of FD-OCT, sensitivity and speed were increased. In this method the reference mirror is stationary, and the reflectivity profile is obtained by applying a fast Fourier transform to the spectral fringe signal [49]. It has been demonstrated that FD-OCT has superior sensitivity advantage, typically 20-30 dB over conventional TD-OCT [13, 47]. In addition to sensitivity, the speed has been tremendously improved to A-scan rate of beyond 10 MHz since FD-OCT was introduced [122]. Advances in the development of optical sources and significant increase in acquisition speed have brought about the realization of such ultrahigh-speed and -resolution OCT systems.

Despite the aforementioned advances in resolution, sensitivity and acquisition speed, real-time data processing and visualization was still lacking during mid-2000s. Although ultrahigh-speed OCT systems were able to acquire volumetric OCT data in real-time, the data processing, construction of 2D images and rendering 3D images were performed in post-processing stage. Several approaches have been proposed to ameliorate OCT data processing and visualization. Field-Programmable Gate Array (FPGA) [126, 127], multi-core CPU parallel processing [61, 128], digital signal processor (DSP) [129] and graphics processing units (GPU) [109, 130] have been employed to accelerate data processing and visualization of FD-OCT images. Among the proposed approaches, GPU-based OCT data processing methods have been increasingly gained popularity because of the reasons explained in the next paragraph.

GPU is highly optimized for massive parallel processing. High processing speed and high bandwidth memory (HBM) of GPU make it very attractive for FD-OCT data processing and visualization. Central processing unit (CPU) hardly handles the heavy computational load of FD-OCT data to process and visualize 3D volumetric OCT data in real-time. Therefore, nowadays the intensive OCT data computations have shifted from CPU to co-processing on the CPU and GPU. GPU-based data processing approaches have three distinct advantages:

1. It offers high performance and speed.

2. It requires simpler programming knowledge on the host computer.

Source	Data Set Size (A-scans×B-scans×Samples)	Vol. Size (MB)	Processor(s)	Vol. Rate (Volumes/s)	Speed (GVoxels/s)
Zhang et al. [149]	125×100×512	12.8	Single GPU	10	0.06
Choi et al. [143]	128×128×256	8.4	<25 FPGAs +Single GPU	41	0.17
Jian et al. [144]	256×200×1024	104	Single GPU	23	1.2
Wieser et al. [145]	320×320×400	82	Dual GPU	26	1.07
This Study	587×2500×960	2800	Single GPU	1.29	1.82
This Study	587×2500×960	2800	Dual GPU	2.05	2.89

Table 6.1: The studies on the development of a real-time video rate volumetric 4D OCT imaging system.

3. High speed computations, 2D visualization and 3D rendering of OCT data can be implemented at a lower cost.

Such distinguished features and advances in GPU computing lead many research groups to re-implement the conventional OCT signal processing steps, previously performed at much lower speed, on GPU(s) to achieve real-time processing and display [108, 109, 131, 132]. In these studies high computational horsepower of GPU was exploited to significantly shorten data processing time and accomplish a real-time video rate OCT imaging system. In addition to this re-implementation, some previously reported time consuming reconstruction methods such as non-uniform discrete fast Fourier transform (NDFFT) and non-uniform fast Fourier transform (NUFFT) [133, 134] were demonstrated by using GPU computation to obtain the reflectivity profile with substantially improved performance [135]. A GPU-based scheme was proposed for dispersion encoded full-range OCT to remove complex-conjugate artifact and display full-range OCT in real-time [136]. Apart from structural OCT imaging, GPU has been also employed for functional imaging such as polarization sensitive OCT (PS-OCT) [137], speckle variance OCT [138, 139] and Doppler processing [140–142].

Volumetric four-dimensional OCT (4D OCT) imaging with video rate real-time visualization can be achieved by the combination of ultrahigh-speed OCT and fast GPU computation [142–148]. So far, GPU-based live video rate 4D OCT systems have been demonstrated for processing and 2D/3D visualization of small volumes due to hardware limitation of GPU. Table 6.1 summarizes the published studies on the development of real-time video rate volumetric 4D OCT imaging systems. The processing speed is measured as the number

of processed voxels in a time unit and is expressed in terms of "GVoxels/s" in Table 6.1, facilitating the comparison of various systems [150].

Zhang et al. showed live 4D SD-OCT for the volume size of 125 A-scans × 100 B-scans × 512 samples/A-scan with the speed rate of 0.06 GVoxels/s [149]. Later, Choi et al. presented a real-time 4D OCT system capable of processing a volume size of 128 A-scans × 128 B-scans × 256 samples/A-scan by using numerous FPGAs (more than 25) to carry out signal processing and a GPU for volume rendering [143]. A speed rate of 0.17 GVoxels/s was achieved for such a volume size. Jian et al. attained a real-time video rate processing and visualization of the volume size of 256 A-scans × 200 B-scans × 1024 samples/A-scan by using a single GPU [144]. Their speed rate was 1.2 GVoxels/s. Wieser et al. accomplished a fast processing and rendering of the volumes size of 320 A-scans × 320 B-scans × 400 samples/A-scan with the speed rate of 1.07 GVoxels/s by employing a dual-GPU card [145].

In contrast to above reviewed studies, this chapter proposes a GPU-based optimized algorithm to achieve processing and visualization of large volumes by using only a single GPU. The captured volume size was 587 A-scans × 2500 B-scans × 960 samples/A-scan, which was processed at sustained speed rate of 1.82 GVoxels/s. Such a speed rate goes to 2.89 GVoxels/s if two GPUs are employed. In this chapter, the optimization techniques for an efficient large volume processing and visualization in real-time are discussed in detail. Moreover, some potential applications of real-time video rate volumetric 4D OCT are given.

6.2 Experimental Setup

A swept source OCT (SS-OCT) system consisting of a microelectromechanical system (MEMS)-tunable vertical-cavity surface emitting laser (VCSEL) light source was used for imaging and evaluation of the proposed signal processing scheme. The VCSEL optical source has the advantage of having very long coherence length, imaging depth range of ~ 5 cm, adjustable spectral sweep range and adjustable sweeping rate (50 - 580 kHz) [151].

The SS-OCT imaging system was developed by the RLE group members and was reported in their previous published studies [152, 153]. The VCSEL optical source operated at 400 kHz sweep rate centered at ~ 1060 nm with wavelength sweep range of ~ 84 nm and axial resolution of ~ 9 μm in tissue. The imaging range was 1.9 mm in tissue and the measured sensitivity was 97.8 dB, using a flat mirror as a sample. An AlarzarTech digitizer card (ATS9360, 12 bit 1.8 GS/s) was used to capture the OCT signal. The digitizer card was externally clocked by using a Mach-Zehnder interferometer to sample the interference signal equally spaced in wavenumber. The digitizer card was clocked with the maximum

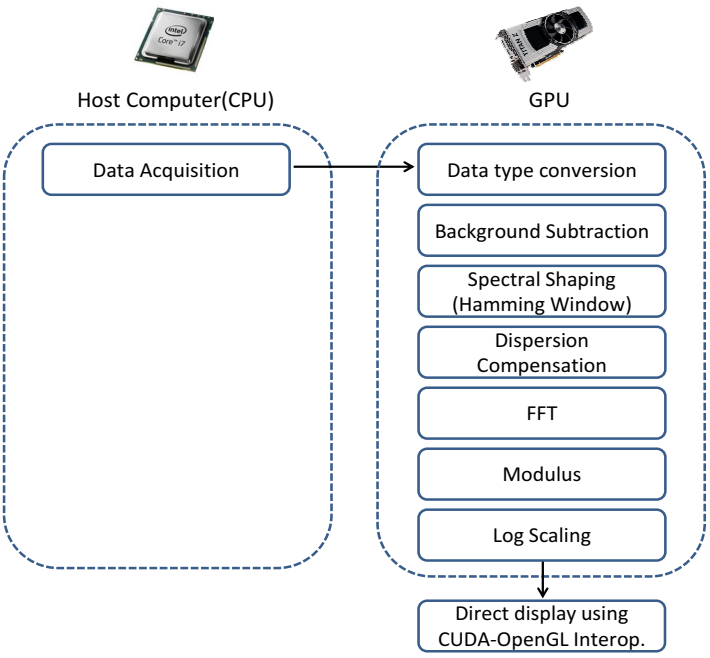

Figure 6.1: A schematic of the GPU processing steps.

clock frequency at 1.0 GHz. A-scan trigger fluctuations were corrected by using a fiber Bragg grating (FBG, $\lambda_0 = 1087$ nm) in one of the balanced detection arms.

6.3 Signal Processing Algorithm and Optimization of GPU Computation

NVIDIA's parallel computing platform and programming model, compute unified device architecture (CUDA) version 6.5 was employed to program and harness the power of the GPU [154]. CUDA-enabled GPU GeForce GTX TITAN Z was exploited. The graphics card consists of twin TITAN Z GPUs which both are connected by a peer-to-peer bus to enhance data communication speed between two GPUs. Each GPU has 6 GB memory and 2880 processing cores. The application was built and compiled in Microsoft Visual Studio 2010. The GPU card was installed in a workstation computer with Intel Core i7-4930K processor running windows 7 64-bit version. The motherboard supports PCI-Express 3.0, allowing maximum bandwidth for data transfer between system and GPU memory.

A schematic of the processing steps performed on the GPU is shown in Fig.6.1. After capturing and digitizing the interference OCT signal, the data was stored in a host computer. In CUDA context, CPU or its memory is referred to as host, and GPU or its memory is

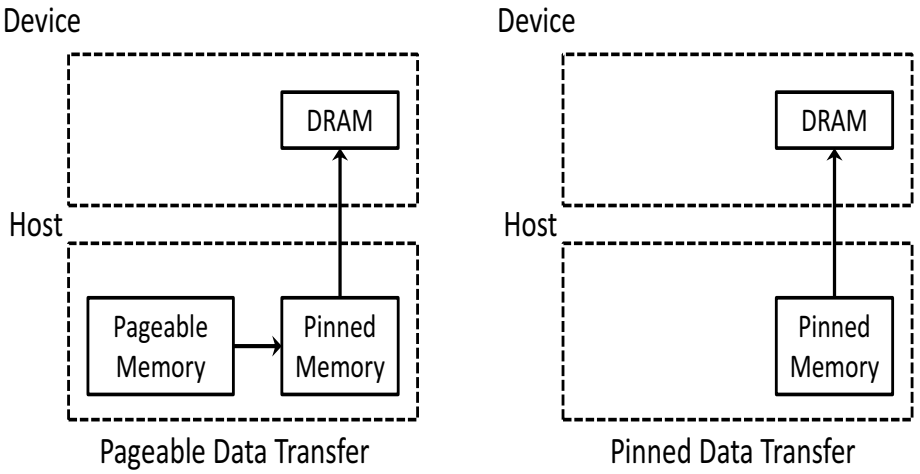

Figure 6.2: Data transfer strategies between host and device.

referred to as device. One of the main bottlenecks previously reported to achieve real-time volumetric OCT data processing and visualization was the data transfer between GPU and host computer. Significant time ($\sim$ 85% of the total processing time) was spent for transferring data to and from GPU memory [109].

The amount of data transfer between host and device was minimized to reduce the data transfer time. As the digitized signal was 16-bit integer, the captured data was first transferred to device memory and then converted to a single precision 32-bit float to minimize data transfers. Another employed optimization technique was to define host memory as pinned memory. The captured data is normally saved in a pageable memory by default, so the data is first copied to pinned memory and subsequently is transferred to device as illustrated in Fig.6.2 [155]. The extra copy from pageable memory to pinned memory was avoided by directly defining pinned memory on host computer. Such a technique allowed achieving maximum data bandwidth for data transfer. The processing speed was improved by a factor of $\sim$ 55% by using pinned memory.

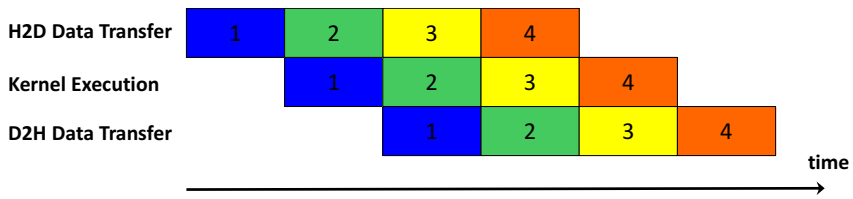

Figure 6.3: Asynchronous data transfers allowing the kernel executions to be overlapped with the data transfers.

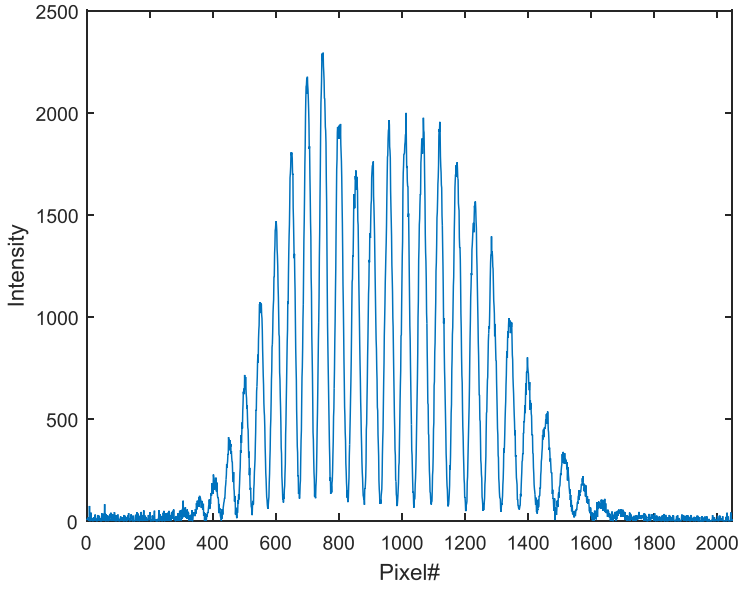

Figure 6.4: A typical captured spectrum.

Another exploited optimized approach was to copy data asynchronously so that data transfers could be overlapped with kernel executions [156]. Fig.6.3 demonstrates asynchronous data transfers allowing the kernel executions to be overlapped with the data transfers [156]. Two streams, sequence of operations executed on GPU, were defined such that copy operations and data processing were executed simultaneously. Using PCIe generation 3 together with the aforementioned optimization techniques, the digitized OCT data was efficiently transferred to GPU memory at the rate of ~ 9.95 GB/s.

A typical captured spectrum is shown in Fig.6.4. The ensemble average of the spectra prerecorded as background signal was computed, and then subtracted from each A-scan within acquired B-scan images [157]. The result of such operation is demonstrated in Fig.6.5. The coherent artifacts or side-lobes were eliminated in the next step. This side-lobes effect is introduced by the non-Gaussian spectral shape of the optical source and the limited width of the recorded spectrum [158]. Such an effect causes false targets and artifacts, degrading the quality of resultant images. The side-lobes effect was minimized by performing a direct spectral reshaping method exploiting a Hamming window. Fig.6.6 shows the obtained result after applying the Hamming window.

The dispersion mismatch between the reference and the sample arms was compensated by a numerical method introduced in Ref.[78]. The fast Fourier transform (FFT) of each A-scan was computed by using a dedicated NVIDIA's CUDA FFT library (CUFFT) [159]. The magnitude of the FFT was obtained by taking modulus of each complex pixel value and

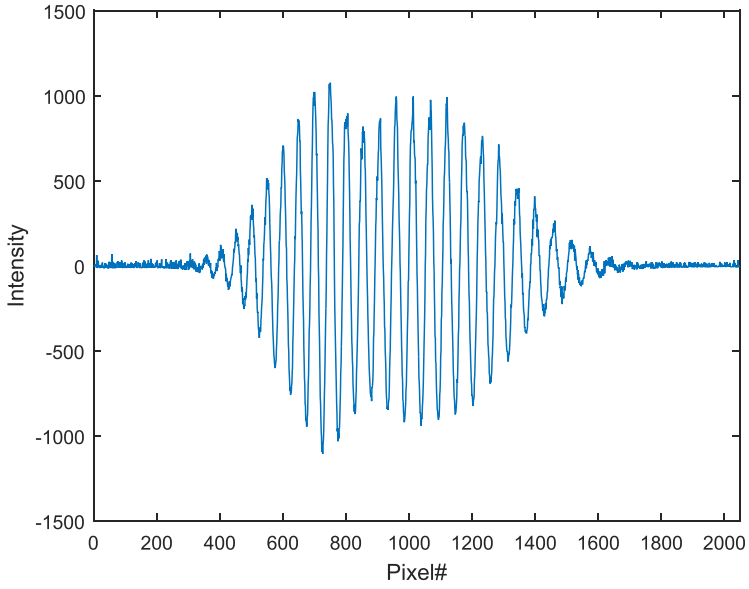

Figure 6.5: The ensemble average result of the prerecorded spectra.

then the intensity values were expressed in logarithmic scale.

Instead of copying the data back to host computer, CUDA/OpenGL interoperability feature enabling interoperation between CUDA and OpenGL API functions was utilized to

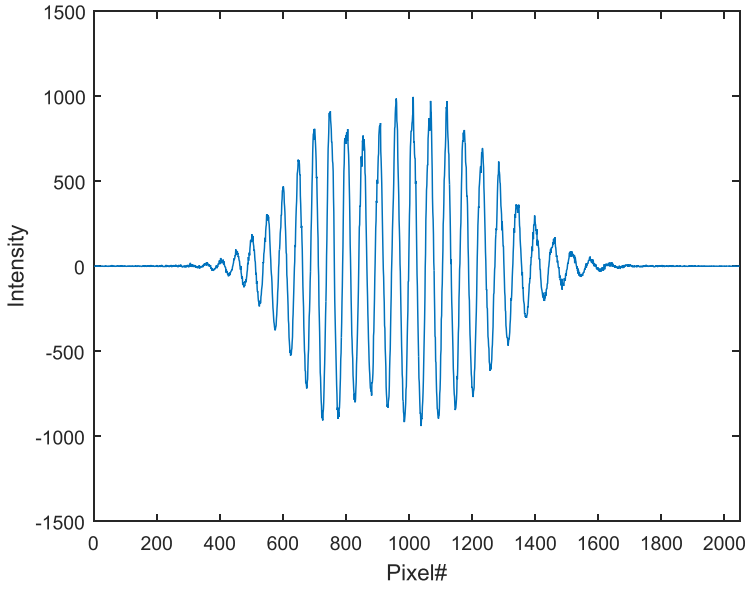

Figure 6.6: Spectral reshaping by using a Hamming window to smooth the resultant signal and minimize the side-lobes effect.

Data set size	2.8 GB	8.1 GB
Number of frames	2500	3276
Frame size (A-scans×Samples)	587×960	1500×848
(A) Single GPU		
Processing time (with D2H data transfer)	0.981 s ∼1.43 GVoxels/s	3.53 s ∼1.18 GVoxels/s
Processing time (without D2H data transfer)	0.774 s ∼1.82 GVoxels/s	3.32 s ∼1.25 GVoxels/s
(B) Two GPUs		
Processing time (with D2H data transfer)	0.542 s ∼2.59 GVoxels/s	1.95 s ∼2.13 GVoxels/s
Processing time (without D2H data transfer)	0.487 s ∼2.89 GVoxels/s	1.72 s ∼2.42 GVoxels/s

Table 6.2: Offline processing time of two OCT data sets (2.8 GB and 8.1 GB), expressed with and without considering device to host (D2H) data transfers by using: (A) a single GPU, and (B) two GPUs.

directly display the processed information. Such a method increases the display rate by eliminating the time spent to transfer the data back to host computer. OpenGL utility toolkit (GLUT) was ultimately used to implement and program a user interface [160].

6.4 Results and Discussion

The accuracy of the processing steps demonstrated in Fig.6.1 was first validated offline by using two acquired ophthalmic and endoscopic data sets as input. The images processed by GPU were compared with the processed images by MATLAB. Fig.6.7 illustrates GPU- and MATLAB-processed images obtained from a human retina. The comparison of the two extracted A-scans from the same transversal position shown in Fig.6.7.c confirms the similarity between these two processed images. The attained GPU A-scan was shifted by 0.45 unit to ease the comparison. The implemented MATLAB code to verify the GPU results is available in Appendix D.2.

The time execution is also measured, and the results are benchmarked in Table 6.2. The processing speed is expressed in terms of "GVoxels/s" to facilitate comparisons. D2H and H2D signify the data transfer from device to host and host to device, respectively.

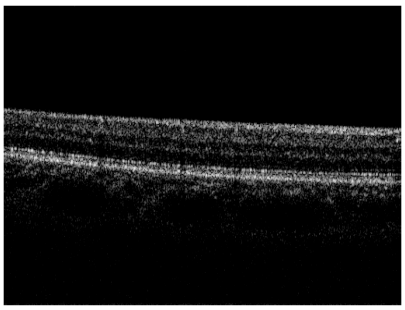

(a) GPU-processed image

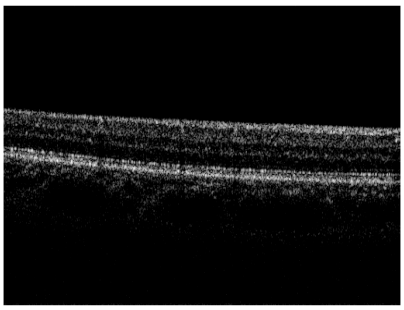

(b) MATLAB-processed image

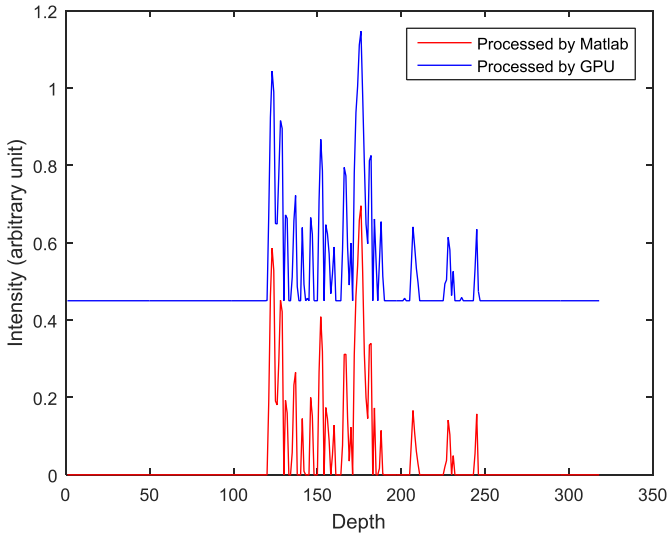

(c) Extracted A-scans

Figure 6.7: (a) GPU- and (b) MATLAB-processed images obtained from a human retina. (c) Comparison of the two extracted A-scans from the same transveral position confirming the similarity between GPU- and MATLAB-processed images. The attained GPU A-scan was shifted by 0.45 unit to ease the comparison.

The processing time reduced when device to host data transfer was eliminated. The endoscopic data set (8.1 GB) and the ophthalmic data set (2.8 GB) were processed in ∼3.32 s and ∼0.77 s respectively without considering device to host data transfer. If device to host data transfer time was added, the processing time for the endoscopic and ophthalmic data sets would increase to ∼3.53 s and ∼0.98 s, respectively.

As the GPU card comprises of two GPUs, multi-GPU programming technique was employed to examine how much the processing time would decrease in relation to the number of added GPUs. The obtained results are benchmarked in Table 6.2.B. Comparing the temporal performance results of two GPUs and a single GPU, the results demonstrated that

the processing time reduction factor is not exactly proportional to the number of GPUs used only for processing. Although employing several GPUs for compute-intensive data processing is suitable as the processing time considerably decreases, it should be taken into account that the reduction factor is less than number of GPUs. The comparison of the results shown in Table 6.2.A and 6.2.B also revealed that the corresponding reduction processing time factor of endoscopic data set is greater than the ophthalmic data set because of the fact that the endoscopic data set size is bigger. This proved that higher temporal performance can be achieved when GPU processing pipeline is kept filled.

The high speed GPU processing code was integrated into the existing complex C++ application implemented for ophthalmic and endoscopic imaging at RLE group. All GPU processing and visualization routines were implemented inside an isolated DLL file such that GPU and the C++ code can cooperate without having any conflict. This approach enabled GPU real-time data processing and visualization while the C++ application was operating. In this study, the developed GPU-accelerated application utilizes only a single consumer grade GPU to achieve real-time video rate volumetric 4D OCT. Multithreading technique was exploited, and two threads, the producer and the consumer threads, were defined. The producer grabs and saves the acquired data into a queue. Meanwhile the consumer processes and visualizes the OCT data. Such adaptation and processing techniques have simplicity advantage. Moreover, the modular structure eases future maintenance and extendibility of the code if any further development required.

Fig.6.8 and Media 1 [161] demonstrate screen captures of the designed user interface to visualize the processed volumetric OCT data acquired from a human retina. The visualization part embraces four sub-windows: en face fundus projection view, cross-sectional view, longitudinal view, and 3D volume rendering. The acquired volumes were processed and visualized based on the proposed algorithm shown in Fig.6.1 without applying any motion correction methods or other image enhancement techniques. The captured volume was processed on a B-scan basis and cross-sectional images were displayed in real-time. The other visualization functions were performed on a volume basis following the volume processing.

The processed data was first copied to a 3D CUDA array and subsequently a 3D texture was bound to the CUDA array, enabling a fast readout of the processed data. CUDA/OpenGL interoperability functions were used to directly display 2D images and render the OCT volumetric data. Such an approach accelerated the display rate by avoiding type conversion and transferring data back to the host.

The *en face* fundus projection was extracted from the processed volume. The *en face* fundus projection is a 2D projection view, generated by the summation of all A-scans within each individual B-scan image of the processed volume. A massive number of summations

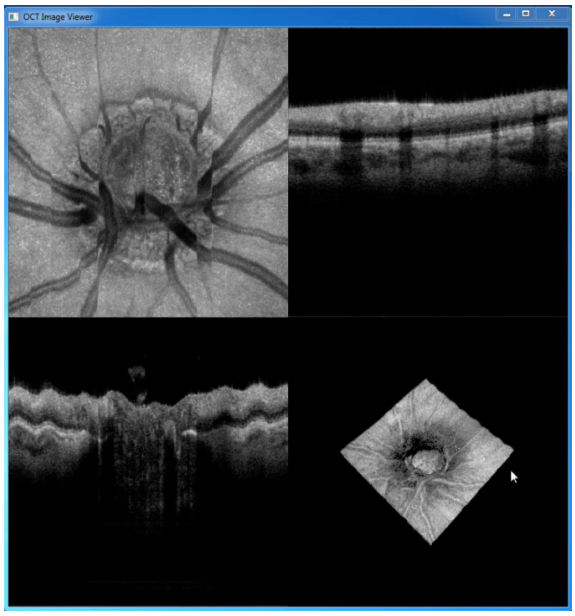

Figure 6.8: A snapshot of the user interface designed for visualization of the processed OCT data. Upper left: En face full projection view (the image shows retina's motion during data acquisition), upper right: B-scan view, lower left: longitudinal view, lower right: 3D volume rendering.

involved to project this view; therefore, an optimized parallel reduction algorithm was employed to perform the summation operations in a parallel and optimized manner [162, 163].

Since the parallel reduction algorithm significantly reduced the processing time, this optimized algorithm was also exploited to generate ensemble average of the prerecorded background images. The longitudinal view was projected by fetching the processed data from the 3D texture. A backward ray tracing method was chosen to render the processed OCT volume [164–166]. The developed application has the ability to interactively rotate, zoom and translate the 3D rendered sample.

Table 6.3 demonstrates the temporal performance results of the real-time video rate volumetric SS-OCT system. The OCT imaging system operated at 400 kHz sweep rate scanning an area of 6 mm × 6 mm with a duty cycle of 80%. The number of samples per A-scan was 928 samples. The temporal performance of each unit was measured and optimized by using NVIDIA Visual Profiler software, a cross-platform performance profiling tool [167]. Different large size volumes were captured, processed and visualized in real-time.

Data Size (A-scans × B-scans)	512×512	1024×512	1024×1024
	Time (ms)	Time (ms)	Time (ms)
Data Copy (H2D)	58.16	114.72	229.68
Data Conversion, Background Subtraction Spectral Shaping & Dispersion Compensation	26.64	59.52	118.56
FFT	31.44	99.84	198.72
Absolute Value & Log Scaling	7.76	18.6	36.84
Ray Tracing	0.33	0.41	0.48
En-face (Full Projection)	6.2	11.92	18.75
Cross-Section Image Display	0.03	0.05	0.07
Longitudinal Image Display	0.04	0.06	0.12
Others (OpenGL, Cuda Pointer Mapping and Unmapping and Internal Data Transfers)	64.6	123.32	194.25
Total GPU Time	195.2	428.44	797.47
Volume Rate (volumes/s)	1.24	0.62	0.31
Efficiency (system A-scan rate/processed A-scans)	81%	81%	81%

Table 6.3: The temporal performance results of the real-time video rate volumetric 4D SS-OCT system.

So far, GPU-based OCT data processing approaches have been implemented for processing of small OCT volumes because of GPU hardware constraints [144–146]. However, the proposed approach has shown the feasibility of real-time processing and 2D/3D visualization of large OCT data volumes by using a single consumer grade GPU. A volume rate of 1.24 volumes/s was achieved for the volume size of 512 A-scans × 512 B-scans. For other two volumes with the size of 1024 A-scans × 512 B-scans and 1024 A-scans × 1024 B-scans, volume rates of 0.62 and 0.31 volumes/s were obtained, respectively. An A-scan processing rate of ∼325 kHz was realized. An efficiency of 81% for all three volumes was gained. The system efficiency is defined as axial scan processing rate divide by actual A-scan rate of the system.

The temporal performance results of processing and visualization units proved highly optimization of the developed GPU modules. The main reason to impede achieving higher volume rate was a bottleneck in acquisition unit. The acquisition and output cards undertook certain procedures as setup in each volume capture, lowering the number of volumes passed

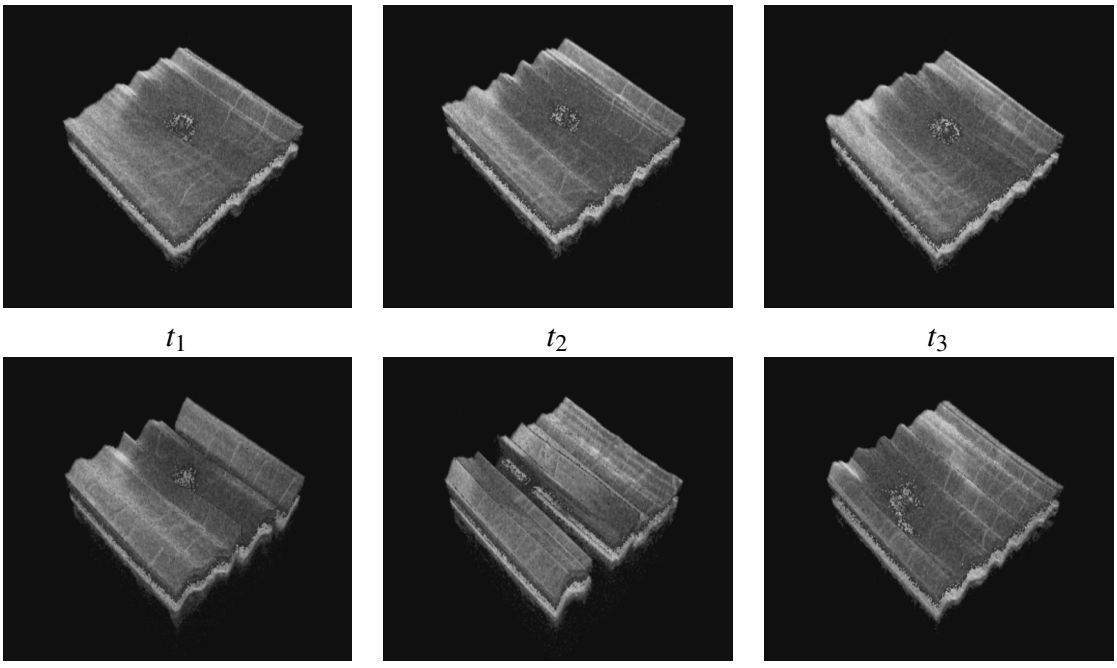

Figure 6.9: Demonstration of retina's motion effect by 4D OCT, built by processing and rendering of six captured data sets (each data set size: 512 A-scans × 512 B-scans × 928 samples per A-scan) at different time ($t_1..t_6$).

to the GPU. Some of the procedures imposing an extra time were disabled to obtain such a volume rate. As future work, the existing C++ code implemented for acquiring the OCT signal and sending the control signals should be restructured and optimized in order to increase the volume rate and efficiency of the system. In addition, the data acquisition card should be setup once in each run instead of each volume capture. The system efficiency would expect to increase to $\sim 95\%$ after such an optimization.

The real-time video rate volumetric 4D OCT systems have some potential applications in medical and industrial fields. The impact of retina's motion was recorded and studied in Media 2 [161]. Six ophthalmic data sets from a human retina were acquired; each set consisted of 3 volumes. In total, 18 volumes (6 data sets $\times$ 3 volumes) were processed and rendered offline. Each volume has the size of 512 A-scans × 512 B-scans × 928 samples per A-scan. The total time of Media 2 is 6 seconds as each data set was rendered and displayed in 1s. Fig.6.9 illustrates 4D OCT of retina's motion obtained by processing and rendering of each individual captured data set at different time ($t_1..t_6$). Motion artifacts associated to the slow speed of the y-scanning mirror can be seen in the rendered volumes in Media 2 [161].

Some applications such as volumetric turbulent flow analysis, live imaging of free-moving small animals (Daphnia and other crustaceans), and surgical guidance for micro-

surgeries have been shown, proving the significance of real-time video rate 4D OCT for future applications [145]. The live 4D OCT was also utilized for characterization of embryonic cardiac function for understanding the genetic specifications of normal development and congenital abnormalities [168]. It was also demonstrated as a powerful tool for OCT-guided micro-injection in mouse embryos [169]. Product in-line monitoring can be other potential application of real-time volumetric 4D OCT for non-destructive and quantitative assessment of products at production lines [41, 120].

6.5 Summary

A GPU-based optimized algorithm to process and visualize acquired volumetric OCT data was proposed. The optimization techniques and all technological challenges to achieve a real-time video rate volumetric 4D OCT were discussed in detail. A live 4D OCT of large volumes by using only a single commercial-grade GPU was accomplished. The large volumes with the size of 512 × 512, 1024 × 512 and 1024 × 1024 depth scans, each depth scan has 928 samples, were processed and rendered in real-time with the rate of 1.24, 0.62 and 0.31 volumes/s, respectively.

The attained A-scan processing rate was ~325 kHz. The system efficiency of 81% was achieved. The temporal performance measurement of the GPU modules proved highly optimization of the processing and visualization units. However, as a future work, the data acquisition unit should be optimized to provide higher volume rate for the GPU. Such an optimization would increase the system efficiency to $\sim 95\%$. Some potential applications of real-time 4D OCT such as dynamic flow analysis, imaging of non-immobilized small animals, surgical guidance for micro-surgeries and micro-injection in mouse embryos, retinal motion study, and product monitoring tool were introduced.

Chapter 7

Quantitative Assessment of PET Preforms Using GPU-Accelerated SD-OCT

This chapter presents the SD-OCT imaging technique as an in-line inspection optical tool for quantitative evaluation of PET laminate preforms. Such an optical imaging solution was proposed for optical thickness measurements performed in real-time to control the quality of produced PET bottle preforms at industrial production lines. In this chapter, the optimization methods described in section 6.3 are employed in order to develop a real-time video rate SD-OCT imaging system at CAP's lab of INESC TEC to be used for sensing and imaging applications.

7.1 Introduction

Nowadays polyethylene terephthalate (PET) bottle preforms are widely used as liquid containers. The PET material offers distinct properties. These properties include high rigidity, temperature tolerance, high safety, low fluid and moisture absorption, high transparency, long life, light weight, and recyclability. Such properties make PET bottles an ideal choice for massive production of beverages packaging and liquid containers such as mineral water, juice, edible oil, pharmaceuticals, cosmetics, and etc.

As explained and depicted in section 5.3, the bottle preforms are manufactured as laminate layers consisting of (a) inner and outer layers of a polyester mainly composed of PET and (b) an intermediate thin film made of ethylene vinyl alcohol (EVOH), placed between the inner and the outer layers. The intermediate layer plays the role of a barrier to lower

the permeability of bottle preforms to oxygen, carbon dioxide and water means in order to protect and maintain the integrity of the product inside. After bottle preform production, it is vital to know that the thin intermediate layer is in place and its thickness is good enough to ensure the functionality of the thin film.

The quality control is performed by destructive means at the production line. Some samples are chosen randomly. These samples are physically cut to separate the layers in order to measure their thickness. This process is usually time consuming and does not follow the speed rate of bottle preform production. In addition, such a destructive testing is suitable only for small set of samples as in the case of massive samples a miss detection of the occurred flaws would result in large losses of the productions. Therefore, an in-line inspection tool to perform real-time measurements of the produced bottle preforms is required.

One widely used method to identify the characteristic of the testing sample is the near-infrared spectroscopy technique [170]. Such an approach is able to determine the material type, the thickness and the color by measuring a spectrum of the absorption in the wavelength region of 350–2500 nm by exploiting a spectrometer. Although the near-infrared spectroscopic method is a high precision method, its response time to analyze the spectrum pattern is slow, making this method suitable for offline process. Moreover, the replacing and adjustment of the new sample takes time and requires an experienced operator. Simpler system configurations were proposed to overcome the aforementioned limitations [170, 171]. These system setups are capable of conducting in-line thickness measurement of flat layers, but they cannot be employed for imaging of highly curved samples such as PET bottle preforms, where the reflectance of the laminate layers vary with the positioning of the sample.

In this chapter, an approach based on spectrally resolved white light interferometry technique is presented to precisely measure the thickness, within the range of micrometers, of the intermediate EVOH laminate film of bottle preforms. An optimized GPU-accelerated signal processing algorithm is proposed to achieve a real-time video rate SD-OCT imaging system to perform such an optical thickness measurement. The proposed in-line measurement solution has nondestructive, high speed and low cost advantages over the conventional methods used at industrial production lines.

7.2 Experimental Setup

A schematic diagram of the system setup and the corresponding implemented experimental setup of the SD-OCT imaging system are illustrated in Fig.7.1. The optical components employed to implement such an imaging system is described in Table 3.2 with their acronyms

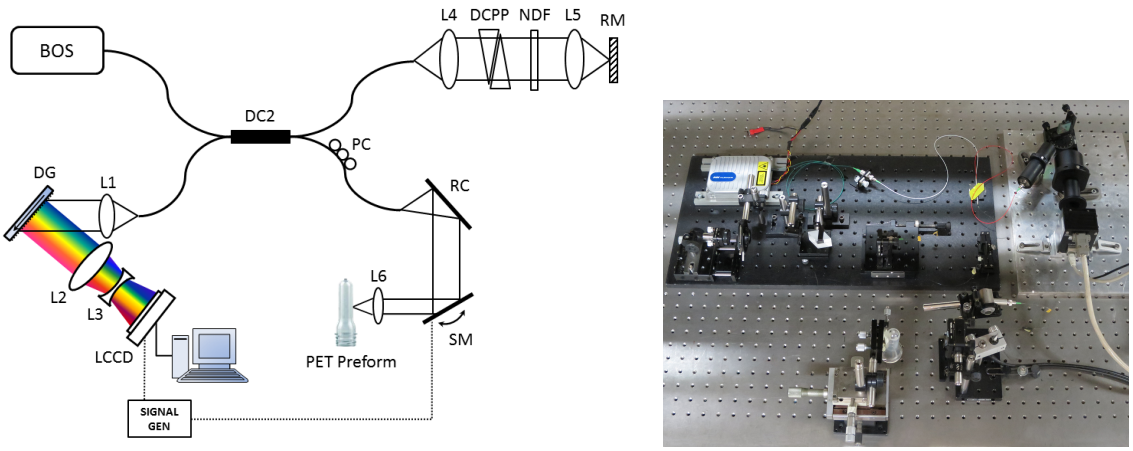

(a) (b)

Figure 7.1: (a) The schematic diagram of the system setup and (b) the corresponding implemented experimental setup of the SD-OCT imaging system. BOS: Broadband Optical Source, DC2: 67/33 Directional Coupler, DCPP: Dispersion-Compensating Prism Pair, NDF: Neutral Density Filter, PC: Polarization Controller, RM: Reference Mirror, RC: Reflective Collimator, SM: Scanning Mirror, DG: Ruled Reflective Diffraction Grating (the arrow shows the direction of the blaze arrow), LCCD: Line-scan Charge Coupled Device Camera, and L1-6: Achromatic Lenses.

used throughout this section. The imaging system consists of the broadband light source BOS, a fiber based Michelson interferometer, and the developed spectrometer with configuration B discussed in sections 3.2.4 and 3.3.

The light is emitted from a Multiwave Photonics' broadband ASE optical source (BOS) with FWHM of 50 nm, central wavelength at ∼1050 nm, and polarized light output power of 20 mW. The light is split by the directional coupler DC2 with the power splitting ratio of 67:33 into the sample (67%) and the reference (33%) arm. The reference arm comprises of the dispersion-compensating prism pair DCPP, the variable neutral density filter NDF, and two achromatic lenses L4 and L5 with the focal length of 15.43 mm and 30 mm, respectively. The dispersion mismatch between two arms caused by L4, L5, L6, and the optical fiber mismatch was compensated by using a pair of dispersion-compensating prism DCPP.

In the sample arm the reflective collimator RC collimates the light toward the galvanometric scanning mirror SM, and the achromatic lens L6 with the focal length of 75 mm is used as an objective lens. Such a configuration enables 2D imaging of testing samples, allowing construction of B-scan images.

As shown in Fig.7.1, the back reflected light from the reference arm and the back scattered light coming from the sample arm are experienced interference at the directional coupler DC2 and detected by the spectrometer with configuration B developed in Chapter 3.

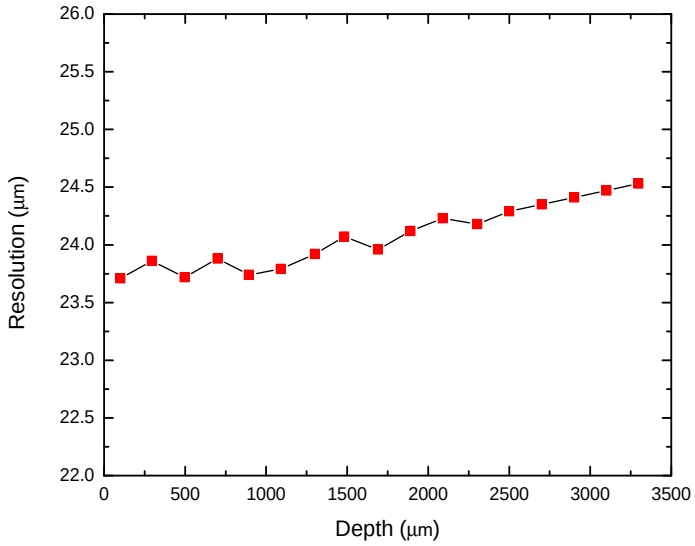

Figure 7.2: The axial resolution of the SD-OCT imaging system as a function of depth, demonstrated over a depth range of $\sim$ 3.2 mm.

Finally, the channeled spectrum data recorded by the line-scan camera LCCD is transferred to a workstation computer by the GigE Vision communication interface protocol, via an Ethernet card. The LCCD and the galvanometric scanning mirror were synchronized using a signal generator to drive the SM, as well as to supply an external frame trigger for the LCCD.

7.3 System Performance Characterization

A flat mirror was used as a sample for all conducted performance characterization measurements reported throughout this section. The maximum imaging depth was measured as $\sim$3.2 mm by changing OPD between two arms until the spectral fringes faded away. Fig.7.2 demonstrates the axial resolution as a function of depth over a depth range of 3.2 mm. The axial resolution was attained by computing the average of the measured FWHM of the axial reflectivity profile at 17 positions along the imaging range. The developed wavelength calibration method discussed in Chapter 4 was exploited to construct the axial reflectivity profile of the imaged flat mirror. The averaged axial resolution was measured as $\sim 24.07\ \mu$m over the depth range of 3.2 mm.

The fringe visibility is maximized if the returning signal from the sample and the reference arms are equal. By doing so, the visibility of 0.93 was attained at OPD 100 μm, when

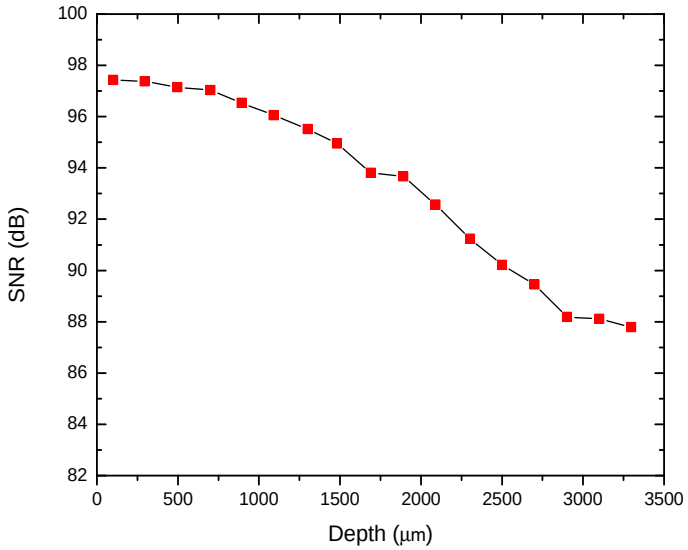

Figure 7.3: The sensitivity fall-off measurement of the SD-OCT imaging system as a function of depth.

the incident power on the testing sample was 0.78 mW. Such a visibility decreases as the difference of optical paths between two arms increases, and it drops to 0.28 at the imaging depth of 3.2 mm. The sensitivity was estimated as ∼97.43 dB by imaging the flat mirror at imaging depth of 100 μm. Eq.5.2 was employed to calculate the sensitivity. The average of the standard deviation of 512 A-scans with the absence of the sample was computed for such a sensitivity measurement. Using Eq.5.2, the SNR repeatedly measured at 17 positions over the imaging range to obtain the system sensitivity fall-off. Fig.7.3 shows the system sensitivity fall-off as a function of depth. The sensitivity fall-off, at maximum depth, was measured as 9.64 dB.

7.4 GPU Signal Processing Algorithm

NVIDIA's compute unified device architecture (CUDA) platform was used to program the GPU, enabling dramatic increase in computing performance [154]. A CUDA-enabled GPU GeForce GTX 680 was installed in a workstation computer with six Intel i7-5930K processing cores, running Microsoft Windows 7 64-bit version. The GPU card has 2 GB memory and 1536 processing cores. The employed motherboard (ASUS X99-DELUXE) and the GPU card both support PCI-Express 3.0 technology, allowing maximum bandwidth for data transfer between system and GPU memory.

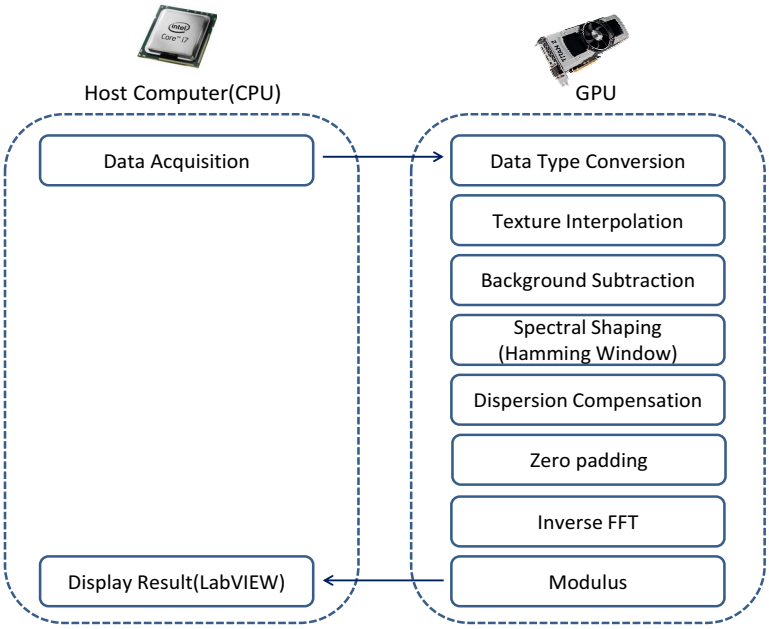

Figure 7.4: The schematic of GPU processing steps for the SD-OCT imaging system.

The OCT signal processing algorithm was implemented and built as a dynamic link library (DLL) file in Microsoft Visual Studio 2010 environment. Another separate application was also designed and implemented as DLL file for data acquisition unit to control the line-scan camera and collect the captured images. The graphical user interface was created by using LabVIE^{TM} 2011 software. The compiled DLL files were directly called in LabVIEW by Call Library Function Node [172]. The screenshots of the developed LabVIEW programs can be found in Appendix C.

A schematic of the signal processing steps performed by GPU is illustrated in Fig.7.4. Raw 512 (spectral lines)$\times$ 2048 (samples/line) spectral images were captured and placed in the system memory (host). A buffer was used to grab the image data continuously without any delay. DALSA camera only permits queuing four images simultaneously [173]; therefore, four spectral images were streamed in at each read. The digitized data was then transferred to the GPU memory (device) by using the optimization techniques explained in section 6.3. Two streams were defined to interleave the GPU operations and run them concurrently. Using PCI-Express generation 3.0 allowed an efficient data transfer at the rate of 8.83 GB/s between device and host.

Each pixel value was converted from 16-bit integer to 32-bit float. The raw images were stored in a CUDA array and bound to a 2D texture memory. This approach enables fast linear data interpolation of pixel values with high computing performance as the re-sampling

is performed in the GPU dedicated texture hardware. The image pixels were interpolated at predefined calibration values, re-sampling the data spectrum in evenly spaced in $k-space$.

The ensemble average of the prerecorded background signal was deducted from each A-scan to obtain the cross-correlation term by removing the auto-correlation artifacts and the noise introduced by the line-scan camera [157]. The ensemble averaging was computed by employing the optimized parallel reduction algorithm to perform the summation operations in a parallel and optimized manner, significantly shortening the time execution [162, 163]. A direct spectral reshaping method, Hamming window, was applied to minimize the side-lobes effect [158]. In addition to the dispersion-compensating prism pair employed in the reference arm, the residual dispersion mismatch between two interferometer's arms was compensated by using a numerical dispersion compensation algorithm proposed in Ref.[78]. This algorithm iteratively modifies the phase of the signal by adjusting the first and the second order of dispersion terms, further enhancing the resolution of the resulting B-scan images.

The re-sampled data was zero-padded prior to Fourier transformation stage to increase the signal resolution by adding zeros to the end of each A-scan. The inverse Fourier transform was computed by employing NVIDIA's dedicated CUDA FFT library known as CUFFT [159]. The absolute value or modulus was taken to bring pixel values from complex Fourier space to real space. The resulting data was ultimately transferred from device to host with the transfer speed of 8.83 GB/s to be displayed by the designed graphical user interface implemented in LabVIEW. The asynchronous data transfer technique, as discussed in section 6.3, was exploited to transfer the data from device to host with high throughput.

7.5 Results and Discussion

The temporal performance of the real-time video rate SD-OCT imaging system is shown in Table 7.1. The time execution measurements are reported for processing of a B-scan image with the size of 512×2048 (A-scans$\times$samples/A-scan). The line-scan camera was operating in high sensitivity mode with the line rate of 36 kHz and the exposure time of 27.8 μs during the acquisition period.

NVIDIA Visual Profiler version 6.5 was used to measure the temporal performance [167]. Such a performance profiling tool enables visualization and performance optimization of the implemented CUDA application. The obtained measurements required an execution version of the application. As the LabVIEW application was implemented as an individual VI file, execution version of the LabVIEW application was built by using "Build Application (EXE) from VI" tool. The employed tool creates a project and then places the

Processing Steps	Time (ms)
Data Copy (H2D) and Data Conversion	0.66
Data Copy (D2H)	0.08
Texture Linear Interpolation	0.73
Background Subtraction, Spectral Shaping, and Dispersion Compensation	0.45
Zero Padding	0.1
Inverse FFT	0.23
Modulus (absolute value)	0.09
Total GPU Time	2.34
Imaging Rate Capability (fps)	427

Table 7.1: The temporal performance results of the real-time SD-OCT imaging system for processing of a B-scan image with the size of 512×2048 (A-scans×samples/A-scan), offering an imaging rate capability of 427 fps. H2D and D2H signify host to device and device to host data transfers, respectively.

execution file inside the project folder.

The total GPU time to produce a 512×2048 (A-scans×samples/A-scan) B-scan image is ∼2.34 ms, demonstrating the ability of GPU to process ∼427 frames/second (fps) in real-time. This frame rate speed enables video rate OCT imaging of moving samples in industrial inspection applications. The current imaging speed including the processing and visualization time is ∼41 fps, corresponding to A-scan processing rate of ∼ 21 kHz. The speed of the passing PET preforms at the production line is ∼7 samples/s, and the current imaging speed is 5.85 times faster than the required speed.

The aforementioned speed of the SD-OCT imaging system is now limited to the readout speed of the line-scan camera. Replacing the existing DALSA camera with the higher line rate camera would significantly increase the speed of the imaging system. Considering the total GPU processing time, such an increased speed can be risen up to ∼427 fps for OCT B-scan images with the size of 512×2048 pixels.

To compare the temporal performance of the CPU- and the GPU-based OCT signal processing routines efficiency, the signal processing steps shown in Fig.7.4 were also implemented in LabVIEW, running only on the system's CPU. The total CPU processing time

Source	Image Size (A-scans×Samples)	Used Processors	Frame Rate	Imaging Rate (Mpixels/s)
K. Zhang et al. [135]	1024 × 512	Single GPU	29.8	15.6
S. Jeught et al. [109]	1024 × 1024	Single GPU	25	26.2
H. Jeong et al. [141]	512 × 1024	Single GPU	120	62.9
D. Xu et al. [64]	1000 × 2048	Triple GPUs	70	143.3
This Study	512 × 2048	Single GPU	427	447.7

Table 7.2: A summary of the previous GPU-based published studies presenting a realtime video rate SD-OCT imaging system.

was $\sim$ 460.82 ms, corresponding to processing and display rate of 2.17 fps, for 512×2048 pixels B-scan images. The obtained result is $\sim$196 times slower than the equivalent GPU-based application used for processing and visualization of OCT images with the same size.

The imaging system speed can be expressed in terms of Megapixels/s (Mpixels/s), easing the comparison of various optical systems. Comparing with the similar GPU-based published studies, K. Zhang et al. implemented non-uniform fast Fourier transform under GPU architecture at the speed rate of 124.9 Mpixels/s [135]. S. Van der Jeught et al. demonstrated a GPU signal processing approach to resample SD-OCT spectral data by using different interpolation methods at the rate of 26.2 Mpixels/s [109]. H. Jeong et al. presented a real-time spectral domain optical Doppler tomography (SD-ODT) to process and display OCT and Doppler images at the rate of 62.9 Mpixels/s [141]. Later, D. Xu et al. developed a live compressive sensing SD-OCT system to visualize B-scan images at the rate of 143.3 Mpixels/s by using triple GPUs [64]. In this study, the developed real-time video rate SD-OCT imaging system processes and displays B-scan images at the speed rate of 427×512×2048 = 447.7 Mpixels/s if the low speed line rate of the employed DALSA camera is neglected. The aforementioned GPU-based studies presenting a realtime video rate SD-OCT imaging system are summarized in Table 7.2.

Fig.7.5.a illustrates the obtained B-scan image of the testing PET preform, showing four reflecting surfaces: air/PET, PET/EVOH, and EVOH/PET and PET/air interfaces. The horizontal scale bars represent 500 μm length. The middle region, 2 cm away from the tip, of a medium size bottle preform was imaged. The PET preform external surface was aligned perpendicular to the incident beam scanning a transverse line of 2 mm length over the testing sample. It is evident in Fig.7.5.a that the laminate PET perform has highly curved multilayer structure as the extreme ends of the scanning area can not be seen in the obtained

(a) (c)

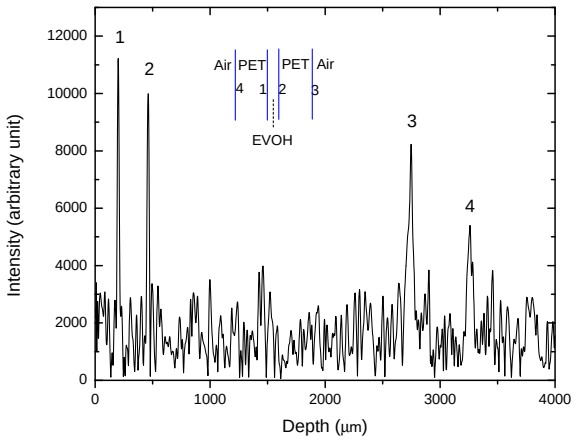

(b)

Figure 7.5: (a) The B-scan OCT image of the examined PET preform placed perpendicular to the direction of the incident beam scanning a transverse line of 2 mm length; (b) an extracted A-scan from the shown B-scan image, used to measure the thickness of laminated PET preform; (c) the post-processed B-scan image after applying the Sobel edge detector in vertical direction. The horizontal scale bars represent 500 μm.

image, and the scanning beam has the right angle with the surface of the testing sample.

The thickness of the EVOH laminate film is estimated from A-scans extracted from B-scan images, such as the one demonstrated in Fig.7.5.b. The optical thickness of EVOH film was measured from the labeled peaks 1 and 2 as ~ 261 μm, corresponding to a physical thickness of ~ 171 μm by considering the EVOH refractive index as 1.525 [114, 174].

The peak labeled as 3 relates to the air/PET interface. The optical thickness between air/PET and PET/EVOH (the peak labeled as 2) interfaces was measured as ~ 2285 μm. Such an optical thickness is equivalent to the physical thickness of ~ 1.45 mm, considering the refractive index of PET as 1.575 [114, 174]. The peak labeled as 4 corresponds to the PET/air interface. The measured optical thickness between EVOH/PET (the peak labeled as 1) and PET/air was ~ 3460 μm, corresponding to the physical thickness of ~ 2.19 mm. All

	Optical Thickness (μm)	Physical Thickness (μm)
EVOH Film	$261 \pm \sim 2$	171
Air/PET - PET/EVOH	$2285 \pm \sim 2$	1451
EVOH/PET - PET/Air	$3460 \pm \sim 2$	2197

Table 7.3: Thickness measurement results of different layers of the testing PET preform.

performed thickness measurements are summarized in Table 7.3. All measured thicknesses were in good agreement with the destructive test performed to validate the accuracy of the obtained results.

The resulting B-scan image demonstrated in Fig.7.5.a was processed in post-processing stage by using MATLAB software. As the resulting image consists of vertical lines, a Sobel operator was employed to detect and emphasize the edges in vertical direction. Such an operator computed an approximation of the gradient of the image intensity in y-direction and determined the edges at points where the gradient was maximum. Fig.7.5.c shows the result of the post-processed B-scan image after applying the Sobel edge detector in vertical direction. Fig.7.5.c demonstrates that such a simple post-processing procedure can be added and implemented under GPU architecture to automate the thickness measurement computation of multilayered PET preform at production lines. In addition, this approach better visualizes the distance between layers for the operators working at production line. The implemented MATLAB code for such a post-processing can be found in Appendix D.3.

7.6 Summary

The designed and implemented spectrometer with configuration B, described in Chapter 3, was integrated into the SD-OCT imaging system. Such a system was considered to perform 2D imaging in order to obtain OCT cross-sectional images, known as B-scan, of testing samples. The developed imaging system was characterized based on principal performance parameters discussed in Chapter 5. The characterization assessment was reported, and was also summarized in Appendix A for future reference.

In this chapter, an optimized GPU-based signal processing algorithm was proposed to process and visualize B-scan images in real-time. A live video rate SD-OCT imaging system was achieved, processing each cross-sectional OCT image of size 512×2048 pixels in only 2.34 ms by using a low-cost consumer grade GPU card. It was shown that the pro-

posed GPU-based approach has speed advantages over conventional CPU-based OCT data processing approaches.

The developed high performance imaging system was presented as an in-line inspection optical tool for quantitative assessment of PET bottle preforms non-destructively at industrial production lines. The PET preform imaging results were demonstrated, aiming to evaluate the thickness of EVOH laminate film for control quality purpose. A post-processing procedure was proposed to automate the computation of optical thickness measurements of laminated bottle PET preforms. This approach facilitates the measurement and better visualizes bottle PET preform layers for the operators working at production lines.

The proposed GPU-accelerated optical imaging approach has nondestructive, high speed, and low-cost distinct advantages over the conventional methods employed at production lines. The real-time video rate SD-OCT imaging system was developed at CAP's lab of INESC TEC for sensing and imaging applications.

Chapter 8

Conclusion and Future Work

8.1 Conclusion

This thesis has presented highly optimized GPU-based signal processing algorithms and 2D/3D visualization methods for SD- and SS-OCT imaging systems. The proposed algorithms employed massively parallel computing techniques to process and visualize OCT images in real-time. Such GPU accelerated implementations enabled development of real-time video rate volumetric 4D OCT imaging system. In Chapter 6, all optimization methods to implement an efficient data processing and fast display were described. All technological challenges to achieve a real-time video rate imaging systems were discussed in detail in Chapters 6 and 7.

So far, the GPU-based processing and visualization methods have been shown in literature for small OCT volumes due to GPU memory latency and resource constraints. In contrast, the presented work in Chapter 6 demonstrated real-time data processing and visualization methods for large OCT volumes (1024 A-scans$\times$1024 B-scans) with the high efficiency of 81% by using only a single commercial-grade GPU.

The developed approach is very beneficial, and it has a great potential application in intraoperative OCT systems. The real-time video rate volumetric 4D SS-OCT imaging system is being deployed at New England Eye Center as a surgical guidance tool to perform micro-surgeries, empowering surgeons by providing real-time intraoperative feedbacks. The acquisition and real-time processing of large OCT volumes enable physicians to scan a large area in order to have a better understanding of anatomy, thus enhancing surgical decision-making during surgeries.

Some other potential applications of volumetric 4D OCT such as dynamic flow analysis, imaging of non-immobilized small animals, micro-injection in mouse embryos, and product monitoring and control quality inspection tool were introduced throughout this thesis. The

retinal motion was demonstrated by rendering 18 OCT data volumes, each with the size of 512 A-scans×512 B-scans×928 samples/A-scan, acquired from a human eye. The resulting 4D OCT video presented in Chapter 6 clearly showed the slow and fast motion of the retina during the acquisition.

The obtained temporal performance results have proved highly optimization of each implemented GPU module. The reported temporal performance in section 6.4 was expressed as "GVoxels/s" to ease the comparison of the obtained results with other studies. The attained processing time execution results outperforms the fastest processing speed published thus far [145].

The overall performance of the existing SD-OCT imaging system at the CAP's lab of INESC TEC was significantly improved in terms of axial resolution (improved twofold), imaging range (increased by more than threefold) and processing speed (increased/limited to the maximum line rate speed of the camera). In Chapter 3, a spectrometer with two focusing optics configurations were designed, implemented and integrated into the CP-SD-OCT and the SD-OCT imaging systems at CAP's lab. The design steps and the approaches to choose appropriate spectrometer components to improve the overall performance were explained in Chapter 3. Such a spectrometer design and optimization allowed imaging of micro multilayer structures with higher axial resolution and increased imaging range.

The spectral calibration and data re-sampling methods were numerically implemented in Chapter 4. The significance role of $k-$space linearization and spectral calibration procedure in achieving the highest signal resolution was demonstrated. The developed calibration method was employed for all future SD-OCT signal processing under GPU architecture.

The spectrometer with configuration A was integrated into the CP-SD-OCT imaging system in order to perform 1D imaging, while the spectrometer with configuration B was integrated into the SD-OCT imaging system for 2D imaging to obtain cross-sectional images of testing samples. Such imaging systems were used to measure the optical and physical thickness of micro multilayer structures with micron scale precision. Both imaging systems were characterized based on some principal performance characterization parameters, aiming to raise awareness of the strength and limitation of the imaging systems to better perform imaging.

In Chapter 7, an optimized approach to develop a real-time video rate SD-OCT imaging system to process and visualize B-scan images was described. The temporal performance results of the employed algorithm were detailed in Chapter 7. It was shown that the proposed GPU-based method was $\sim$196 times faster than the corresponding CPU-based approach to process and visualize cross-sectional images with the size of 512×2048 pixels. The developed live video rate SD-OCT imaging system was presented as an in-line inspection optical

tool for quantitative assessment of PET bottle preforms non-destructively at industrial production lines. A post-processing procedure was implemented to automate the computation of thickness measurements of laminated bottle PET preforms. Such a post-processing approach eases the measurements and better visualizes multilayer structure of PET preforms for the operators working at industrial production lines.

The highly optimized SD-OCT imaging system has now the imaging speed of $\sim$41 fps, each frame size is 512×2048 pixels. As the speed of the passing PET preforms is $\sim$7 samples/s, the imaging system speed is currently more than the required speed at the production line. In addition to such a high speed, the proposed optical approach has non-destructive and low-cost distinct advantages over the traditional approaches employed at production lines.

The developed real-time video rate volumetric 4D SS-OCT imaging system at the RLE Laser Medicine and Medical Imaging Group of MIT, and the real-time video rate SD-OCT imaging system at the CAP Group of INESC TEC now serve as a base for future experiments and studies at both groups. At the RLE group, it is employed for intraoperative OCT and biomedical imaging applications, whereas at the CAP group, it is mainly exploited for industrial nondestructive testing applications. The implemented highly parallelized and optimized signal processing and visualization methods empower both groups to easily perform real-time structural and functional imaging for the studies requiring an ultrahigh-speed imaging system.

8.2 Future Work

The real-time video rate SD-OCT and SS-OCT imaging systems can be further developed in future. Here are some possible directions to advance these two imaging systems:

The proposed post-processing image processing algorithm to detect two surfaces of EVOH laminate layer is greatly helpful to automatically estimate the physical thickness of this intermediate layer. The gradient based edge detector can be implemented by GPU to detect the edges of B-scan images and compute the distance in real-time. As another solution, a GPU-based peak detector module can also be implemented to find the peaks and calculate the distance between them.

A second scanning mirror can be added to the sample arm of the developed SD-OCT imaging system, resulting in generation of OCT data volumes. This hardware upgrade would pave the way for the development of a real-time video rate volumetric 4D SD-OCT imaging system at CAP's lab. Such an imaging system can be used as a powerful tool for structural and functional imaging studies of embryonic cardiovascular system of small ani-

mals such as chicken or mouse. As the human hearts begin to form and beat before being imaged by ultrasound, physicians have little information about heart dynamics and function in humans. Therefore, most studies are nowadays heavily based on animals to find out the cause of the abnormalities in the growth and development of the cardiovascular system of human embryos. Such future studies at CAP's lab would contribute to the understanding of the leading cause of the most common type of congenital birth defects.

As the GPU card in the intraoperative OCT system consists of two GPUs connecting to each other by a peer-to-peer bus (PCI-Express generation 3.0), one GPU can be dedicated for data processing and the other for 2D/3D visualization of the processed data. In this approach, the first GPU processes the captured OCT volumes on a B-scan basis while the second GPU is displaying the processed B-scan images and updating the rendered volume. In addition to this approach, the existing C++ code should be restructured such that the data acquisition card is setup only once for each run instead of each volume capture. Such an optimization would significantly increase the current efficiency to $\sim$95%.

References

[1] Peter Morris. *Biomedical Imaging: Applications and Advances*. Elsevier, 2014.

[2] Troy Farncombe and Kris Iniewski. *Medical Imaging: Technology and Applications*. CRC Press, 2013.

[3] Nadine Barrie Smith and Andrew Webb. *Introduction to medical imaging: physics, engineering and clinical applications*. Cambridge university press, 2010.

[4] David Huang, Eric A Swanson, Charles P Lin, Joel S Schuman, William G Stinson, Warren Chang, Michael R Hee, Thomas Flotte, Kenton Gregory, Carmen A Puliafito, et al. Optical coherence tomography. *Science*, 254(5035):1178–1181, 1991.

[5] Ch W Sensen and Benedikt Hallgrimsson. *Advanced Imaging in Biology and Medicine: Technology, Software Environments, Applications (Chapter 5)*. Springer Science & Business Media, 2008.

[6] Wolfgang Drexler, Mengyang Liu, Abhishek Kumar, Tschackad Kamali, Angelika Unterhuber, and Rainer A Leitgeb. Optical coherence tomography today: speed, contrast, and multimodality. *Journal of biomedical optics*, 19(7):071412–071412, 2014.

[7] Evelyn Regar, AMGJ van Leeuwen, and Patrick W Serruys. *Optical coherence tomography in cardiovascular research*. CRC Press, 2007.

[8] James G Fujimoto, Costas Pitris, Stephen A Boppart, and Mark E Brezinski. Optical coherence tomography: an emerging technology for biomedical imaging and optical biopsy. *Neoplasia*, 2(1):9–25, 2000.

[9] Shoude Chang, Youxin Mao, Costel Flueraru, and Sherif Sherif. Optical coherence tomography: technology and applications. In *International Conference of Optical Instrument and Technology*, pages 715606–715606. International Society for Optics and Photonics, 2008.

[10] Joel A Kubby. *Adaptive Optics for Biological Imaging*. CRC press, 2013.

[11] A. Gh. Podoleanu. Optical coherence tomography. *Journal of Microscopy*, 247(3):209–219, 2012.

[12] Wolfgang Drexler. Ultrahigh-resolution optical coherence tomography. *Journal of biomedical optics*, 9(1):47–74, 2004.

[13] Michael Choma, Marinko Sarunic, Changhuei Yang, and Joseph Izatt. Sensitivity advantage of swept source and fourier domain optical coherence tomography. *Optics express*, 11(18):2183–2189, 2003.

[14] John H Kempen, Elizabeth A Sugar, Glenn J Jaffe, Nisha R Acharya, James P Dunn, Susan G Elner, Susan L Lightman, Jennifer E Thorne, Albert T Vitale, Michael M Altaweel, et al. Fluorescein angiography versus optical coherence tomography for diagnosis of uveitic macular edema. *Ophthalmology*, 120(9):1852–1859, 2013.

[15] Thomas Klein, Wolfgang Wieser, Lukas Reznicek, Aljoscha Neubauer, Anselm Kampik, and Robert Huber. Multi-mhz retinal OCT. *Biomedical optics express*, 4(10):1890–1908, 2013.

[16] Tiancheng Huo, Chengming Wang, Xiao Zhang, Tianyuan Chen, Wenchao Liao, Wenxin Zhang, Shengnan Ai, Jui-Cheng Hsieh, and Ping Xue. Ultrahigh-speed optical coherence tomography utilizing all-optical 40 mhz swept-source. *Journal of biomedical optics*, 20(3):030503–030503, 2015.

[17] Sven Nebelung, Nicolai Brill, Ulrich Marx, Valentin Quack, Markus Tingart, Robert Schmitt, Björn Rath, and Holger Jahr. Three-dimensional imaging and analysis of human cartilage degeneration using optical coherence tomography. *Journal of Orthopaedic Research*, 33(5):651–659, 2015.

[18] Maciej Wojtkowski, Vivek Srinivasan, James G Fujimoto, Tony Ko, Joel S Schuman, Andrzej Kowalczyk, and Jay S Duker. Three-dimensional retinal imaging with high-speed ultrahigh-resolution optical coherence tomography. *Ophthalmology*, 112(10):1734–1746, 2005.

[19] Jina Kim, William Brown, Jason R Maher, Howard Levinson, and Adam Wax. Functional optical coherence tomography: principles and progress. *Physics in medicine and biology*, 60(10):R211, 2015.

[20] Byeong Ha Lee, Eun Jung Min, and Young Ho Kim. Fiber-based optical coherence tomography for biomedical imaging, sensing, and precision measurements. *Optical Fiber Technology*, 19(6, Part B):729 – 740, 2013.

[21] Pier Alberto Testoni. Optical coherence tomography. *The Scientific World Journal*, 7:87–108, 2007.

[22] Matthew B Sturm and Thomas D Wang. Emerging optical methods for surveillance of barrett's oesophagus. *Gut*, pages gutjnl–2013, 2015.

[23] Tsung-Han Tsai, Benjamin Potsaid, Yuankai K Tao, Vijaysekhar Jayaraman, James Jiang, Peter JS Heim, Martin F Kraus, Chao Zhou, Joachim Hornegger, Hiroshi Mashimo, et al. Ultrahigh speed endoscopic optical coherence tomography using micromotor imaging catheter and VCSEL technology. *Biomedical optics express*, 4(7):1119–1132, 2013.

[24] A. Garg. *Anterior & Posterior Segment OCT: Current Technology & Future Applications*. Jaypee Brothers,Medical Publishers Pvt. Limited, 2014.

[25] Jay S Duker, Nadia K Waheed, and Darin Goldman. *Handbook of Retinal OCT: Optical Coherence Tomography*. Elsevier Health Sciences, 2013.

[26] Joel S Schuman, Carmen A Puliafito, James G Fujimoto, and Jay S Duker. *Optical coherence tomography of ocular diseases*. Slack New Jersey, 2004.

[27] D.A. Landry. *Optical Coherence Tomography, A Clinical Atlas of Retinal Images*. Bryson Taylor Publishing, 2013.

[28] Ik-Kyung Jang. *Cardiovascular OCT Imaging*. Springer, 2015.

[29] Tsung-Han Tsai. *Endoscopic optical coherence tomography for clinical studies in the gastrointestinal tract*. PhD thesis, Massachusetts Institute of Technology, 2013.

[30] Kaicheng Liang, Giovanni Traverso, Hsiang-Chieh Lee, Osman Oguz Ahsen, Zhao Wang, Benjamin Potsaid, Michael Giacomelli, Vijaysekhar Jayaraman, Ross Barman, Alex Cable, et al. Ultrahigh speed en face OCT capsule for endoscopic imaging. *Biomedical optics express*, 6(4):1146–1163, 2015.

[31] Michalina J Gora, Jenny S Sauk, Robert W Carruth, Kevin A Gallagher, Melissa J Suter, Norman S Nishioka, Lauren E Kava, Mireille Rosenberg, Brett E Bouma, and Guillermo J Tearney. Tethered capsule endomicroscopy enables less invasive imaging of gastrointestinal tract microstructure. *Nature medicine*, 19(2):238–240, 2013.

[32] Eben Rosenthal and Kurt R Zinn. *Optical Imaging of Cancer, Clinical Applications*. Springer, 2009.

[33] Benjamin J Vakoc, Dai Fukumura, Rakesh K Jain, and Brett E Bouma. Cancer imaging by optical coherence tomography: preclinical progress and clinical potential. *Nature Reviews Cancer*, 12(5):363–368, 2012.

[34] Hisaichi Nakagawa, Alireza Sadr, Yasushi Shimada, Junji Tagami, and Yasunori Sumi. Validation of swept source optical coherence tomography (SS-OCT) for the diagnosis of smooth surface caries in vitro. *Journal of Dentistry*, 41(1):80 – 89, 2013.

[35] Enzo Berardesca, Howard Maibach, and Klaus Wilhelm. *Non Invasive Diagnostic Techniques in Clinical Dermatology*. Springer Science & Business Media, 2013.

[36] Elke Sattler, Raphaela Kästle, and Julia Welzel. Optical coherence tomography in dermatology. *Journal of biomedical optics*, 18(6):061224–061224, 2013.

[37] Richard Haindl, Wolfgang Karl Trasischker, Bernhard Baumann, Michael Pircher, and Christoph K Hitzenberger. Measurement of absolute velocity and flow of moving scatterers in retinal veins using 3-beam doppler optical coherence tomography. *Investigative Ophthalmology & Visual Science*, 55(13):218–218, 2014.

[38] Bernhard Baumann, WooJhon Choi, Benjamin Potsaid, David Huang, Jay S Duker, and James G Fujimoto. Swept source/Fourier domain polarization sensitive optical coherence tomography with a passive polarization delay unit. *Optics express*, 20(9):10229–10241, 2012.

[39] D Stifter. Beyond biomedicine: a review of alternative applications and developments for optical coherence tomography. *Applied Physics B*, 88(3):337–357, 2007.

[40] CS Cheung, M Spring, and H Liang. Ultra-high resolution Fourier domain optical coherence tomography for old master paintings. *Optics express*, 23(8):10145–10157, 2015.

[41] Daniel Markl, Günther Hannesschläger, Stephan Sacher, Michael Leitner, and Johannes G Khinast. Optical coherence tomography as a novel tool for in-line monitoring of a pharmaceutical film-coating process. *European Journal of Pharmaceutical Sciences*, 55:58–67, 2014.

[42] CAP Group at INESC TEC. https://www.inesctec.pt/cap, February 2016.

[43] RLE Laser Medicine and Medical Imaging Group at the Massachusetts Institute of Technology. http://www.rle.mit.edu/boib, February 2016.

[44] Mark E Brezinski. *Optical coherence tomography: principles and applications*. Academic press, 2006.

[45] Ruikang K Wang and Valery V Tuchin. *Advanced biophotonics: tissue optical sectioning*. CRC Press, 2013.

[46] A Gh Podoleanu. Optical coherence tomography. *The British Journal of Radiology*, 78(935):976–988, 2005. PMID: 16249597.

[47] R Leitgeb, C Hitzenberger, and Adolf Fercher. Performance of fourier domain vs. time domain optical coherence tomography. *Optics Express*, 11(8):889–894, 2003.

[48] Yuuki Watanabe, Fumitoshi Sajima, Toshiki Itagaki, Kei Watanabe, and Yuuki Shuto. High-speed linear detection time domain optical coherence tomography with reflective grating-generated spatial reference delay. *Applied optics*, 48(18):3401–3406, 2009.

[49] Maciej Wojtkowski. High-speed optical coherence tomography: basics and applications. *Applied Optics*, 49(16):D30–D61, 2010.

[50] Adolph F Fercher, Ch K Hitzenberger, G Kamp, and Sy Y El-Zaiat. Measurement of intraocular distances by backscattering spectral interferometry. *Optics Communications*, 117(1):43–48, 1995.

[51] Hiroshi Shibata, Nobuhiko Ozaki, Takuma Yasuda, Shunsuke Ohkouchi, Naoki Ikeda, Hirotaka Ohsato, Eiichiro Watanabe, Yoshimasa Sugimoto, Kenji Furuki, Kunio Miyaji, et al. Imaging of spectral-domain optical coherence tomography using a superluminescent diode based on InAs quantum dots emitting broadband spectrum with Gaussian-like shape. *Japanese Journal of Applied Physics*, 54(4S):04DG07, 2015.

[52] Mohammad Kamal. *Reflective optics-based line-scanning spectral domain optical coherence tomography system*. PhD thesis, Concordia University, 2011.

[53] S Yun, G Tearney, Johannes de Boer, N Iftimia, and B Bouma. High-speed optical frequency-domain imaging. *Optics Express*, 11(22):2953–2963, 2003.

[54] Peter H Tomlins and RK Wang. Theory, developments and applications of optical coherence tomography. *Journal of Physics D: Applied Physics*, 38(15):2519, 2005.

[55] Johannes F De Boer, Barry Cense, B Hyle Park, Mark C Pierce, Guillermo J Tearney, and Brett E Bouma. Improved signal-to-noise ratio in spectral-domain compared with time-domain optical coherence tomography. *Optics letters*, 28(21):2067–2069, 2003.

[56] Zahid Yaqoob, Jigang Wu, and Changhuei Yang. Spectral domain optical coherence tomography: a better OCT imaging strategy. *Biotechniques*, 39, 2005.

[57] Adrian Bradu and Adrian Gh Podoleanu. Attenuation of mirror image and enhancement of the signal-to-noise ratio in a talbot bands optical coherence tomography system. *Journal of biomedical optics*, 16(7):076010–076010, 2011.

[58] Adrian Bachmann, Rainer Leitgeb, and Theo Lasser. Heterodyne Fourier domain optical coherence tomography for full range probing with high axial resolution. *Optics express*, 14(4):1487–1496, 2006.

[59] Wolfgang Drexler and James G Fujimoto. *Optical coherence tomography: technology and applications*. Springer Science & Business Media, 2008.

[60] Michael W Jenkins, Osman Q Chughtai, Ajay N Basavanhally, Michiko Watanabe, and Andrew M Rollins. In vivo gated 4D imaging of the embryonic heart using optical coherence tomography. *Journal of biomedical optics*, 12(3):030505–030505, 2007.

[61] Gangjun Liu, Jun Zhang, Lingfeng Yu, Tuqiang Xie, and Zhongping Chen. Real-time polarization-sensitive optical coherence tomography data processing with parallel computing. *Applied optics*, 48(32):6365–6370, 2009.

[62] Shikui Yan, Daqing Piao, Yueli Chen, and Quing Zhu. Digital signal processor-based real-time optical doppler tomography system. *Journal of biomedical optics*, 9(3):454–463, 2004.

[63] Adrian Bradu, Konstantin Kapinchev, Frederick Barnes, and Adrian Podoleanu. On the possibility of producing true real-time retinal cross-sectional images using a graphics processing unit enhanced master-slave optical coherence tomography system. *Journal of biomedical optics*, 20(7):076008–076008, 2015.

[64] Daguang Xu, Yong Huang, and Jin U Kang. Real-time compressive sensing spectral domain optical coherence tomography. *Optics letters*, 39(1):76–79, 2014.

[65] Adolf F Fercher, Wolfgang Drexler, Christoph K Hitzenberger, and Theo Lasser. Optical coherence tomography-principles and applications. *Reports on progress in physics*, 66(2):239, 2003.

[66] W Drexler, U Morgner, FX Kärtner, C Pitris, SA Boppart, XD Li, EP Ippen, and JG Fujimoto. In vivo ultrahigh-resolution optical coherence tomography. *Optics letters*, 24(17):1221–1223, 1999.

[67] David A Boas, Constantinos Pitris, and Nimmi Ramanujam. *Handbook of biomedical optics*. CRC press, 2011.

[68] James G Fujimoto. Optical coherence tomography. *Comptes Rendus de l'Académie des Sciences - Series IV - Physics*, 2(8):1099–1111, 2001.

[69] Kenny K. H. Chan. *Spectral domain optical coherence tomography system design: sensitivity fall-off and processing speed enhancement*. PhD thesis, University of British Columbia, 2010.

[70] Donghak Choi, Hideaki Hiro-Oka, Takuji Amano, Hiroyuki Furukawa, Fumiyoshi Kano, Motoi Nakanishi, Kimiya Shimizu, and Kohji Ohbayashi. Numerical compensation of dispersion mismatch in discretely swept optical-frequency-domain-reflectometry optical coherence tomography. *Japanese journal of applied physics*, 45(7R):6022, 2006.

[71] Adolf Fercher, Christoph Hitzenberger, Markus Sticker, Robert Zawadzki, Boris Karamata, and Theo Lasser. Numerical dispersion compensation for partial coherence interferometry and optical coherence tomography. *Optics Express*, 9(12):610–615, 2001.

[72] CK Hitzenberger, A Baumgartner, and AF Fercher. Dispersion induced multiple signal peak splitting in partial coherence interferometry. *Optics Communications*, 154(4):179–185, 1998.

[73] Max Born and Emil Wolf. *Principles of optics: electromagnetic theory of propagation, interference and diffraction of light*. Cambridge university press, 1999.

[74] Timothy Hillman and David Sampson. The effect of water dispersion and absorption on axial resolution in ultrahigh-resolution optical coherence tomography. *Optics express*, 13(6):1860–1874, 2005.

[75] GJ Tearney, BE Bouma, and JG Fujimoto. High-speed phase-and group-delay scanning with a grating-based phase control delay line. *Optics Letters*, 22(23):1811–1813, 1997.

[76] Michael Leitner. *White Light Interferometry applications in high resolution sensing and biomedical imaging*. PhD thesis, University of Porto, 2010.

[77] Carla C Rosa, John Rogers, and Adrian Gh Podoleanu. Fast scanning transmissive delay line for optical coherence tomography. *Optics letters*, 30(24):3263–3265, 2005.

[78] Maciej Wojtkowski, Vivek Srinivasan, Tony Ko, James Fujimoto, Andrzej Kowalczyk, and Jay Duker. Ultrahigh-resolution, high-speed, Fourier domain optical coherence tomography and methods for dispersion compensation. *Optics express*, 12(11):2404–2422, 2004.

[79] AF Fercher, CK Hitzenberger, M Sticker, R Zawadzki, B Karamata, and T Lasser. Dispersion compensation for optical coherence tomography depth-scan signals by a numerical technique. *Optics Communications*, 204(1):67–74, 2002.

[80] Daniel L Marks, Amy L Oldenburg, J Joshua Reynolds, and Stephen A Boppart. Autofocus algorithm for dispersion correction in optical coherence tomography. *Applied optics*, 42(16):3038–3046, 2003.

[81] Johannes F de Boer, Christopher E Saxer, and J Stuart Nelson. Stable carrier generation and phase-resolved digital data processing in optical coherence tomography. *Applied Optics*, 40(31):5787–5790, 2001.

[82] Adolf Friedrich Fercher. Optical coherence tomography–development, principles, applications. *Zeitschrift für Medizinische Physik*, 20(4):251–276, 2010.

[83] Peng Xi, Kai Mei, Tobias Bräuler, Chuanqing Zhou, and Qiushi Ren. Evaluation of spectrometric parameters in spectral-domain optical coherence tomography. *Applied optics*, 50(3):366–372, 2011.

[84] Mohammad Kamal, Sivakumar Narayanswamy, and Muthukumaran Packirisamy. Design of spectrometer for high-speed line field optical coherence tomography. In *Photonics North 2011*, pages 80071J–80071J. International Society for Optics and Photonics, 2011.

[85] Benjamin Potsaid, Iwona Gorczynska, Vivek J Srinivasan, Yueli Chen, James Jiang, Alex Cable, and James G Fujimoto. Ultrahigh speed spectral/Fourier domain OCT

ophthalmic imaging at 70,000 to 312,500 axial scans per second. *Optics express*, 16(19):15149–15169, 2008.

[86] BI Akca, B Považay, A Alex, K Wörhoff, RM De Ridder, W Drexler, and M Pollnau. Miniature spectrometer and beam splitter for an optical coherence tomography on a silicon chip. *Optics express*, 21(14):16648–16656, 2013.

[87] Arthur Nitkowski, Kyle Preston, Nicolás Sherwood-Droz, Bradley S Schmidt, and Arsen R Hajian. On-chip spectrometer for low-cost optical coherence tomography. In *SPIE BiOS*, pages 89340F–89340F. International Society for Optics and Photonics, 2014.

[88] BImran Akca, Victor Nguyen, Jeroen Kalkman, Nur Ismail, Gabriel Sengo, Fei Sun, Alfred Driessen, Ton G van Leeuwen, Markus Pollnau, Kerstin Worhoff, et al. Toward spectral-domain optical coherence tomography on a chip. *Selected Topics in Quantum Electronics, IEEE Journal of*, 18(3):1223–1233, 2012.

[89] B Imran Akca, V Duc Nguyen, Jeroen Kalkman, Ton G van Leeuwen, Kerstin Worhoff, Rene de Ridder, and Markus Pollnau. Integrated spectrometers for spectral-domain optical coherence tomography. In *The European Conference on Lasers and Electro-Optics*, page CLEB5_4. Optical Society of America, 2011.

[90] V Duc Nguyen, B Imran Akca, Kerstin Wörhoff, René M De Ridder, Markus Pollnau, Ton G van Leeuwen, and Jeroen Kalkman. Spectral domain optical coherence tomography imaging with an integrated optics spectrometer. *Optics letters*, 36(7):1293–1295, 2011.

[91] Zhilin Hu and Andrew M Rollins. Fourier domain optical coherence tomography with a linear-in-wavenumber spectrometer. *Optics letters*, 32(24):3525–3527, 2007.

[92] Mohammad Kamal, Narayanswamy Sivakumar, and Muthukumaran Packirisamy. Design of a spectrometer for all-reflective optics-based line scan Fourier domain optical coherence tomography. In *Photonics North 2010*, pages 775020–775020. International Society for Optics and Photonics, 2010.

[93] Teledyne DALSA. Spyder 3 GigE User's Manual. http://goo.gl/1I5rgi, February 2016.

[94] Bahaa EA Saleh, Malvin Carl Teich, and Bahaa E Saleh. *Fundamentals of photonics*, volume 22. Wiley New York, 1991.

[95] Christopher A Palmer, Erwin G Loewen, and RGL Thermo. *Diffraction grating handbook*. Newport Corporation Springfield, Ohio, USA, 2005.

[96] Thorlabs. GR25-1210 Ruled Reflective Diffraction Grating. https://goo.gl/zsASQE, February 2016.

[97] WinLens Optical Design Software. http://www.winlens.de/, January 2016.

[98] VM Gelikonov, GV Gelikonov, and PA Shilyagin. Linear-wavenumber spectrometer for high-speed spectral-domain optical coherence tomography. *Optics and Spectroscopy*, 106(3):459–465, 2009.

[99] Desmond C Adler, Yu Chen, Robert Huber, Joseph Schmitt, James Connolly, and James G Fujimoto. Three-dimensional endomicroscopy using optical coherence tomography. *Nature Photonics*, 1(12):709–716, 2007.

[100] Kai Wang and Zhihua Ding. Spectral calibration in spectral domain optical coherence tomography. *Chinese Optics Letters*, 6(12):902–904, 2008.

[101] Shuichi Makita, Tapio Fabritius, and Yoshiaki Yasuno. Full-range, high-speed, high-resolution 1-μm spectral-domain optical coherence tomography using bm-scan for volumetric imaging of the human posterior eye. *Optics express*, 16(12):8406–8420, 2008.

[102] Maciej Szkulmowski, Maciej Wojtkowski, Tomasz Bajraszewski, Iwona Gorczyńska, Piotr Targowski, Wojciech Wasilewski, Andrzej Kowalczyk, and Czesław Radzewicz. Quality improvement for high resolution in vivo images by spectral domain optical coherence tomography with supercontinuum source. *Optics communications*, 246(4):569–578, 2005.

[103] Barry Cense, Nader Nassif, Teresa Chen, Mark Pierce, Seok-Hyun Yun, B Park, Brett Bouma, Guillermo Tearney, and Johannes de Boer. Ultrahigh-resolution high-speed retinal imaging using spectral-domain optical coherence tomography. *Optics Express*, 12(11):2435–2447, 2004.

[104] N Nassif, B Cense, B Park, Me Pierce, S Yun, B Bouma, G Tearney, T Chen, and J de Boer. In vivo high-resolution video-rate spectral-domain optical coherence tomography of the human retina and optic nerve. *Optics Express*, 12(3):367–376, 2004.

[105] S Yun, G Tearney, B Bouma, B Park, and Johannes de Boer. High-speed spectral-domain optical coherence tomography at 1.3 μm wavelength. *Optics Express*, 11(26):3598–3604, 2003.

[106] Christophe Dorrer, Nadia Belabas, Jean-Pierre Likforman, and Manuel Joffre. Spectral resolution and sampling issues in Fourier-transform spectral interferometry. *JOSA B*, 17(10):1795–1802, 2000.

[107] R Leitgeb, W Drexler, A Unterhuber, B Hermann, T Bajraszewski, T Le, A Stingl, and A Fercher. Ultrahigh resolution Fourier domain optical coherence tomography. *Optics Express*, 12(10):2156–2165, 2004.

[108] Yuuki Watanabe, Seiya Maeno, Kenji Aoshima, Haruyuki Hasegawa, and Hitoshi Koseki. Real-time processing for full-range Fourier-domain optical-coherence tomography with zero-filling interpolation using multiple graphic processing units. *Applied optics*, 49(25):4756–4762, 2010.

[109] Sam Van der Jeught, Adrian Bradu, and Adrian Gh Podoleanu. Real-time resampling in fourier domain optical coherence tomography using a graphics processing unit. *Journal of Biomedical Optics*, 15(3):030511–030511, 2010.

[110] S.L. Hahn. *Hilbert Transforms in Signal Processing*. Artech House signal processing library. Artech House, 1996.

[111] KM Tan, M Mazilu, TH Chow, WM Lee, K Taguchi, BK Ng, W Sibbett, CS Herrington, CTA Brown, and K Dholakia. In-fiber common-path optical coherence tomography using a conical-tip fiber. *Optics express*, 17(4):2375–2384, 2009.

[112] Andrei B Vakhtin, Daniel J Kane, William R Wood, and Kristen A Peterson. Common-path interferometer for frequency-domain optical coherence tomography. *Applied optics*, 42(34):6953–6958, 2003.

[113] Robert Tyson. *Principles of adaptive optics*. CRC press, 2010.

[114] Carla C Rosa, Hamid Hosseiny, Manuel João Ferreira, and Teresa Martins. White light interferometry measurements of PET preforms. In *OCT4NDT Symposium*, 2013.

[115] Nicola Bellini, Martin J Cox, Danielle J Harper, Sebastian R Stott, Praveen C Ashok, Kishan Dholakia, So Kawaguchi, Robert King, Tammy Horton, and Christian TA Brown. The application of optical coherence tomography to image subsurface tissue structure of antarctic krill Euphausia Superba. *PLoS ONE*, 9(10):e110367, 2014.

[116] Abdullah Al-Mujaini, Upender K Wali, and Sitara Azeem. Optical coherence tomography: clinical applications in medical practice. *Oman medical journal*, 28(2):86, 2013.

[117] Adam M Zysk, Freddy T Nguyen, Amy L Oldenburg, Daniel L Marks, and Stephen A Boppart. Optical coherence tomography: a review of clinical development from bench to bedside. *Journal of biomedical optics*, 12(5):051403–051403, 2007.

[118] K Divakar Rao, DV Udupa, C Prathap, A Rathod, R Balasubramaniam, and NK Sahoo. Optical coherence tomography for shape and radius of curvature measurements of deeply curved machined metallic surfaces: a comparison with two-beam laser interferometry. *Optics and Lasers in Engineering*, 66:204–209, 2015.

[119] Erkki Alarousu, Ahmed AlSaggaf, and Ghassan E Jabbour. Online monitoring of printed electronics by spectral-domain optical coherence tomography. *Scientific reports*, 3:1562, 2013.

[120] Hamid Hosseiny, Manuel João Ferreira, Teresa Martins, and Carla Carmelo Rosa. Characterization of PET preforms using spectral domain optical coherence tomography. In *8th Ibero American Optics Meeting/11th Latin American Meeting on Optics, Lasers, and Applications*, pages 8785DT–8785DT. International Society for Optics and Photonics, 2013.

[121] Ireneusz Grulkowski, Jonathan J Liu, Benjamin Potsaid, Vijaysekhar Jayaraman, Alex E Cable, and James G Fujimoto. Ultrahigh Speed OCT. *Optical Coherence Tomography: Technology and Applications*, pages 319–356, 2015.

[122] Jingjiang Xu, Xiaoming Wei, Luoqin Yu, Chi Zhang, Jianbing Xu, KKY Wong, and Kevin K Tsia. High-performance multi-megahertz optical coherence tomography based on amplified optical time-stretch. *Biomedical optics express*, 6(4):1340–1350, 2015.

[123] Yuji Hattori, Hiroyuki Kawagoe, Yoshimichi Ando, Masahito Yamanaka, and Norihiko Nishizawa. High-speed ultrahigh-resolution spectral domain optical coherence tomography using high-power supercontinuum at 0.8 μm wavelength. *Applied Physics Express*, 8(8):082501, 2015.

[124] Eric A Swanson, JA Izatt, CP Lin, JG Fujimoto, JS Schuman, MR Hee, D Huang, and CA Puliafito. In vivo retinal imaging by optical coherence tomography. *Optics letters*, 18(21):1864–1866, 1993.

[125] Young Kwan Kim and Yong Pyung Kim. High-speed time-domain optical coherence tomography with an imaging speed of ten frames per second with 2000 A-scan. *Optical Engineering*, 49(5):055601–055601, 2010.

[126] Adrien E Desjardins, Benjamin J Vakoc, Melissa J Suter, Seok-Hyun Yun, Guillermo J Tearney, and Brett E Bouma. Real-time FPGA processing for high-speed optical frequency domain imaging. *Medical Imaging, IEEE Transactions on*, 28(9):1468–1472, 2009.

[127] Teoman E Ustun, Nicusor V Iftimia, R Daniel Ferguson, and Daniel X Hammer. Real-time processing for Fourier domain optical coherence tomography using a field programmable gate array. *Review of Scientific Instruments*, 79(11):114301, 2008.

[128] Kenny KH Chan and Shuo Tang. High-speed spectral domain optical coherence tomography using non-uniform fast Fourier transform. *Biomedical optics express*, 1(5):1309–1319, 2010.

[129] Jianping Su, Jun Zhang, Lingfeng Yu, Henri G Colt, Matthew Brenner, and Zhongping Chen. Real-time swept source optical coherence tomography imaging of the human airway using a microelectromechanical system endoscope and digital signal processor. *Journal of biomedical optics*, 13(3):030506–030506, 2008.

[130] Yuuki Watanabe and Toshiki Itagaki. Real-time display on Fourier domain optical coherence tomography system using a graphics processing unit. *Journal of Biomedical Optics*, 14(6):060506–060506, 2009.

[131] Jian Li, Pavel Bloch, Jing Xu, Marinko V Sarunic, and Lesley Shannon. Performance and scalability of Fourier domain optical coherence tomography acceleration using graphics processing units. *Applied optics*, 50(13):1832–1838, 2011.

[132] Janarthanan Rasakanthan, Kate Sugden, and Peter H Tomlins. Processing and rendering of Fourier domain optical coherence tomography images at a line rate over 524 kHz using a graphics processing unit. *Journal of biomedical optics*, 16(2):020505–020505, 2011.

[133] Jun Ke and Edmund Y Lam. Image reconstruction from nonuniformly spaced samples in spectral-domain optical coherence tomography. *Biomedical optics express*, 3(4):741–752, 2012.

[134] Kai Wang, Zhihua Ding, Tong Wu, Chuan Wang, Jie Meng, Minghui Chen, and Lei Xu. Development of a non-uniform discrete Fourier transform based high speed spectral domain optical coherence tomography system. *Optics express*, 17(14):12121–12131, 2009.

[135] Kang Zhang and Jin U Kang. Graphics processing unit accelerated non-uniform fast Fourier transform for ultrahigh-speed, real-time Fourier-domain OCT. *Optics express*, 18(22):23472–23487, 2010.

[136] Ling Wang, Bernd Hofer, Jeremy A Guggenheim, and Boris Považay. Graphics processing unit-based dispersion encoded full-range frequency-domain optical coherence tomography. *Journal of biomedical optics*, 17(7):077007–077007, 2012.

[137] Yan Wang, Christian M Oh, Michael C Oliveira, M Shahidul Islam, Arthur Ortega, and B Hyle Park. GPU accelerated real-time multi-functional spectral-domain optical coherence tomography system at 1300nm. *Optics express*, 20(14):14797–14813, 2012.

[138] Jing Xu, Kevin Wong, Yifan Jian, and Marinko V Sarunic. Real-time acquisition and display of flow contrast using speckle variance optical coherence tomography in a graphics processing unit. *Journal of biomedical optics*, 19(2):026001–026001, 2014.

[139] Kenneth KC Lee, Adrian Mariampillai, Joe XZ Yu, David W Cadotte, Brian C Wilson, Beau A Standish, and Victor XD Yang. Real-time speckle variance swept-source optical coherence tomography using a graphics processing unit. *Biomedical optics express*, 3(7):1557–1564, 2012.

[140] Yong Huang, Xuan Liu, and Jin U Kang. Real-time 3D and 4D Fourier domain Doppler optical coherence tomography based on dual graphics processing units. *Biomedical optics express*, 3(9):2162–2174, 2012.

[141] Hyosang Jeong, Nam Hyun Cho, Unsang Jung, Changho Lee, Jeong-Yeon Kim, and Jeehyun Kim. Ultra-fast displaying spectral domain optical Doppler tomography system using a graphics processing unit. *Sensors*, 12(6):6920–6929, 2012.

[142] Marcin Sylwestrzak, Daniel Szlag, Maciej Szkulmowski, Iwona Gorczynska, Danuta Bukowska, Maciej Wojtkowski, and Piotr Targowski. Four-dimensional structural and Doppler optical coherence tomography imaging on graphics processing units. *Journal of biomedical optics*, 17(10):100502–100502, 2012.

[143] Dong-hak Choi, Hideaki Hiro-Oka, Kimiya Shimizu, and Kohji Ohbayashi. Spectral domain optical coherence tomography of multi-MHz A-scan rates at 1310 nm range and real-time 4D-display up to 41 volumes/second. *Biomedical optics express*, 3(12):3067–3086, 2012.

[144] Yifan Jian, Kevin Wong, and Marinko V Sarunic. Graphics processing unit accelerated optical coherence tomography processing at megahertz axial scan rate and high resolution video rate volumetric rendering. *Journal of biomedical optics*, 18(2):026002–026002, 2013.

[145] Wolfgang Wieser, Wolfgang Draxinger, Thomas Klein, Sebastian Karpf, Tom Pfeiffer, and Robert Huber. High definition live 3D-OCT in vivo: design and evaluation of a 4D OCT engine with 1 GVoxel/s. *Biomedical optics express*, 5(9):2963–2977, 2014.

[146] Kang Zhang and Jin U Kang. Real-time intraoperative 4D full-range FD-OCT based on the dual graphics processing units architecture for microsurgery guidance. *Biomedical optics express*, 2(4):764–770, 2011.

[147] Joachim Probst, Dierck Hillmann, Eva Lankenau, Christan Winter, Stefan Oelckers, Peter Koch, and Gereon Hüttmann. Optical coherence tomography with online visualization of more than seven rendered volumes per second. *Journal of biomedical optics*, 15(2):026014–026014, 2010.

[148] Marcin Sylwestrzak, Daniel Szlag, Maciej Szkulmowski, and Piotr Targowski. Real-time massively parallel processing of spectral optical coherence tomography data on graphics processing units. In *European Conferences on Biomedical Optics*, pages 80910V–80910V. International Society for Optics and Photonics, 2011.

[149] Kang Zhang and Jin U Kang. Real-time 4D signal processing and visualization using graphics processing unit on a regular nonlinear-k Fourier-domain OCT system. *Optics express*, 18(11):11772–11784, 2010.

[150] Adrian Gh Podoleanu and Richard B Rosen. Combinations of techniques in imaging the retina with high resolution. *Progress in retinal and eye research*, 27(4):464–499, 2008.

[151] Ireneusz Grulkowski, Jonathan J Liu, Benjamin Potsaid, Vijaysekhar Jayaraman, Chen D Lu, James Jiang, Alex E Cable, Jay S Duker, and James G Fujimoto. Retinal, anterior segment and full eye imaging using ultrahigh speed swept source OCT with vertical-cavity surface emitting lasers. *Biomedical optics express*, 3(11):2733–2751, 2012.

[152] WooJhon Choi, Benjamin Potsaid, Vijaysekhar Jayaraman, Bernhard Baumann, Ireneusz Grulkowski, Jonathan J Liu, Chen D Lu, Alex E Cable, David Huang, Jay S

Duker, et al. Phase-sensitive swept-source optical coherence tomography imaging of the human retina with a vertical cavity surface-emitting laser light source. *Optics letters*, 38(3):338–340, 2013.

[153] ByungKun Lee, WooJhon Choi, Jonathan J Liu, Chen D Lu, Joel S Schuman, Gadi Wollstein, Jay S Duker, Nadia K Waheed, and James G Fujimoto. Cardiac-gated en face doppler measurement of retinal blood flow using swept-source optical coherence tomography at 100,000 axial scans per second. *Investigative ophthalmology & visual science*, 56(4):2522–2530, 2015.

[154] NVIDIA. NVIDIA CUDA Compute Unified Device Architecture : Reference Manual, August 2014.

[155] Mark Harris. How to Optimize Data Transfers in CUDA C/C++. https://devblogs.nvidia.com/parallelforall/how-optimize-data-transfers-cuda-cc/, December 2012.

[156] Mark Harris. How to Overlap Data Transfers in CUDA C/C++. https://devblogs.nvidia.com/parallelforall/how-overlap-data-transfers-cuda-cc/, December 2012.

[157] Ruikang K Wang and Zhenhe Ma. A practical approach to eliminate autocorrelation artefacts for volume-rate spectral domain optical coherence tomography. *Physics in medicine and biology*, 51(12):3231, 2006.

[158] Ji-hyun Kim, Jaehong Aum, Jae-Ho Han, and Jichai Jeong. Optimization of compute unified device architecture for real-time ultrahigh-resolution optical coherence tomography. *Optics Communications*, 334:308–313, 2015.

[159] NVIDIA. CUFFT Library User's Guide, August 2014.

[160] OpenGL. The OpenGL Utility Toolkit. www.opengl.org/resources/libraries/glut, November 2015.

[161] Hamid Hosseiny. 4D SS-OCT Media Files. http://photonics.inescporto.pt/Members/shh/phdthesis/4d_ssoct, March 2016.

[162] Nicholas Wilt. *The CUDA handbook: A comprehensive guide to GPU programming*. Pearson Education, 2013.

[163] Mark Harris. Optimizing parallel reduction in CUDA. *NVIDIA Developer Technology*, 2(4), 2007.

[164] Thomas A Pitkin. GPU ray tracing with CUDA. 2013.

[165] Tomas Akenine-Möller, Eric Haines, and Naty Hoffman. *Real-time rendering*. CRC Press, 2008.

[166] Kevin Suffern. *Ray Tracing from the Ground up*. AK Peters, 2007.

[167] NVIDIA. Visual Profiler User's Guide. http://docs.nvidia.com/cuda/profiler-users-guide, November 2015.

[168] Andrew L Lopez, Shang Wang, Kirill V Larin, Paul A Overbeek, and Irina V Larina. Live four-dimensional optical coherence tomography reveals embryonic cardiac phenotype in mouse mutant. *Journal of biomedical optics*, 20(9):090501–090501, 2015.

[169] Saba H Syed, Andrew J Coughlin, Monica D Garcia, Shang Wang, Jennifer L West, Kirill V Larin, and Irina V Larina. Optical coherence tomography guided microinjections in live mouse embryos: high-resolution targeted manipulation for mouse embryonic research. *Journal of biomedical optics*, 20(5):051020–051020, 2015.

[170] Koji Inada, Rina Matsuda, Chizuru Fujiwara, Mitsutoshi Nomura, Tatsumi Tamon, Ikkan Nishihara, Takeshi Takao, and Toshihiro Fujita. Identification of plastics by infrared absorption using InGaAsP laser diode. *Resources, Conservation and Recycling*, 33(2):131 – 146, 2001.

[171] Haibo Huang, Haiyan Yu, Huirong Xu, and Yibin Ying. Near infrared spectroscopy for on/in-line monitoring of quality in foods and beverages: A review. *Journal of Food Engineering*, 87(3):303 – 313, 2008.

[172] National Instruments. LabVIEW 2011 User's Manual, June 2011.

[173] DALSA. Spyder GigE Application Guide, March 2010.

[174] N.A. Lange and J.A. Dean. *Lange's Handbook of Chemistry*. McGraw-Hill, 1973.

Appendix A

System Characterization Summary

Table A.1 summarizes the performance characterization results of the CP-SD-OCT and the SD-OCT systems.

Description	CP-SD-OCT System	SD-OCT System
Operating wavelength	1000 nm - 1100 nm	1000 nm - 1100 nm
λ_0	∼1050 nm	∼1050 nm
$\Delta\lambda$	50 nm	50 nm
Axial Resolution	$\sim 20\ \mu m$	$\sim 24.07\ \mu m$
Maximum imaging depth (z_{max})	∼ 3.06 mm	∼ 3.2 mm
Fringe visibility at OPD 0.1 mm	0.93	0.93
Sensitivity	∼ 98.21 dB	∼97.43 dB
Sensitivity fall-off at z_{max}	30.93 dB	9.64 dB
Camera line rate	36 kHz	36 kHz
Samples per A-scan	2048	2048
A-scan processing rate (high sensitivity mode)	∼21 kHz	∼21 kHz

Table A.1: The characterization summary of the CP-SD-OCT and the SD-OCT systems.

Appendix B

SD-OCT Imaging System Setup

Fig.B.1 demonstrates a screenshot of the implemented real-time video rate SD-OCT imaging system consisting of the broadband light source BOS, a fiber based Michelson interferometer, and the developed spectrometer with configuration B described in detail in Chapter 3. Such an optical imaging system was developed at the CAP's lab of INESC TEC for sensing and imaging applications.

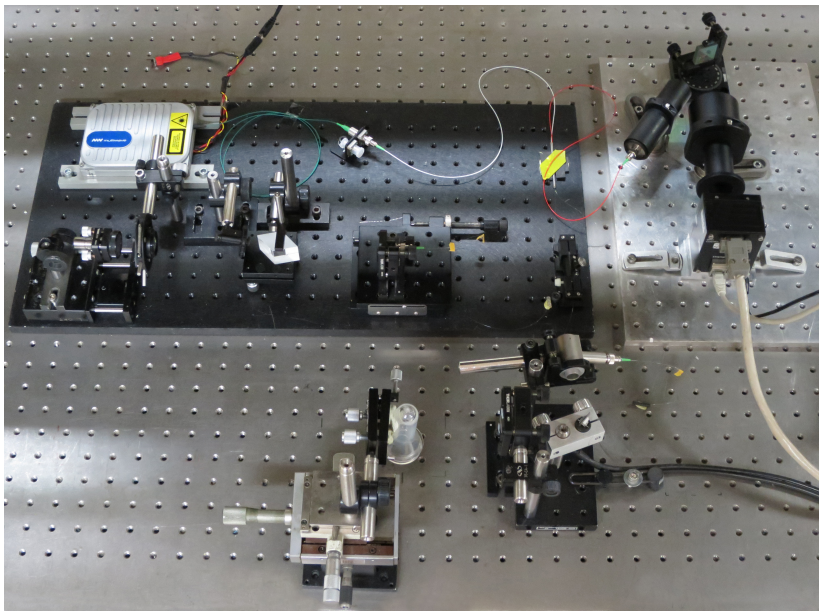

Figure B.1: A screenshot of the real-time video rate SD-OCT imaging system at CAP's lab of INESC TEC developed for industrial nondestructive testing applications.

Fig.B.2 shows two screenshots of the implemented scanning and detection unit of the SD-OCT imaging system. Fig.B.2.A illustrates the developed sample arm, and Fig.B.2.B exhibits the implemented spectrometer with configuration B described in Chapter 3.

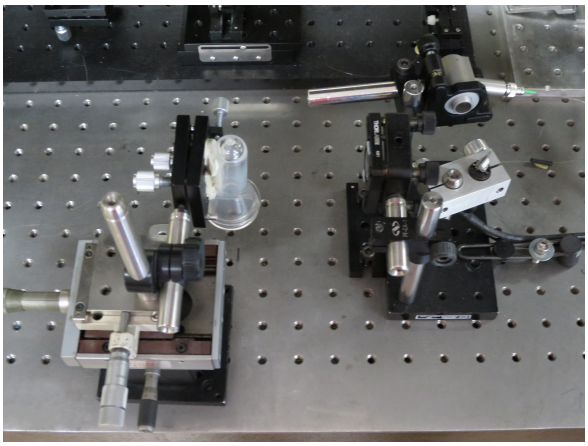

A

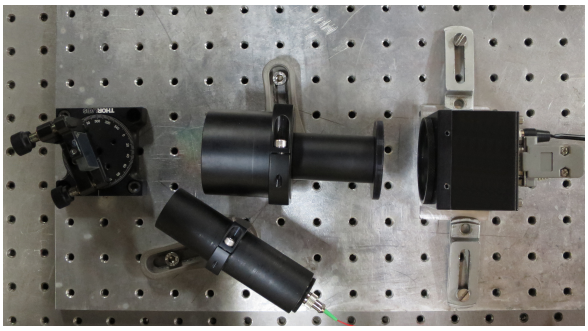

B

Figure B.2: Two screenshots of the implemented (A) sample arm and (B) spectrometer with configuration B explained in Chapter 3.

Appendix C

LabVIEW Applications

Fig.C.1 demonstrates a screenshot of the developed LabVIEW application to acquire data from the line-scan DALSA camera. This application was used for the purpose of monitoring and optimization of the CP-SD-OCT and the SD-OCT systems.

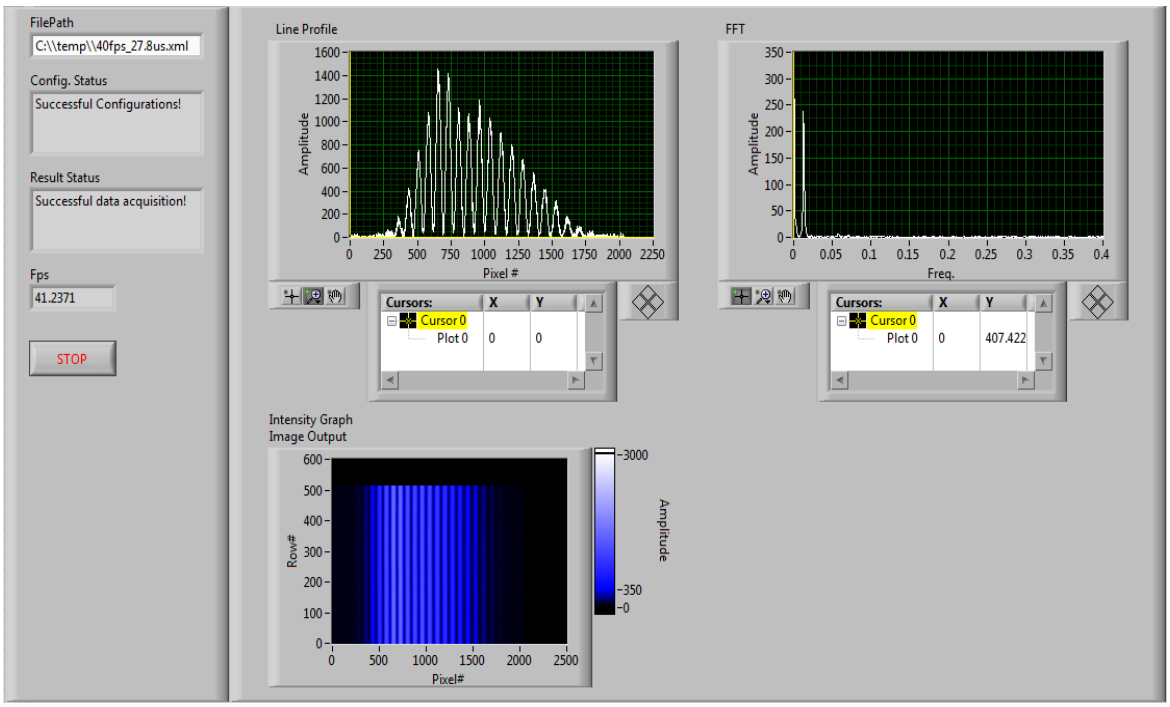

Figure C.1: A screenshot of the developed LabVIEW application to acquire data from the line-scan DALSA camera.

Fig.C.2 illustrates a screenshot of the developed LabVIEW application for the SD-OCT imaging system. The application consists of data acquisition, data processing, and calibration units. The compiled DLL files by Visual Studio C++ software, implemented for the acquisition and processing of spectrum data, were directly called in LabVIEW by using Call Library Function Nodes. The auto-correlation artifacts and the background noise can be removed either by recording the background signal in "Background Signal" tab or deducting the ensemble average of each frame from each A-scan in GPU.

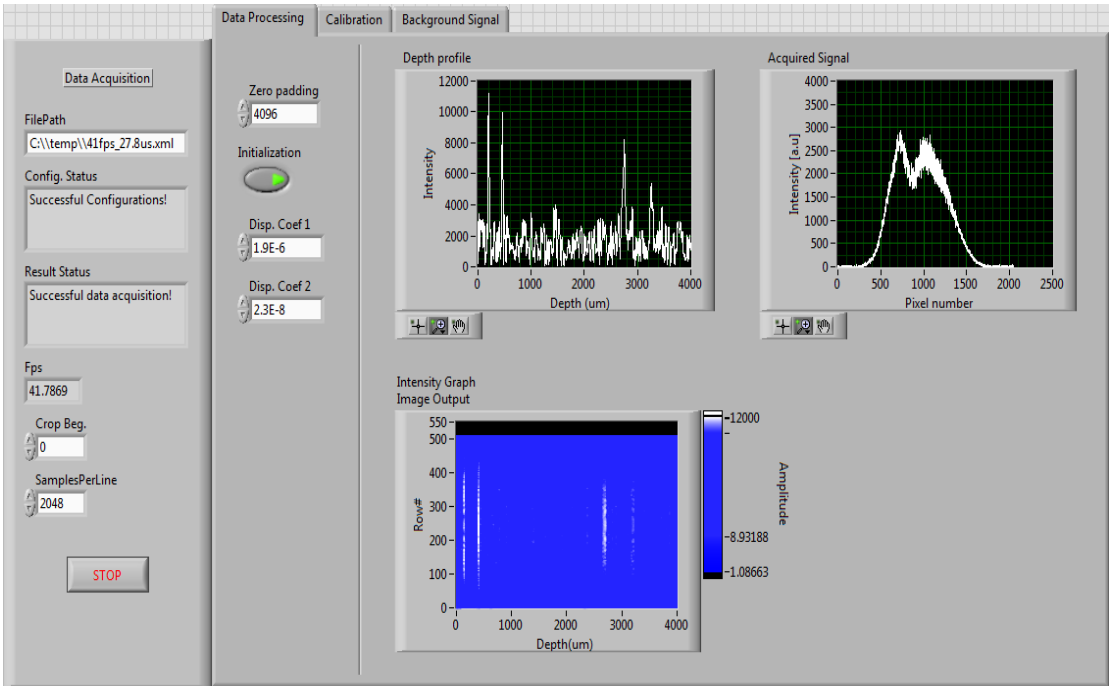

Figure C.2: A screenshot of the developed LabVIEW application for the SD-OCT system.

Appendix D

MATLAB Code

D.1 Sensitivity Fall-off Effect

MATLAB simulation code implemented to demonstrate the sensitivity fall-off effect:

```
clc;
close all;

x = -2.5:0.001:2.5;

%Sinc function
y1 = abs(sinc(x));

%Gaussian functions, the peak width broadens as OPD increases
y2 = 0.27*gaussmf(x,[.03 -0.75]);
y3 = 0.61*gaussmf(x,[.026 -0.5]);
y4 = 0.93*gaussmf(x,[.022 -0.2]);
y5 = 0.93*gaussmf(x,[.022 0.2]);
y6 = 0.61*gaussmf(x,[.026 0.5]);
y7 = 0.27*gaussmf(x,[.03 0.75]);

%Plot all functions together figure;
plot(x,y1,'black','linewidth',2);
hold on;
plot(x,y2,'blue',x,y3,'red',x,y4,'black',x,y5,'black',x,y6,'red',x,y7,
    'blue','linewidth',1); xlabel('Optical Depth');
ylabel('Amplitude');
```

D.2 Verification of Processing Steps

The implemented MATLAB code to verify the result of each processing step performed by GPU:

```
clc;
clear all;

frameNo = 60;
numAscans = 601;
usefulAscans = 512;
numSamplesPerLine = 928;
numFrames = 1536;

BGLines = 200;
initialFlyBackLines = 220;
initialLineShift = 708;

cropBeg = 80;
cropEnd = 200;

f = fopen('D:\\RecordedData\\Ophthalmic_20150301T140304.dat');
%Read Background Data
BGData = fread(f, [numSamplesPerLine BGLines], 'int16');

%Initialize BGProcessed by zero
%The first line was deleted as it does not have meaningful information
BGProcessed = zeros(numSamplesPerLine-cropBeg-cropEnd, BGLines-1);
for i = 2: BGLines
 BGProcessed(:,i-1) = BGData(cropBeg+1:end-cropEnd, i);
end

%compute the average of (BGLines-1) lines
BG = mean(BGProcessed, 2);

%Place the read pointer at the right position in the file
%Each data element is int16, so it consists of 2 bytes
fseek( f, numSamplesPerLine*numAscans*(frameNo-1)*2 +
   (BGLines+initialFlyBackLines+initialLineShift)*
    numSamplesPerLine*2,'bof');

%Read the frame indicated by frameNo
ReadData = fread(f, [numSamplesPerLine numAscans], 'int16');
```

```
39 fclose(f);
40
41 %Select usefulAscans and remove fly back lines
42 AlignedData = zeros(numSamplesPerLine-cropBeg-cropEnd, usefulAscans);
43 for i =1:usefulAscans
44  AlignedData(:,i) = ReadData(cropBeg+1:end-cropEnd, i);
45 end
46
47 %Background subtraction
48 ReadDataBS = AlignedData - repmat(BG, [1, usefulAscans]);
49
50 %Spectral shaping
51 w = hamming(size(AlignedData,1));
52 for i =1:usefulAscans
53  ReadDataBS(:,i) = ReadDataBS(:,i).*w;
54 end
55
56 %FFT and modulus computation
57 fftResult = log10(abs(fft(ReadDataBS,[],1)));
58
59 %Normalization, used for the sake of display
60 fftResult = (fftResult-min(fftResult(:))./
61              (max(fftResult(:))-min(fftResult(:)));
62 %imadjust maps the values in the first bracket to the second one
63 fftResult = imadjust(fftResult,[0.68 1],[0 1]);
64
65 %Display half of the spectrum
66 figure;
67 imshow(mat2gray(fftResult(1:size(fftResult,1)/2, :)));
```

D.3 B-scan Image Post-Processing

The post-processing code implemented to automate the computation of optical thickness measurements of the layers of bottle PET preforms:

```
clc;
close all;

%Read the input image
I = imread('D:\\PET13.png');
figure;
imshow(I);

Red = I(:,:,1); % Red Channel
Green = I(:,:,2); % Green Channel
Blue = I(:,:,3); % Blue Channel

%Convert the image to a grayscale image
I = rgb2gray(I);
%Find the vertical edges by using Sobel Edge detector
J = edge(I,'sobel','vertical');

%A median filter can be applied in case the input image is noisy.
%B = medfilt2(J);

%Draw the white vertical lines where the layers are
Red(:,sum(J)>5) = 256;
Green(:,sum(J)>5) = 256;
Blue(:,sum(J)>5) = 256;

%Concatenate the colors
H = cat(3, Red, Green, Blue);
figure;
imshow(H);
```